SPIN-DEPENDENT ELECTRON TRANSPORT IN NANOSCALE SAMPLES

A Thesis
Presented to
The Academic Faculty

by

Yaguang Wei

In Partial Fulfillment
of the Requirements for the Degree
Doctor of Philosophy in the
School of Physics

Georgia Institute of Technology
December 2007

SPIN-DEPENDENT ELECTRON TRANSPORT IN NANOSCALE SAMPLES

Approved by:

Professor Dragomir Davidovic, Advisor,
Committee Chair
School of Physics
Georgia Institute of Technology

Professor Walter A. de Heer
School of Physics
Georgia Institute of Technology

Professor Alexei Marchenkov
School of Physics
Georgia Institute of Technology

Professor Elisa Riedo,
School of Physics
Georgia Institute of Technology

Professor David Citrin,
School of electrical and computer
engineering
Georgia Institute of Technology

Date Approved: 13 November 2007

To my parents, my loving wife and daughter

ACKNOWLEDGEMENTS

First I would like to thank my research advisor, Professor Dragomir Davidovic for his guidance, encouragement and support throughout my stay at Georgia Tech. He has been and will continue to be my best sources of inspiration and support. I would like to extend my gratitude to Professor Walter A. de Heer, Professor Alexei Marchenkov, Professor Elisa Riedo and Professor David Citrin for serving on my Ph.D. committee as well as providing help on my research and study.

I would like to thank all the past and present group members. I thank Xiya Liu for working with me on my first project. Thanks for Dr. Liyuan Zhang's great help through so many years. I give my thanks to Chris Malec, I am grateful for your passionate and hard working during our collaboration. Thanks to former group members: Cunyun Wang, Dr. Andrei Korotkov, Dr. Anaya Armando, Rupa Bhaumik, Michael Bowman and Anthony Liang.

Special thanks goes to Dr. Zhenting Dai, who provides valuable discussion on sample fabrication and cryogenic techniques. I would like to thank Dr. Claire Berger, Dr. Yan Yi, Dr. Zhimin Song, Xuebin Li and Tai-De Li for helping me on AFM.

I would like to thank assistance and cooperation from Kevin Carter, Keith Garner, Debbie James, Velera Pate, Nancy Bagget, Patricia Dixon, and Lori Sheridan.

I enjoyed six-year living in Atlanta. Thanks my friends: Qiang Cao, Zhen Zhou, Jiang Xiao, Bo li, Tianbo Li, Wuwei Liang, Francine, Emily and Dixon.

I would like to thank my parents, my parents-in-law and my sister for their love and encouragement. Without them, this dissertation would not be possible.

Finally I would like to thank my wife and my best friend Yujia for her love, support and understanding.

TABLE OF CONTENTS

LIST OF FIGURES

SUMMARY

In this thesis, we describe the research in which we use metallic nanoparticles to explore spin-dependent electron transport at nanometer scale. Nanoscale samples were fabricated by using a state of the art electron beam lithography and shadow evaporation technique. We have investigated spin relaxation and decoherence in metallic grains as a function of bias voltage and magnetic field at low temperatures (down to $\sim$ 30mK).

At low temperatures, the discrete energy levels within a metallic nanoparticle provides a new means to study the physics of the spin-polarized electron tunneling. We describe measurements of spin-polarized tunneling via discrete energy levels of single Aluminum grain. Spin polarized current saturates quickly as a function of bias voltage, which demonstrates that the ground state and the lowest excited states carry spin polarized current. The ratio of electron-spin relaxation time (T_1) to the electron-phonon relaxation rate is in quantitative agreement with the Elliot-Yafet scaling, an evidence that spin-relaxation in Al grains is driven by the spin-orbit interaction. The spin-relaxation time of the low-lying excited states is $T_1 \approx 0.7\ \mu s$ and $0.1\ \mu s$ in two samples, showing that electron spin in a metallic grain could be a potential candidate for quantum information research.

We also present measurements of mesoscopic resistance fluctuations in cobalt nanoparticles at low temperature and study how the fluctuations with bias voltage, bias fingerprints, respond to magnetization-reversal processes. Bias fingerprints rearrange when domains are nucleated or annihilated. The domain wall causes an electron wave function-phase shift of $\sim 5\ \pi$. The phase shift is not caused by the Aharonov-Bohm effect; we explain how it arises from the mistracking effect, where electron spins lag in orientation with respect to the moments inside the domain wall. The dephasing length at low temperatures is only 30 nm, which is attributed to the large magnetocrystalline anisotropy in Co.

CHAPTER I

INTRODUCTION

Spintronics is a novel research field which involves the study of active control and manipulation of spin degrees of freedom in solid state systems [1, 2, 3]. The emerging spintronics technology may offer higher density of integration, nonvolatility, faster operating speed and lower power consumption compared to traditional semiconductor technology.

As spintronics goes nanometer scale with zero-dimension, new phenomena are predicted resulting from the interplay between spin dependent electron transport and single electron physics. The spin transport investigations of mesoscopic islands [4, 5] and granular films [6, 7] have lead to progress in understanding the effect of confinement on spin in metallic nanometer scale samples.

In order to make use of spin, one needs to have: 1) a device capable of generating and measuring spin-polarized current, 2) spin stability during the transit time, and 3) a technique to manipulate spin. One of the challenges faced in spintronics is that electron spin can be flipped in normal metals and semiconductors, leading to a finite lifetime of the spin-polarized current. In order to investigate spin transport, spin lifetime must be longer than the transit time and the time it takes to inject, manipulate and measure spin information.

In semiconductors, electron spin lifetimes can be enhanced by orders of magnitude as a function of dopant concentration [8]. In semiconductor heterostructures and quantum dots [9], electron spin lifetimes on the order of nanoseconds persist, even at room temperature. Because of its stability, the spin of an electron confined in a semiconductor quantum dot has been proposed as a candidate quantum bit [10, 11]. It has been theoretically shown that the dominant spin-flip scattering mechanisms of the bulk become significantly suppressed in quantum dots, because of the the zero-dimensional character of the electronic wave function [12, 13]. These theoretical predictions have been confirmed experimentally in GaAs quantum

dots. Longitudinal spin relaxation times (T_1) exceeding 200 μs [14] and 0.8 ms [15] have recently been demonstrated. Despite the fact that the spin relaxation time (T_1) is very long, the spin coherent time measured in GaAs quantum dot is only $\sim$ ns [16]. In GaAs quantum dot, dephasing is caused by spin precession around an effective magnetic field created by nuclear spin [17].

In bulk metals and metallic thin films, spin lifetimes are relatively short due to strong spin flip scattering. Theoretical work has shown that the dominant spin flip mechanism is caused by the spin-orbit interaction [18, 19]. Spin flip scattering through spin-orbit interaction leads to a spin lifetime τ_{SO} that is proportional to the momentum relaxation time τ, $\tau_{SO} = \tau/\alpha$ (Elliot-Yafet relation, where α is scattering ratio). Electron-phonon scattering is suppressed at low temperature, hence τ becomes equal to the elastic electron scattering time. The scattering ratio ($\alpha \ll 1$) depends on the atomic number and band structure of the metal. In aluminum thin films, the scattering ratio is enhanced by the "spin hot-spots" in the band-structure [20, 21, 22] and the spin relaxation time is about $0.1ns$ [23].

Analogous to the way that spin lifetime is enhanced in semiconducting quantum dots relative to bulk semiconductors [12, 13], we expect that spin lifetime in nanometer-scale metallic grains should be much longer than that in bulk metals or metallic thin films. This prediction follows from the quantization of the energy levels of a single nanoparticle. Absence of continuum in states restricts the pathways for spin relaxation. Also, quantum chaos reduces the overlap between initial and final states.

Also, in nanometer scale grains, the spin-orbit interaction affects the energy levels and the eigenstates and does not lead to spin-relaxation [24, 25, 26]. In zero dimensions, only interactions between electron spins and the environment can lead to spin-relaxation [12, 13], as opposed to bulk. Such interactions include spin-orbit coupling to phonons and hyperfine coupling to nuclear spins. So the dominant mechanism of spin flip scattering in bulk becomes ineffective in nanometer scale metallic grains.

The spin relaxation time of an electron confined in a metallic grain has not yet been measured precisely. Deshmukh et al [27], have found that the energy relaxation time of some

excited states in an aluminum grain in a weak magnetic field was comparable to or larger than $19ns$. The spin preserving energy relaxation time, on the other hand, was predicted to be ~ 10 ns [28], suggesting that the spin relaxation time may be comparable to or larger than $19ns$.

In the first part of this thesis, we will investigate spin transport in nanometer-scale metallic grains connected to reservoirs via tunneling junctions (metallic quantum dots). We will use ferromagnetic metals ($Ni_{0.8}Fe_{0.2}$) to make the reservoirs, and nonmagnetic metals (aluminum) to make the nanometer scale grains, the insulating layers are made by Al_2O_3. The grains are sufficiently small to display discrete energy levels at experimentally accessible temperatures. The spin relaxation time of single electron spins will be determined through spin injection and detection [29]. The interplay between single electron charging effects and ferromagnetism in single metallic islands was studied both experimentally [30, 31, 32] and theoretically [33, 34, 35, 36, 37, 38, 39, 40, 41]. But in these studies, metallic islands were large and did not exhibit discrete quantum states. More recently, Deshmukh and Ralph [5] have used discrete quantum states in an aluminum grain as spin filters to investigate spin polarization effects in a ferromagnetic reservoir.

In our investigation, the metallic grain exhibits both discrete quantum states and TMR (tunneling magnetoresistance) effects. Prior to our work, spin-coherent electron tunneling via nanometer scale normal metallic grains has been confirmed in arrays [7] and in single grain [42]. However, the electron spin relaxation time T_1 in a metallic grain has not been studied yet. Here we report on spin polarized tunneling via discrete energy levels of single aluminum grain.

In the second part of the thesis, we investigate the resistance of mesoscopic ferromagnets at low temperatures. In micron scale metallic samples at low temperatures, interference among scattered electron waves creates noticeable contributions to sample resistance, including random but reproducible fluctuations in conductance (CF) [43, 44, 45]. One remarkable consequence is that the resistance of phase-coherent samples becomes sensitive to microscopic impurity configurations. We find a similar result, that the resistance of a mesoscopic ferromagnet is very sensitive to the magnetic state of the sample. In particular,

we observe significant wave-function phase shifts generated by domain walls.

CHAPTER II

SPIN-POLARIZED TUNNELING AND SPIN RELAXATION IN SINGLE ALUMINUM NANOPARTICLE: MOTIVATION AND THEORETICAL OVERVIEW

Electron tunneling through single nanometer scale metallic grains at low temperatures can display a discrete energy level spectrum [46]. Tunneling spectroscopy of the energy spectra have led to numerous discoveries, including Fermi-Liquid coupling constants between quasiparticles [28], spin-orbit interactions [47, 48], and superconducting correlations in zero-dimensional systems [49] Some information regarding the spin of an electron occupying a discrete level can be obtained using spin-unpolarized tunneling, such as spin-multiplicity and electron g-factors [46].

Here we report on spin-polarized tunneling via discrete energy levels of single aluminum grains. Spin-polarized electron transport permits studies of spin relaxation and spin dephasing [29, 23]. By comparison, spin-unpolarized spectroscopy is suitable for the studies of energy relaxation in the grains [46, 28]. Since spin-relaxation times are generally many orders of magnitude longer than energy relaxation times, spin-unpolarized spectroscopy is not an easy tool to study spin-relaxation in the grains and spin-polarized tunneling is needed.

Spin-polarized transport via metallic grains has recently generated a lot of theoretical interest [50, 51, 52, 53, 54]. Spin-coherent electron tunneling via nanometer scale normal metallic grains has been confirmed in arrays [7, 55] and in single grains [42]. However, the electron spin-relaxation time T_1 in a metallic grain has not been reported yet.

2.1 Spin Lifetime and Spin Relaxation

2.1.1 Spin Lifetime: T_1 and T_2

The dominant spin relaxation mechanism in normal metals is suppressed in nanoparticles because energy level quantization. In the absence of the contribution from momentum relaxation, we expect that the spin relaxation in nanoparticles is caused by an interaction between electron spin and environment. We refer to the corresponding relaxation time as the intrinsic relaxation time. The intrinsic spin relaxation time can be longitudinal T_1 and transverse T_2.

The longitudinal spin relaxation time (T_1), also called spin-lifetime, is the decay time from a spin-down state into a spin-up state in a strong magnetic field applied parallel to spin direction. Equivalently, it is the time of thermal equilibration of the spin population with the environment. In Figure 2.1, we sketch the spin-relaxation process in a quantum dot in a parallel magnetic field. If an electron occupies the upper energy level (spin-down), then T_1 is the decay time for the electron into the lower (spin-up) state. At low temperatures, this decay process involves emission of energy into the environment (phonon, for example). This relaxation is irreversible.

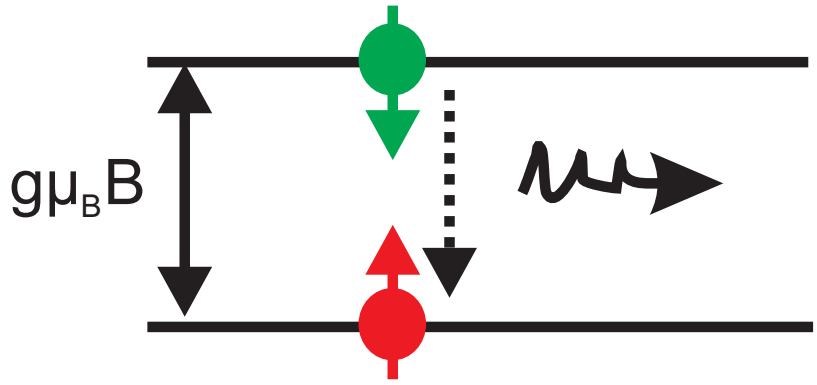

Figure 2.1: Diagram of the spin-relaxation process in a quantum dot in a parallel magnetic field.

Spin dephasing time (T_2), also called transverse spin relaxation time, is classically the time it takes for an ensemble of transverse electron spins, initially precessing in phase about the longitudinal field, to lose their phase due to spatial and temporal fluctuations of the precessing frequencies. If a spin is initially perpendicular to the magnetic field, it will precess around the magnetic field with frequency $g\mu_B B/h$. T_2 is the coherence time of

these precessions. T_2 is responsible for the line-width in magnetic resonance.

For conduction electrons in metals, Yafet [19] showed that $T_2 \leq 2T_1$, and T_2 changed with the direction by at most a factor of 2. In isotropic solid, $T_2 \leq T_1$ at zero magnetic field [19]. Prior measurements of T_1 in quantum dots were made in a strong magnetic field [14]. Spin injection and detection techniques measure spin-relaxation in zero magnetic field [29], thus allowing us to measure T_2 of single electrons in nanometer scale metallic grains. (In metals, the width of the conduction electron spin resonance line $1/(g\mu_B T_2)$ and the resistivity have similar magnetic field dependence [19]. Because the mean free path in our case is short, it follows that T_2 does not vary significantly with magnetic field.)

2.1.2 Spin Relaxation mechanisms

For spin relaxation of conduction electrons, four relevant mechanisms have been found for metals and semiconductors [2]: the Elliott-Yafet, Dyakonov-Perel, Bir-Aronov-Pikus, and hyperfine-interaction mechanisms. Ref. [2] claims that the majority of simple metals are believed to follow the Elliott-Yafet mechanism of spin relaxation. This claim is supported by several facts [2]. Since we study the spin relaxation in metallic particle, we will briefly discuss Elliott-Yafet mechanism of spin relaxation.

In the Elliott-Yafet mechanism, spin-orbit coupling induced by ions causes spins to relax. As a result, the electron wave functions associated with a given spin mix with the opposite-spin states. By the Elliot-Yafet relation [18], the spin-orbit scattering rate τ_{SO}^{-1} is related to the elastic scattering rate τ_e^{-1}: $\tau_{SO}^{-1} = \alpha\tau_e^{-1}$. The spin-orbit scattering includes both spin-flip and spin-conserving processes, so spin-orbit scattering rate τ_{SO}^{-1} is larger than spin relaxation time T_1

The majority of simple metals are believed to follow the Elliott-Yafet mechanism of spin relaxation. Especially, the Elliott-Yafet mechanism has been found to be valid for Al. This is supported by several facts according to ref. [2]:

- The Elliott-Yafet mechanism gives the right order of magnitude for τ_{SO}, while other possible spin relaxation mechanisms give much greater τ_{SO} than what is observed.

- The temperature dependence of τ_{SO} is consistent with the Elliott-Yafet mechanism.
- A realistic, first-principles calculation for Al [21] shows excellent agreement with experiment [56].
- The Elliott and Yafet relations [57, 58] has been proved to be valid for the majority of metals tested (alkali and noble). The deviation from the Yafet relation for several polyvalent metals (Al, Pd, Be, and Mg) was later resolved by spin-hot-spot theory [20, 58].

2.1.3 Spin Relaxation in Metallic Grains

In this section we discuss the spin-flip process in metallic grains. As discussed above, in metallic thin films, spin-orbit interaction leads to a finite spin lifetime that is proportional to the momentum relaxation time $\tau_{SO} = \tau/\alpha$. Since the physical properties change in a fundamental way in response to the confinement, it shouldn't be surprising that the spin-flip process in metallic grains is very different from that of bulk.

If an electron enters the grain from one reservoir and then exits to another reservoir, one may expect that the spin-flip probability is small if the transit time through the grain is smaller than τ/α, and that the spin-flip probability is large if the transit time through the grain is larger than τ/α. However, this picture is incorrect because of the quantization of energy. In fact, the probability of a spin-flip through momentum scattering is independent of the transit time. In nanometer scale grains, the spin-orbit interaction affects the energy levels and the eigenstates and does not lead to spin- relaxation [24, 25, 26]. In zero dimensions, only interactions between electron spins and the environment can lead to spin-relaxation [12, 13]. Such interactions include spin-orbit coupling to phonons and hyperfine coupling to nuclear spins.

To simplify further discussion, we assume that the contact resistances (R) between the grain and the two leads are the same. Assuming that the grains are ballistic. In this

case, the elastic scattering time inside the grains is given by $\tau_e \sim D/v_F$, where D is the grain diameter and v_F is the Fermi velocity. The electron transit time through the grain (τ_0) is roughly equal to $Rh/R_Q\delta$, where $R_Q = h/e^2 = 25.8k\Omega$ is the resistance quantum and δ is the single-electron level spacing of the grain [59]. In zero magnetic field, the eigenstates of the grain are two-fold degenerate because of the Kramers degeneracy [24]. A pair of these degenerate states is also known as a Kramers doublet. In a magnetic field, the eigenstates split because of the Zeeman interaction. Theoretically, the spin-orbit interaction is characterized by the strength parameter $s = h/(\tau_{SO}\delta)$, where $\tau_{SO} = \tau_e/\alpha$ [25].

If $s \ll 1$, then the spin-orbit scattering is weak. In this case, the eigenstates are approximately pure spin-up and spin-down states and the g-factors are close to 2.

If $s \gg 1$, then spin-orbit scattering is strong, and the spin-up and spin-down states are significantly mixed in the eigenstates. The g-factors are significantly suppressed ($g \sim 1/s \ll 2$), and they vary among different energy levels and different directions of the applied magnetic field ($rms(g) \sim g$).

We define a characteristic diameter $D^* \sim \lambda_F/\sqrt{\alpha}$. Since $s \sim \alpha D^2/\lambda_F^2$, it follows that if $D < D^*$, then spin-orbit scattering is weak, and if $D > D^*$, then spin-orbit scattering is strong. Thus, by reducing the grain diameter we reduce the spin-orbit scattering strength. The effects of spin orbit interaction on energy levels and g-factors in metallic grains have been thoroughly investigated, both experimentally [4, 47, 60, 48]and theoretically [25, 61]. The experiments are in excellent agreement with the theory. However, the spin lifetimes T_1 and T_2 in nanometer scale metallic grains have not yet been investigated before the work presented here.

In the absence of the contribution of the momentum relaxation, we still expect that the spin lifetime in metallic grains is finite. We expect this to be caused by interaction between electron spin and the environment. This interaction could be due to the hyperfine interaction or the spin-orbit interaction coupled to phonon.

2.2 Single Electron Tunneling

2.2.1 Coulomb Charging Effect

The continuous progress in nanofabrication techniques leads to the fabrication of a small conductive dot or island connected to the electrodes by tunneling junctions [62, 63, 46, 49, 47]. The simplest example is a metallic nanoparticle embedded into a tunnel junction as shown in Figure 2.2. When the capacitances of junctions become sufficiently low, the charging energy associated with adding or removing a single electron from the island, is given by

$$E_C = e^2/2C_\Sigma \tag{2.1}$$

where $C_\Sigma = C_1 + C_2$ is the total capacitance of the island and C_1 (C_2) relates to the first (second) tunneling junction.

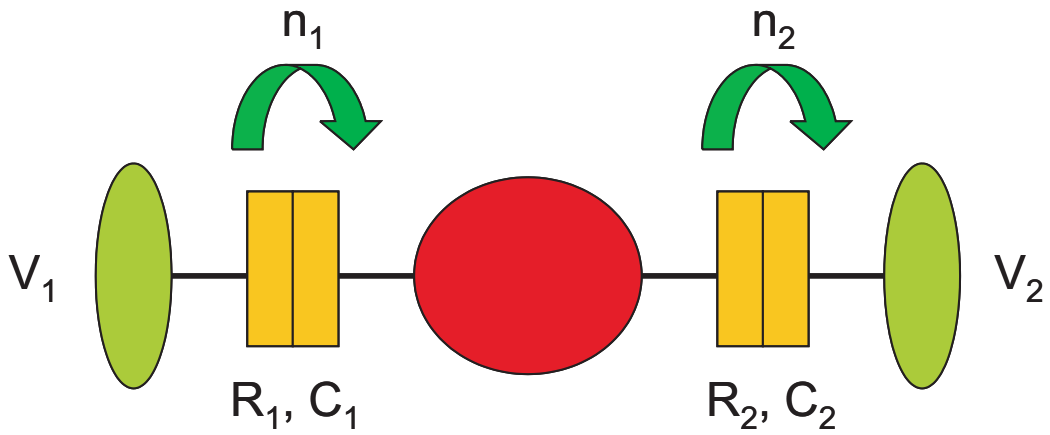

Figure 2.2: Schematic diagram of the type of double junction: a nanoparticle is connected to two leads via two tunnel junctions.

The charging energy is high enough to play a major role at low temperature. Under this simple picture, at low enough voltage and temperature, where eV, $k_BT \ll E_C$, this charging energy introduces a gap for electron tunneling and the system is in the so-called Coulomb blockade regime. In order to observe the Coulomb charging effect, two conditions must be satisfied:

• The charging energy E_C must exceed thermal energy k_BT. Otherwise the electrons will gain enough energy to tunnel through junctions, hence Coulomb blockade is suppressed.

• The total tunneling junction resistance must exceed the quantum resistance $R_Q = h/e^2$ $\simeq$ 25.8kΩ. This condition is obtained from uncertainty principle: for an extra charge on the island, the energy uncertainty $\hbar/RC$ associated with the life time due to the tunneling should be smaller than the charging energy E_C, which ensures that the electron wave function is localized on the island and the quantum fluctuations of charge are negligible.

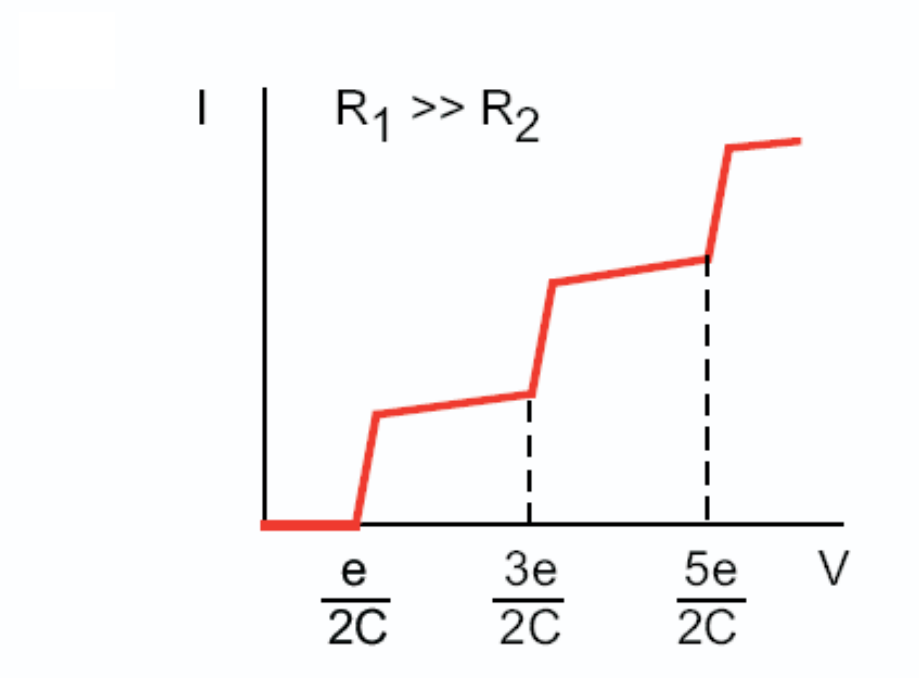

Figure 2.3: Current (I) - bias voltage (V) characteristics of a single electron double tunnel junctions device. It shows both Coulomb Blockade and Coulomb Staircase.

When the bias voltage exceeds the threshold by roughly $V_{th} = e/2C$, the current starts to increase. If the difference between the two junction resistances is large ($R_1 \gg R_2$ or $R_1 \ll R_2$), the current increases stepwise with bias voltage depending on the number of electrons accumulated on the island (see Figure 2.3, where $Q_0 = 0$ and $C_1 = C_2$.). The step-like structure in current vs bias voltage characteristics is called the Coulomb staircase. In general, the Coulomb staircase in a two junctions system can be much more complicated [64]. The $I - V$ curve depends on the fractional residue charge Q_0 on the island and other parameters of the junctions, $C_{1,2}$ and $R_{1,2}$. By following standard procedures explained in

ref [64], one can obtain Q_0, $C_{1,2}$ and $R_{1,2}$ from I-V curve.

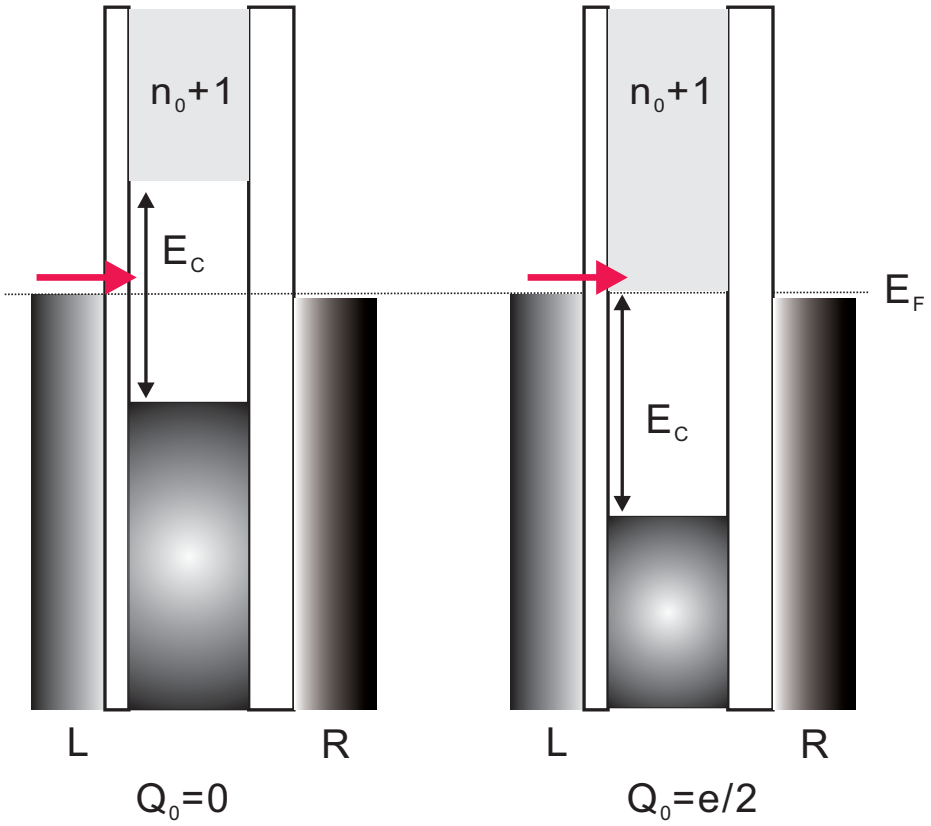

Figure 2.4: Energy diagram depicting the effect of Q_0 on threshold voltages at zero bias. Left, threshold voltage equals charging energy E_C when $Q_0 = 0$; Right, threshold voltage is reduced to zero $Q_0 = e/2$.

Electron tunneling through the island is described by two degrees of freedom. One is a discrete number n, the number of electrons added to the island by tunneling. The island charge changes by $\pm e$ when an electron tunnels onto/off the island. The other degree of freedom is the fractional residue charge Q_0 on the island. Q_0 is a continuous variable, which can be controlled by adding a gate and varying the gate voltage, or it can be changed randomly by warming up and cooling down the sample. Q_0 causes the shift and suppression of Coulomb blockade gap, which is demonstrated in Figure 2.4. Coulomb blockade gap is at its maximum when $Q_0 = 0, \pm e, \pm 2e, \cdots$, and completely suppressed when $Q_0 = e/2, e/2 \pm e, e/2 \pm 2e, \cdots$. Both Q_0 and n are classical variables with well defined values at instant time in the orthodox theory [65].

There are two different type of tunneling processes by which electrons transfer via the

island from one electrode to the other. The first one is sequential tunneling. By applying bias voltage V, electrons tunneling onto then off the island must be energetically favorable, which means energy change ΔE must be negative for each tunneling step. The energy difference is equal to the work done by the power supply. Here the Coulomb blockade is the energy barrier which must be overcome on each of the two successive transitions.

Another tunneling process, co-tunneling, becomes significant when tunneling resistance is comparable to resistance quantum ($25.8k\Omega$). This process, two electrons tunnel in a correlated way due to the energy-time uncertainty relation. An electron tunnels onto the island through one junction, while another electron tunnels off the other junction simultaneously, creating a virtual energy state. Co-tunneling induces a finite current within the Coulomb blockade regime. In this report, we will only study the sequential tunneling. Actually, some of the tunneling thresholds are found in the cotunneling regime, but they have much smaller amplitude.

2.2.2 Energy and Current of Single Electron Tunneling

The double tunneling junction can be described by the model shown in Figure 2.5, both nanoparticle and electrodes are made of normal metals. The total charges on the island (ne) can be expressed as

$$ne = \sum_{i=1}^{2} C_i(V_i - \varphi) \tag{2.2}$$

where $n = n_1$ - n_2 is the excess number of electrons on the island, C_i and V_i are the capacitance and bias voltages of each junction, φ is the electrostatic potential of the island. Then we can find [66]

$$\varphi = \frac{\sum_{i=1}^{2} C_i V_i - ne}{C_\Sigma} \tag{2.3}$$

The total electrostatic energy U is obtained by adding up the field energy of two capacitors.

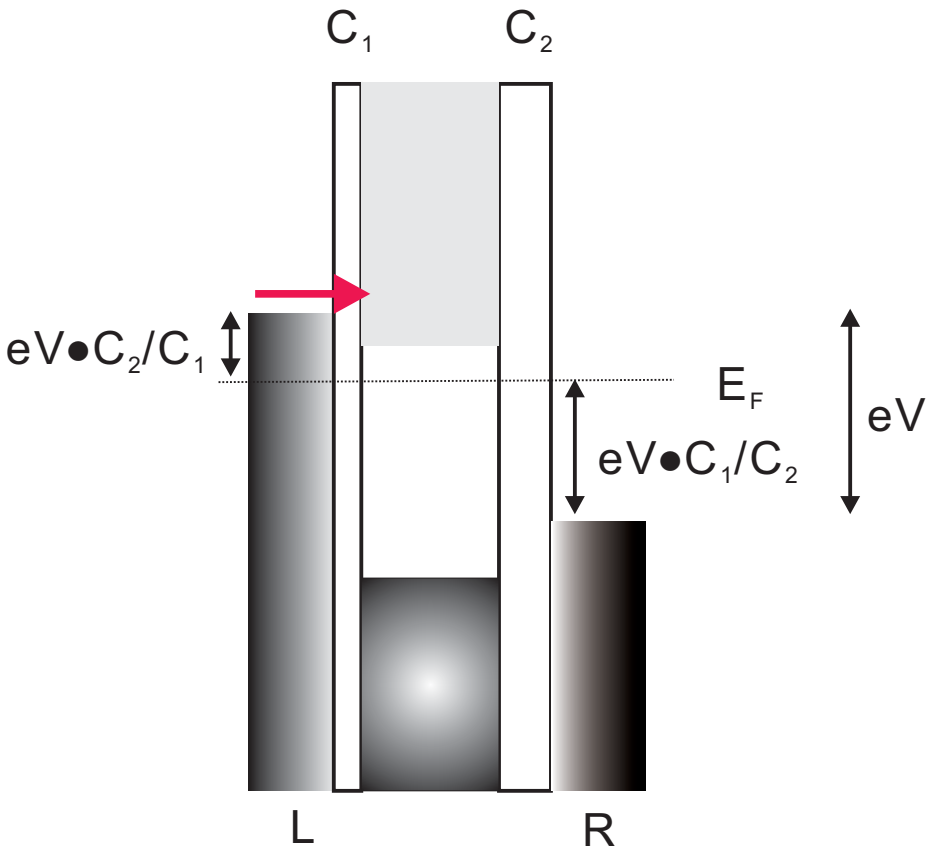

Figure 2.5: Energy diagram for a double tunneling junction device with a positive bias applied to the right electrode. The two junctions, 1 and 2, have different capacitances associated with them.

$$U = \frac{1}{2}\sum_{i=1}^{2} C_i(V_i - \varphi)^2 \tag{2.4}$$

Combining equation 2.3 and 2.4, we have

$$U = A + \frac{ne^2}{2C_\Sigma} \tag{2.5}$$

where A is a constant independent of n. We will neglect A for the rest calculation. In order to get total free energy, we also need find the total work done by the bias voltages. When one electron tunnels onto the island, the work done by junction 1, with total bias voltage $V = V_1$ -V_2, is

$$W_1 = \frac{C_2}{C_\Sigma} eV \tag{2.6}$$

and work done by junction 2 is

$$W_2 = \frac{C_1}{C_\Sigma} eV \tag{2.7}$$

The total free energy E can be calculated as

$$E(n_1, n_2) = U - n_1 W_1 + n_2 W_2 \tag{2.8}$$

where n_1 and n_2 are the number of electrons that tunnel onto island across junction 1 and off island across junction 2 respectively. From equation 2.4, 2.6, 2.7 and 2.8, we get

$$E(m, n) = \frac{ne^2}{2C_\Sigma} - (m + n\frac{C_2 - C_1}{C_\Sigma})\frac{eV}{2} \tag{2.9}$$

where $m = n_1 + n_2$. The fractional residue charge Q_0 was assumed to be zero for all the calculations above. This is true only when chemical potential of metallic island matches the Fermi energy of both leads at zero bias. By including the non-zero Q_0 in equation 2.9, the energy involved in tunneling an electron across junction 1 (junction 2) onto or off the island is given by:

$$\Delta E_1^\pm = \mp\frac{C_2}{C_\Sigma} eV + E_C[1 \pm (2n - \frac{2Q_0}{e})] \tag{2.10}$$

and

$$\Delta E_2^\pm = \pm\frac{C_1}{C_\Sigma} eV + E_C[1 \pm (2n - \frac{2Q_0}{e})] \tag{2.11}$$

For example, an electron tunneling across junction 1 onto the island associates the energy ΔE_1^+, then an electron tunneling across junction 2 off the island associates the energy ΔE_2^-. As we discussed before. Both ΔE_1^+ and ΔE_2^- must be negative to be energetically favorable. We define Γ_1 as the tunneling rate across junction 1, Γ_2 as the tunneling rate across junction 1, and R_1 (R_2) as the resistance of junction 1 (junction 2). The tunneling rate with ΔE is described by [65]

$$\Gamma_i^\pm(\Delta E_i^\pm) = \frac{-\Delta E_i^\pm}{e^2 R_i (1 - e^{\Delta E_i^\pm / k_B T})} \tag{2.12}$$

Now we can determine the current by following the orthodox theory of single electron tunneling [65],[67]. Here, we will only discuss a simple case, in which one electron tunnels onto island from n to n+1 state, then off island from n+1 to n state only through their ground energy state. In the steady state, there is no net charge accumulation on the island, the current across two junctions are equal. We define $\sigma(n)$ as the probability for the island filled by n electrons.

$$\sigma(n)\Gamma(n \to n+1) = \sigma(n+1)\Gamma(n+1 \to n) \tag{2.13}$$

Considering an electron can tunnel onto and off the island across either junction, using 2.13 and the normalization condition $\Sigma_n \sigma(n) = 1$. Finally, the total current will be

$$I = -e \sum_n \sigma(n)[\Gamma_1(n \to n+1) - \Gamma_1(n \to n-1)] \tag{2.14}$$

or

$$= -e \sum_n \sigma(n)[\Gamma_2(n \to n-1) - \Gamma_2(n \to n+1)] \tag{2.15}$$

2.14 and 2.15 are equal due to steady state condition.

2.2.3 Single Electron Tunneling Through Discrete Energy Levels

As the size of the central island (metal nanoparticle) gets smaller, the particle-in-a-box energy level spacing increases with decreasing particle size. When the energy level spacing becomes comparable to the thermal energy, the energy level is quantized. Ralph, Black and Tinkham (RBT) were the pioneer to perform single-electron-tunneling spectroscopy on individual ultrasmall metallic grains [49, 46, 68, 69]. Their research opened a new frontier to study electron correlations in metals. A lot of work have been done since then [27, 28, 47, 70, 60].

Let's consider a simple free electron model of a metal, the spacing between the electronic energy levels (measured at the Fermi energy) is given by [71]:

$$\delta(E_F) = \frac{4E_F}{3N} \tag{2.16}$$

where E_F is the Fermi energy, and N is the number of electrons on the island. We study Aluminum in this report. $E_F(\mathrm{Al}) = 11.7\ meV$ and $n(Al) = 1.81{\times}10^{22}/cm^3$. For a spherical aluminum island with a diameter of $\sim 10nm$, the level spacing $\delta = 0.086\ meV \sim 1K$, which is the temperature accessible in dilution refridgerator.

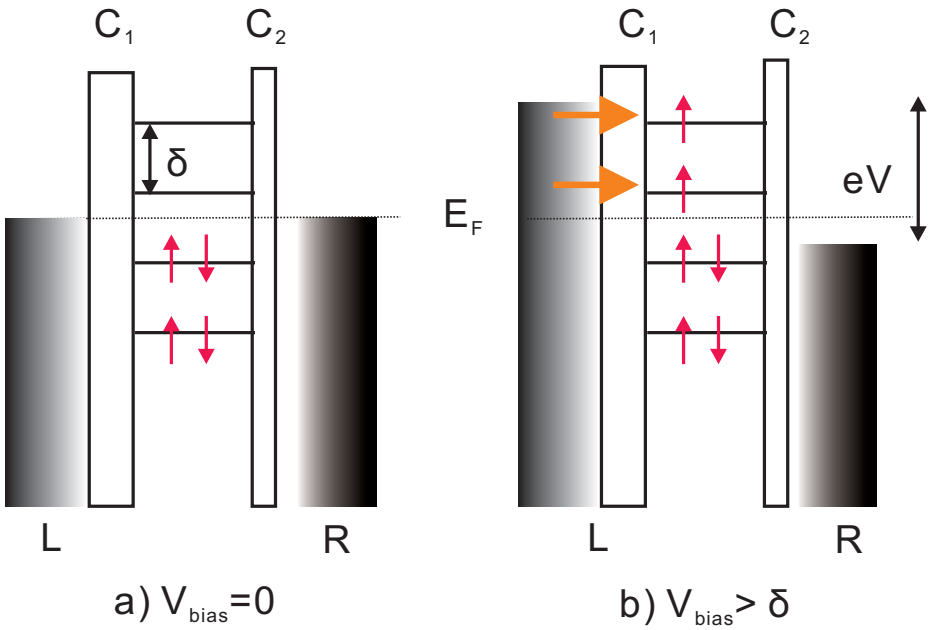

Figure 2.6: Discrete energy level diagram for a double tunneling junction device at a) zero bias voltage, there is no current flow through the device; b) a positive bias applied to the right electrode, the current increases then saturates when the fermi energy of the left electrode pass each level.

In our experiments, the mean level spacing δ ranged from 0.02 to 0.3 meV, which is about 2 orders smaller than charing energy E_C. Other than the conditions to satisfy the Coulomb charging effect, there are three conditions that must be met to resolve the discrete energy levels [72]:

- The thermal energy k_BT must be smaller than level spacing δ. In order to achieve high resolution, one need $\delta > 3k_BT_e$ [73], where T_e is the electron temperature (k_BT_e the thermal energy of the electrons in the leads).
- The tunneling rate (Γ) out of a given discrete state on the grain into lead, must be small enough, $\hbar\Gamma < \delta$, to avoid overlap between neighboring levels.
- For an excited state on the grain with energy ΔE above the ground state to be

resolved, its inelastic relaxation rate Γ_{inel} must be small enough that the corresponding line width is less than the level spacing, $\hbar\Gamma_{inel}<\delta$.

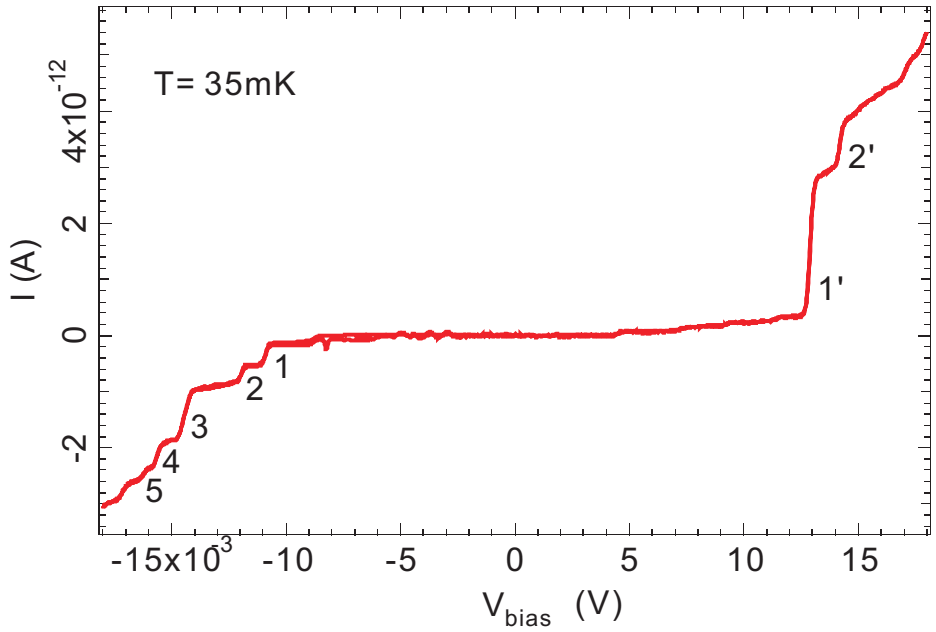

Figure 2.7: Current vs. voltage with the discrete energy levels.

Once all the conditions are satisfied, we can perform tunnelin spectroscopy of the nanopaticle energy levels. The tunneling through such a nanoparticle can be illustrated by energy diagrams. Figure 2.6 shows an energy diagram with discrete energy levels within the nanoparticle. It shows schematically how the energy levels can be detected by measuring the conductance of the device. As shown in Figure 2.6 (a), there is no current flowing through the particle because all the available energy levels are above the Fermi level of both electrodes. When the bias voltage increases (Figure 2.6 (b)), the current increases and saturates when the fermi energy of the left electrode passes the first available energy level of the particle. A plateau can be observed from $I-V$ curve. If we keep increasing the bias, the electron can tunnel via the second empty energy level which has now become accessible. Similarly, once the Fermi energy passes the second level, the current saturates and another plateau appears (Figure 2.7). Eventually, more plateaus appear at higher bias. The position of transitions from one plateau to another corresponds to the position of the energy levels. Measuring the conductance in this way allows us to perform spectroscopy on

the nanoparticle. Bonet and Ralph analyzed in details of the voltage positions, amplitudes, and widths of the current steps due to the quantum states[27, 74].

2.3 Spin Polarized Single Electron Tunneling

2.3.1 FM/I/FM Tunneling Junction

Spin-polarized electron tunneling in magnetic magnetic tunnel junctions ($MTJs$) has become a very active area of research due to possible applications in the magnetic sensor and memory industry [1, 75], as well as by the possibility of observing novel effects [31, 32]. For ferromagnet/insulator/ferromagnet ($FM/I/FM$) single tunnel junction, the pioneer work has been done by *Julliére* since 1975 [76]. Tunneling magnetoresistance (TMR) was observed in that experiment. In the mid-1990's, the observation of large room-temperature TMR [77, 78] motivated enormous increase in the amount of research in this field.

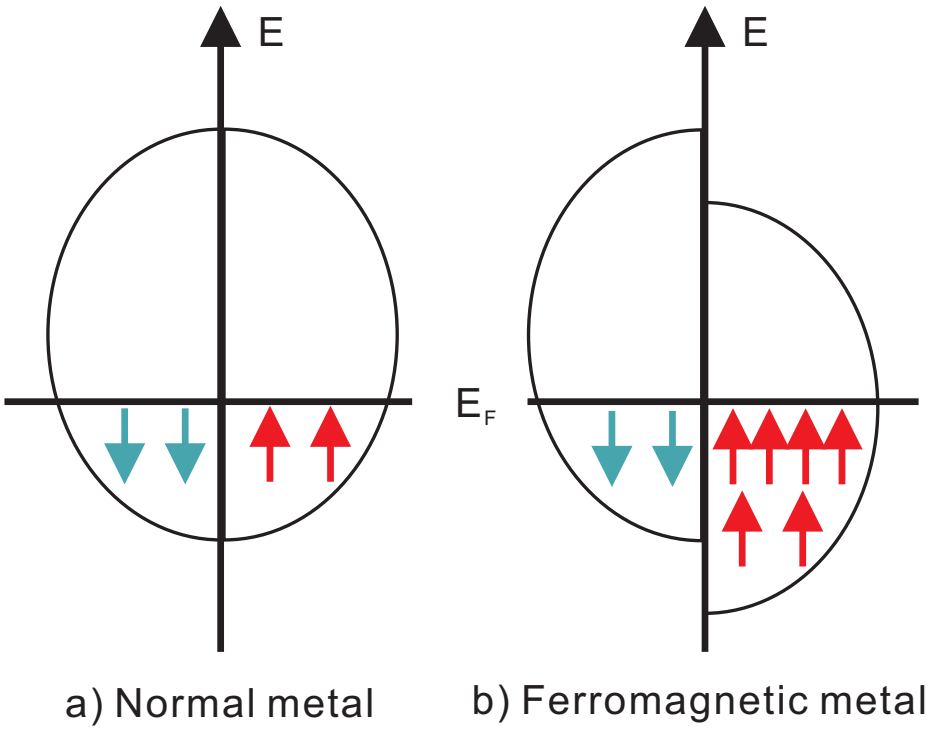

Figure 2.8: Schematics of the difference in the densities of states between a normal metal and a ferromagnetic metal.

The band structure of a ferromagnet is different from that of a normal metal. For normal metal, the density of states for spin-up electrons is equal to that of spin-down electrons (Figure 2.8 a). But the density of states of ferromagnetic metal is asymmetric due to spin-split by the exchange interaction. The majority spin states are shifted with respect to the minority spin states, as shown in Figure 2.8 b. Then polarization arises because of the asymmetry in the density of states at the Fermi energy.

The schematic of density of states for $FM/I/FM$ junction is shown in Figure 2.9. A bias voltage is applied to the MTJ. The main feature of this MTJ is that the resistance depends on the relative orientation of the magnetization in the ferromagnets. This is characterized by the tunneling magnetoresistance, defined as the relative change of the resistance when the magnetizations of the ferromagnets rotate from being parallel to antiparallel.

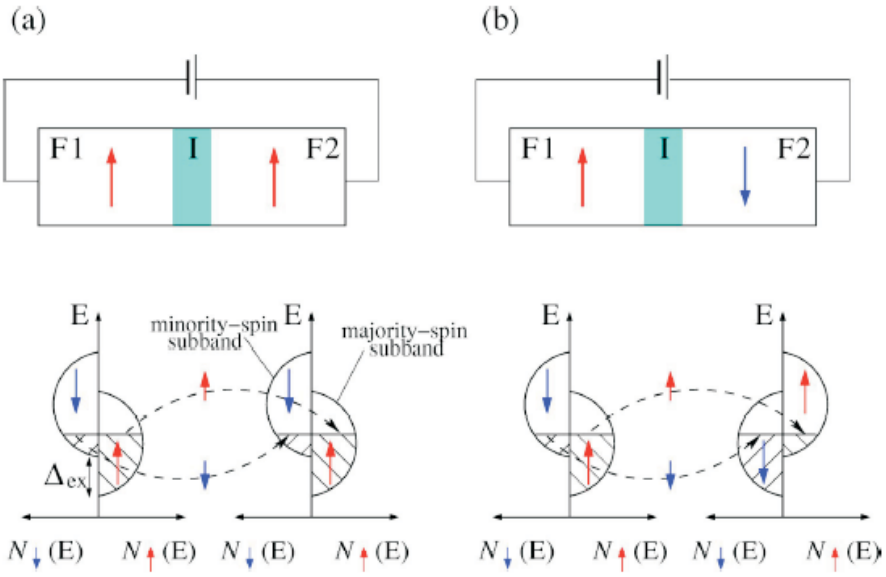

Figure 2.9: Schematic of electron tunneling in FM/I/FM tunnel junctions: The magnetization of two FM layers are (a) Parallel and (b) antiparallel. (Adopted from ref [2])

TMR was explained by *Julliére* within a simple model [76]. *Julliére*'s model served as a useful basis for interpreting a number of experiments on TMR, but the model is too simple to describe all the available experimental data. Nevertheless, Julliere's model gives a basic picture to describe the physics behind TMR. *Julliére*'s model assumes that the tunnel current is proportional to the product of the densities of same spin polarization states

at either side of the tunnel barrier. Also there is no spin relaxation during tunneling.

As shown in Figure 2.9. Electron can only tunnel from left (occupied state at Fermi level) to the right (empty state at Fermi level) with same spin polarization. We define G_P and G_{AP} as the conductance for parallel and antiparallel configuration of two ferromagnetic electrodes respectively. G_P and G_{AP} are described as,

$$G_P \propto N_L^{\uparrow} N_R^{\uparrow} + N_L^{\downarrow} N_R^{\downarrow} \tag{2.17}$$

and

$$G_{AP} \propto N_L^{\downarrow} N_R^{\uparrow} + N_L^{\uparrow} N_R^{\downarrow} \tag{2.18}$$

where $N_i^{\uparrow}$ and $N_i^{\downarrow}$ are the spin up or spin down density of state at Fermi level in either left or right electrode ($i = L, R$).

When right and left electrodes are made of the same material, we have $G_{AP} < G_P$ or, in other words, the resistance is reduced when the magnetization of the electrodes is aligned. Using equations 2.17 and 2.18, the TMR can be described by,

$$TMR = \frac{G_P - G_{AP}}{G_{AP}} = \frac{I_{\uparrow\uparrow} - I_{\uparrow\downarrow}}{I_{\uparrow\downarrow}} \tag{2.19}$$

where $I_{\uparrow\uparrow}$ and $I_{\uparrow\downarrow}$ are the currents in the parallel and the antiparallel magnetization configurations, respectively.

As we mentioned before, the spin up states are shifted with respect to the spin down states. As a result, the density of states at the Fermi level differs between spin up and spin down electrons, as quantified by the polarization ratio P_i,

$$P_i = \frac{N_i^{\uparrow} - N_i^{\downarrow}}{N_i^{\uparrow} + N_i^{\downarrow}}. \tag{2.20}$$

Then the TMR is expressed in terms of the polarization ratio of the two ferromagnetic electrodes:

$$TMR = \frac{2P_L P_R}{1 - P_L P_R}. \tag{2.21}$$

Despite its simplicity, The simple *Julliére* tunneling theory gives good insight into the physical basis of spin polarized tunneling, the *Julliére* model for the tunneling magnetoresistance has continued to be used for interpreting the spin polarization in various MTJ's [7, 79]. However, *Julliére*'s formula does not offer an explicit TMR dependence on junction properties, interface, bias and temperature. Slonczewski gave a more accurate theoretical consideration of TMR [80]. This was the first indication of the fact that the spin polarization of the conductance is not an intrinsic property of the ferromagnets. More sophisticated theoretical work have been performed since then [81].

We will briefly discuss some important features of TMR, such as the TMR dependence on bias voltage and temperature.

- Bias voltage dependence: In most cases, the TMR decreases with increasing bias voltage [76, 77]. Zhang [82] proposed that inelastic scattering by hot electrons at the FM/I interface controlled the voltage dependence. These hot electrons may lose their energy by emitting a magnon and resulting in the reduced TMR values. Moodera [83] suggested that part of the decrease in TMR can be attributed to the excitation of magnons, thereby randomizing the tunneling electron spins and increasing the total conductance.

- Temperature dependence: In all tunnel junctions the TMR decreases with increasing temperature. Compared to non-magnetic junctions, the temperature dependence of the tunnel resistance for $MTJs$ is much stronger [84]. As in ref [84], which assumed that the tunneling spin polarization ratio P decreases with increasing temperature due to spin-wave excitations, as does the surface magnetization. Moodera [83] attributed the temperature dependence of TMR to the temperature dependence of the surface magnetization of the FM electrodes, which was related to the decrease of the surface magnetization

The TMR also depends on the insulating barrier, interface properties and so on. For more details, please see ref [81].

2.3.2 FM/I/N/I/FM Double Tunneling Junction

So far we have discussed single electron tunneling through double tunneling junctions with normal metal electrodes, and direct tunneling between two ferromagnetic electrodes. When combining single electronics and spin electronics, we see an interplay between Coulomb blockade and spin dependent tunneling. Some interesting TMR phenomena come in. Spin dependent single electron tunneling has been studied in both co-tunneling and sequential tunneling regimes.

As we discussed in section 2.3.1, co-tunneling happens when tunneling resistance is comparable to the resistance quantum ($25.8k\Omega$). Spin dependent co-tunneling has been studied both theoretically and experimentally in the Coulomb blockade region [32, 35, 85, 86]. The enhanced TMR in the co-tunneling regime has been predicted for either granular films [87] or double tunnel junctions [35]. According to ref [35], TMR is enhanced in the co-tunneling regime to at least twice the TMR in the sequential regime. This enhanced TMR has been observed in experiments.

In this report, we will focused on the sequential regime. Phenomena in sequential regime are discussed based on the orthodox theory of single electron tunneling. Theoretical works were first performed by Barnas and Fert [33, 34]. They predicted that novel TMR phenomena such as modification of the spin-dependent tunneling probability associated with a Coulomb staircase gives rise to a TMR peak around the step point of the staircase. A peak appears at each step resulting in the oscillation of TMR as a function of the bias-voltage. In principle, the step heights are determined by the resistance of each junction, so different step heights are expected in the parallel and antiparallel configurations. This, combined with the non-linearity of the steps, would give rise to oscillations as a function of applied voltage in $F/I/F/I/F$ and $F/I/F/I/NM$ double junctions.

We investigated the $FM/I/N/I/FM$ double tunneling junction in our work. The energy diagram of such a $FM/I/N/I/FM$ double tunneling junction is shown in Figure 2.10. Once spin accumulation [29, 33, 37, 41] in the island is considered, characteristic TMR behavior due to the spin accumulation effect was predicted: the difference the chemical potential in

the central island between parallel and anti-parallel configuration leads to nonzero TMR with periodic oscillation.

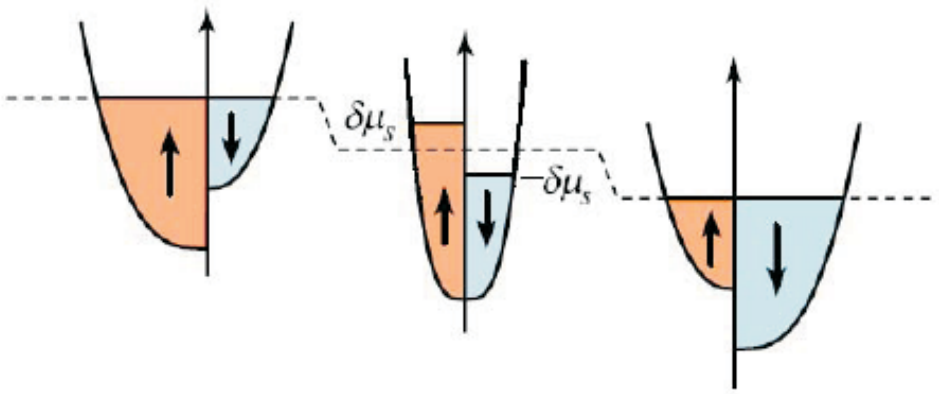

Figure 2.10: Schematic of electron tunneling in FM/I/N/I/FM double tunnel junctions with the magnetization of two FM layers are antiparallel. A positive bias is applied to the right lead.

Electrical spin injection and detection in normal metals was pioneered by Johnson and Silsbee [29]. In spin injection, a nonequilibrium density of electron spins is generated in a normal metal by electron injection from a ferromagnetic reservoir. Spin injection leads to a difference between the chemical potentials of electrons with spin-up and spin-down inside the normal particle. This spin accumulation in the normal metal layer is detected by a second ferromagnetic reservoir connected electrically to the normal metal. The voltage measured by the detector is proportional to the component of the induced nonequilibrium magnetization along the direction of the magnetization in the detector.

Johnson and Silsbee obtained the spin relaxation length and the spin-flip scattering time by applying a weak magnetic field perpendicular to the magnetization direction. The perpendicular field resulted in precessions of injected electron spins. As a result, the detector voltage displayed damped oscillations with the perpendicular field, known as the Hanle effect. The period of the oscillations corresponded to the average transit time between the injector and the detector, and the characteristic field for destruction of the spin polarization was $(\gamma T_2)^{-1}$, where γ was the gyromagnetic ratio.

By fitting these oscillations with the functional forms derived in Ref. [29], it was possible

to determine the transverse spin-relaxation time T_2 in the normal metals and the degree of spin polarization P in the ferromagnetic reservoirs. The original measurements were done in single crystal aluminum bars. At 4.2 K, the spin relaxation length was $\simeq 500\mu s$ and the spin relaxation time was $\simeq 10ns$.

Recently, Jedema et al. have extended the spin injection and detection technique to micron scale metallic thin film devices [23, 56, 88]. The spin-detection signal was greatly enhanced through the use of tunneling barriers between ferromagnetic reservoirs and the normal metal [89] and through small sample size. The spin relaxation length and the degree of spin polarization in the ferromagnetic leads were determined through the Hanle signal. The typical value for T_2 at 4.2 K was found to be $0.1ns$, which is significantly shorter than T_2 obtained by Johnson and Silsbee.

The difference between T_2 at $4.2K$ in single crystals and thin films was explained by the fact that the elastic mean free path in thin films is much shorter than that in single crystals (primarily because of the surface scattering). [56] In this case, the Elliot-Yafet relation gave spin- orbit scattering times in rough agreement with the observed values, showing that the dominant spin relaxation mechanism in Al at $4.2K$ is given by momentum scattering.

In addition, Jedema at al. studied "all-metal mesoscopic spin valves" [23, 56]. In these devices, the electrical current follows between two ferromagnetic reservoirs via a micron-scale normal metal bridge. The resistance of the bridge depends on the relative orientation of the magnetization of the ferromagnetic reservoirs. The difference between the currents in parallel and antiparallel orientations (at fixed voltage) is explained by the spin accumulation within the nanoparticle.

The spin accumulation is also confirmed in the array of normal metal grains [7], where spin-polarized current through ensembles of nanometer Al grains were studied. The spin-coherence time measured using the Hanle effect is of order ns. The dephasing is attributed to electron spin precession in local magnetic fields. Tunneling magnetoresistance is strongly asymmetric with current direction, which was attributed to the asymmetry in electron dwell times and spin relaxation.

Most recently, spin accumulation in Au nanoparticles have been performed [42]. The

negative TMR was observed. The negative TMR could not be explained in the framework of *Julliére* model, and was attributed to the spin accumulation in Au nanoparticles in an $FM/I/Au/I/FM$ structure. But no energy level quantization was studied, and data was not sufficient to analyze spin relaxation time.

In this letter we report on spin-polarized tunneling via discrete energy levels of single aluminum grains, which are weakly coupled to ferromagnetic electrodes. There are some issues which need to be considered to make working samples.

We investigate the spin-transport in individual nanometer-scale metallic grains focusing on spin relaxation effects. A long spin relaxation time is expected for such a nanoparticle [12, 13]. As discussed above, spin relaxation in normal metals is explained by spin-orbit interaction. In normal metal grains, spin-orbit interaction causes significant perturbation of the electronic eigenstates by mixing spin-up and spin-down states. The strength of spin-orbit interaction increases with atomic number Z. So we choose the metal with low atomic number to reduce spin-orbit interaction. Aluminum, with a Z of 13, is selected for our research.

In order to resolve the energy levels at dilution refrigerator temperatures, the diameter of the grain must be smaller than about $10nm$. In addition, we want to prevent superconductivity in the grains. This is achieved by making the grains smaller, because when the level spacing becomes larger than the superconducting gap in Al, the superconductivity disappears [49].

To study the interplay between spin polarization and single electron tunneling, we want to have the spin polarized signal as high as possible. First we need ferromagnetic electrodes with high degree of polarization P of the electrons at the Fermi level. P of $Ni_{0.8}Fe_{0.2}$ (Py), Fe and Co are 32%, 40% and 35% respectively [90]. Among them, we pick Py due to its relative low intrinsic field $\simeq 1T$ and relatively slow oxidation. Intrinsic field introduces smaller fringing field to the nanoparticle. Second, a good tunneling junction is required. Al_2O_3 is the best choice to date.

In order to observe spin relaxation of electrons in the particle-in-a-box states, we would like the coupling between particle and electrodes to be as small as possible. This reduces

tunneling rates, so they can be comparable to spin relaxation rates. Experimentally, the largest resistance we can measure reliably is of the order of $G\Omega$, which sets the lower limit on the tunnel coupling. We use e-beam lithography to make samples. It's nearly impossible to make a junction containing only one nanoparticle. We select the sample with the highest resistance , as they have the smallest overlap. Due to surface roughness and particle size variation, we can get a tunneling junction in which one particle connects to the thinner Al_2O_3 than other particles in the junction. Since the tunneling rate depends on barrier thickness exponentially, most current will flow through this single particle.

CHAPTER III

EXPERIMENTS

The purpose of this chapter is to summarize the experimental techniques that were used to prepare, modify and characterize the spin polarized single electron transport samples. In principle, electron beam lithography was used to define the nano-scale devices, and shadow evaporation technique was used to deposit nanoparticles, different metallic and insulating layers. Then samples were pre-tested at room temperature ($\sim 300K$) and liquid Helium temperature ($\sim 4.2K$). Finally, we pick high resistance ($\sim G\Omega$) samples, which have the smallest overlap, and show Coulomb-blockade, discrete levels, and TMR signals.

3.1 Sample Preparation

3.1.1 Electron Beam Lithography

Photolithography dominates the industry mainly due to its high throughput. But the smallest feature by photolithography is limited by the wavelength of the light that is used, and the ability of the reduction lens system to capture enough diffraction orders from the illuminated mask. The minimum feature size (d) that a projection system can write is approximately:

$$d = 1.22\lambda\frac{f}{a}. \tag{3.1}$$

where λ is the wavelength of photon, f is the focal length and a is the diameter of the lens.

Some techniques are developed to improve the resolution, such as phase shifting mask (PSM) and optical proximity correction (OPC) [91]. Photolithography has extended to deep submicron range, but equipment and mask are costly.

Compared to photolithography, electron beam lithography (EBL) has some advantages which include the generation of submicron pattern, greater depth of focus and no mask needed. Limited by its low throughput, EBL is mostly used in research and to make photomasks.

The resolution is not limited by diffraction for EBL ($\lambda = 0.03nm$ at $41keV$). However, the resolution of an EBL may be limited by other factors, such as electron scattering in the resist and by various aberrations in its electron optics. The scattering of electrons may be forward and backward. Scattering occurs when electrons interacts with the resist and substrate atoms. This electron scattering broadens the diameter of the incident electron beam as it penetrates the resist and substrate, and gives the resist unintended extra doses because of back scattering. Thus, scattering effects causes wider patterns than ideal resolution. Since the dose applied to resist is the sum of irradiations from all the neighboring areas, a phenomenon known as the proximity effect, the minimum size is constrained.

3.1.1.1 Electron Beam Resists and Spin Coating

A silicon wafer with thermally oxidized surface is used as substrate. Samples fabricated on this substrate are electrically isolated to the environment. Contamination on the surface will lower the yield of samples, so extra care need to be taken. The wafer is cleaned ultrasonically in trichloroethylene (TCE) followed by acetone and isopropanol (IPA) for 5 minutes in each solution. Then the wafer is blown dry by dry air.

Electron resists are polymers. A chemical or physical change is induced in the resist by high energy electrons. This change allows resist to be patterned. We use both polymethyl methacrylate, $PMMA$, with 950000 molecular weight in chlorobenzene (2%) and copolymer methacrylic acid ($MMA-MAA$) in Ethyl Lactate (6%). Those polymers are positive resists with different sensitivities to irradiation. For a positive resist, chemical bonds are broken by electrons attacking. As a result, the molecule weight is reduced in the exposed area, which can be dissolved in a developer solution.

Copolymer $MMA-MAA$ is used in combination with $PMMA$ to make a bi-layer. $MMA-MAA$ is the bottom layer and $PMMA$ is the top layer. The wafer is cleaned by acetone and IPA at 5500 RPM for 20 second on the spinner. Next, the $MMA-MAA$ is spin coated at 1000 RPM for 90 seconds. The thickness of the bottom layer is about 250 nm. Wafer is then baked at 150 C for 10 minutes on the hot plate. Then the $PMMA$ is spin coated at 5500 RPM for 60 seconds. The thickness of the top layer is about 100 nm. It is then baked at 180 C for another 10 minutes.

Such a bi-layer structure serves two purposes: 1) Applying the proper dose, because of different sensitivity to electrons irradiation, the top layer generates the designed pattern while the bottom layer has larger size than that of top layer. An undercut is formed, which is used for shadow evaporation. 2) The undercut is helpful for liftoff after deposition.

3.1.1.2 Samples Patterning

We use a Scanning Electron Microscope (SEM) $JSM5910$ to define patterns on polymers. The patterns are designed by $DesignCAD\ LT2000$ in $DC2$ files. Nanometer Pattern Generation System ($NPGS$) developed by Dr. Nabity is used to control electron beam writing. $NPGS$ software creates a $rf6$ run file for a $DC2$ file. All the electron beam writing parameters are included in this $rf6$ file. The critical parameters include beam current, dosage, magnification, working distance and offset. Some other parameters, such as line spacing and center to center distance can be adjusted to save writhing time.

The physical structure includes three layers: 1st layer) Two micrometer size triangle are separated with a small gap in the order of 100 nm; 2nd layer) an intermediate layer ($\sim 50\mu m$) connects the first layer and the third layer; 3rd layer) Source and drain contact pads are in the order of mm. The contact pads are designed into strip structure to save writing time.

The shape of the device is chosen to have the stable magnetic moments for both parallel and antiparallel configuration at zero applied field, and to minimize the stray field by

magnetic electrodes. As we mentioned earlier, it is challenging to make a junction only containing one nanoparticle based on EBL with a $40nm$ resolution. But with surface roughness and particle size variation, most current may flow through a single particle. Such a working sample can't be precisely controlled. So many samples with varied gap sizes need to be made.

In general, 30 patterns are made automatically in a 5 by 6 array. The gap sizes vary around $200nm$ from column to column. The distance between patterns is $2.5mm$. In order to get the best resolution, the electron beam has to be very well focused on the surface. We make a contamination dot and focus on the dot at each corner of the chip. The electron beam parameters for those focal points are saved to a batch file, which then calculates and controls the electron beam parameters through the whole chip.

Based on the resolution requirement, the writing parameters for those three layers are set differently. One should keep in mind that those parameters may differ from wafer to wafer. A couple of runs to characterize all the parameters is highly suggested for each new spin coated wafer. A detailed set of writing parameters are described below for a single sample.

The working distance is $20mm$, and the acceleration voltage is $30kV$ for all three layers.

The first layer: The magnification is 1000. The beam current is $10pA$. The offset is zero. The area dose is $177\mu c/cm^2$. The configuration parameter (CP) is 2000. The CP controls the beam current, and needs to be set only for auto sample writing and reset for each run. For manual sample writing, one uses front panel to set the right beam current. The rest of the parameters, such as dwell time, are set automatically afterwards.

The second layer: The magnification is also 1000. The beam current is $100pA$. The offset is $0.4\mu m$ in x direction only. This little offset is caused by a larger beam current than that of the first layer. The area dose is $275\mu c/cm^2$. The CP is 830.

The third layer: The magnification is 60. The beam current is $9000pA$. The offset is $40.5\mu m$ in x direction and $5\mu m$. The large offset is due to intrinsic optical properties for different magnifications. The area dose is $450\mu c/cm^2$. The CP is 110. The third layer is the most time consuming, taking 90% of the time to write a sample. In order to save time,

we increase both line spacing and center to center distance to $300\mu m$.

Thirty EBL patterns are made within 2 hours for each run. Then the chip is developed in 1:3 $MIBK$: IPA for 12 seconds. The developing time is very critical here. After developing, rinse with IPA and blown with dry air.

A suspended nano-bridge is formed (Figure 3.1), The sizes of nano-bridges vary around $200nm$ from column to column. The nano-bridge serves as a mask for shadow evaporation.

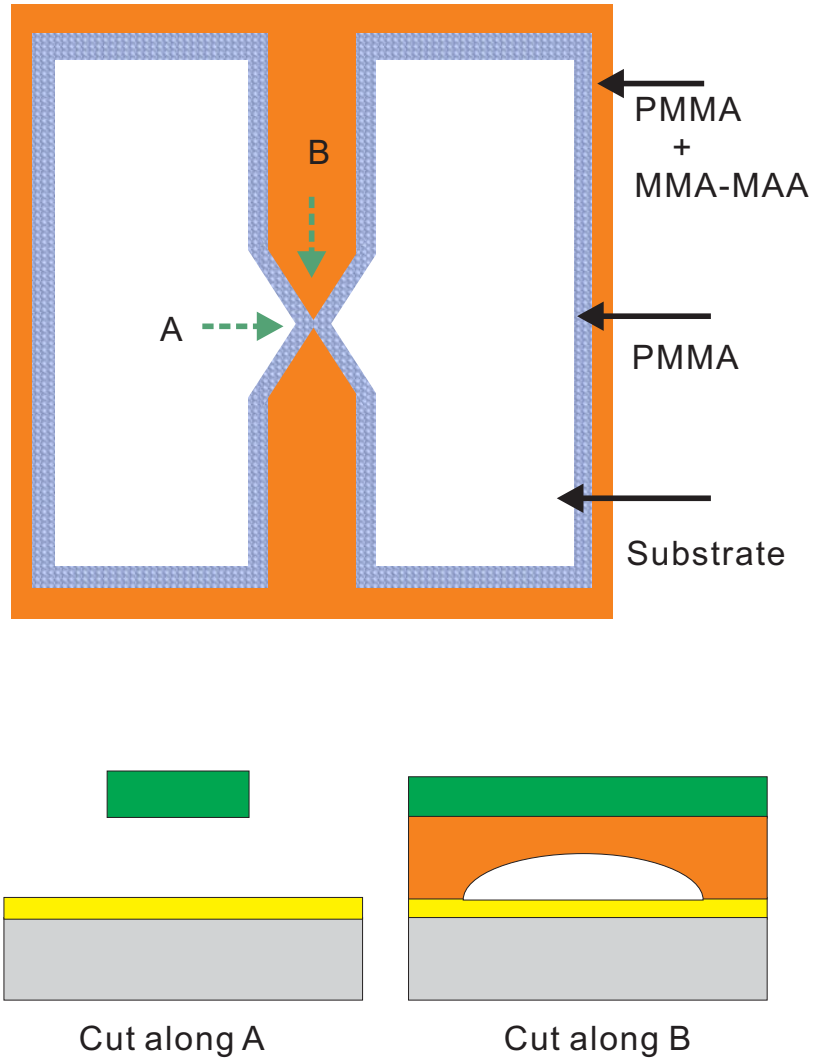

Figure 3.1: Pattern written by electron beam lithography: Top view) Electron beam lithography over a 2-layer resist, a suspended small bridge is formed; Side views) Bottom left shows the suspended bridge When cut sample along direction A; Bottom right shows a channel when cut along direction B.

3.1.2 Shadow Evaporation

To fabricate the nanoparticles, different metallic and insulating layers are deposited with shadow evaporation, similar to the technique described previously [47]. An EBL patterned resist bridge is placed $250nm$ above the silicon wafer; this bridge acts as a mask. Sample deposition steps and device geometry are sketched in Figure 3.2.

Metals are deposited by using a thermal evaporator. Samples are held on a self made rotating stage which can be attached to the fixed stage inside the evaporator. Two desired angles are controlled by stops. Al and Py ($Ni_{0.8}Fe_{0.2}$) are loaded into alumina coated tungsten boats. The vacuum chamber is cryo-pumped to its base pressure, $4 \times 10^{-7} Torr$ in our case. Under such a low pressure, the mean free path (longer than 10 m) of metal vapor is much longer than the distance between boat and sample ($\sim 30cm$). So metal atoms can reach the substrate without reacting with or scattering against other gas-phase atoms in the chamber, and reduce the incorporation of impurities from the residual gas in the vacuum chamber.

First(Figure 3.2-1), we heat up the Py, when the deposition rate reaches 0.2 nm/s, we open the shutter and deposit $11nm$ Py at onto oxidized silicon substrate at $4 \times 10^{-7} Torr$ base pressure, measured near the gate valve, along the direction indicated by the arrow. Then we rotate the sample by 36 degrees without breaking the vacuum and deposit aluminum for 1 second at a rate 0.2 nm/s. The Py layer is now covered with a seed layer of aluminum with nominal thickness $0.2nm$. This thin aluminum layer will be oxidized later and prevent bottom Py layer from oxidation a little. The oxidized seed layer also provides a better contact with insulating layer (Al_2O_3).

The typical oxygen pressures used to thermally oxidize aluminum surfaces in tunneling junctions is described in reference [46], in which Al nanoparticles were deposited at base pressure, then oxidized in oxygen at 0.1 $Torr$ for ~ 2 minutes. This process created $\sim M\Omega$ resistance samples. The oxide thickness is $\sim 1nm$ according to [46]. We were trying to follow the oxidation procedure by [46], but with $\sim M\Omega$ resistance tunneling junctions, it's hard to get a single nanoparticle device.

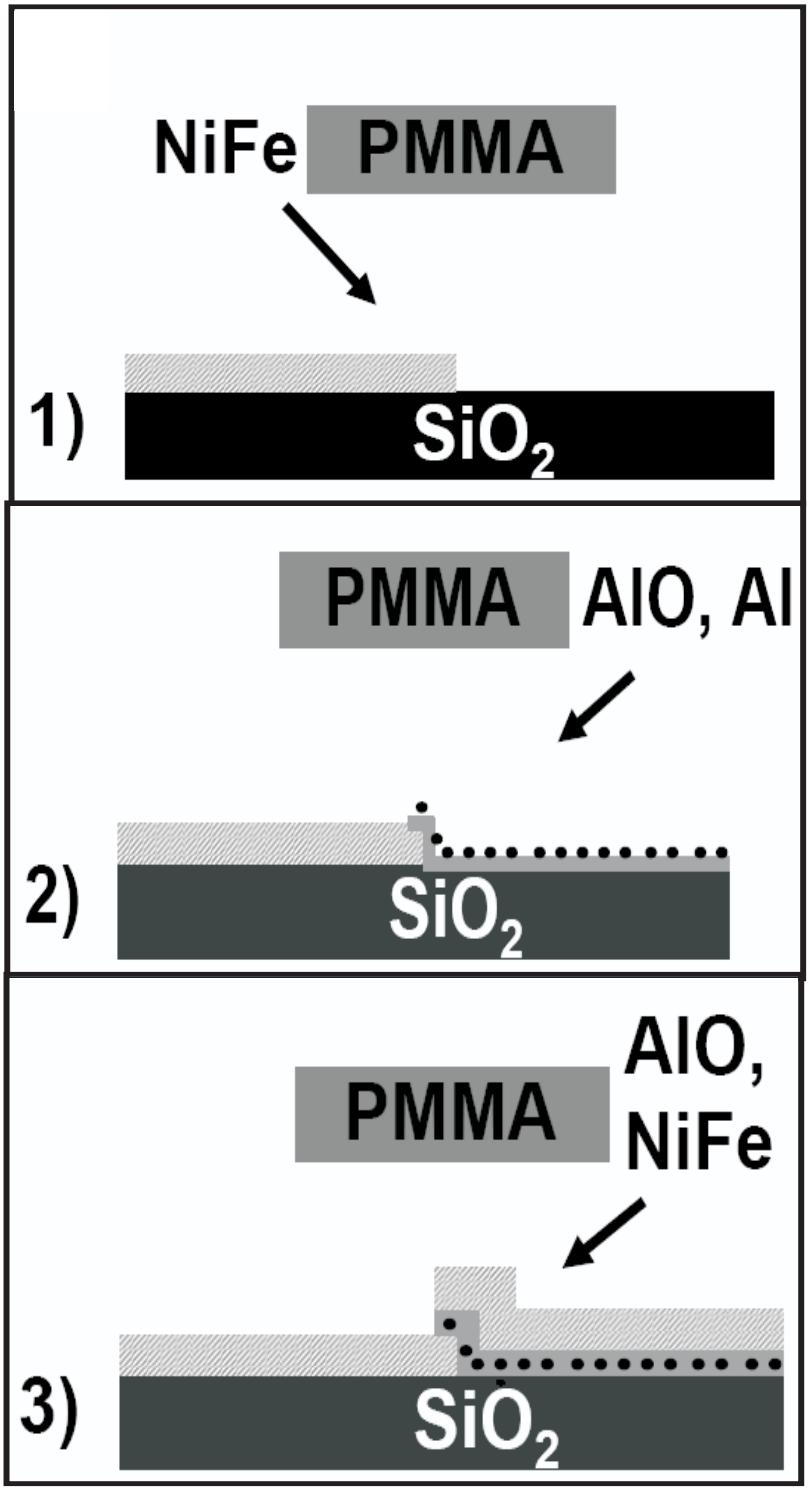

Figure 3.2: Sample deposition steps

To obtain higher resistance tunneling junctions, the reactive evaporation technique was used [47]. The junctions were of high quality and they displayed well resolved Coulomb-Blockade steps and discrete energy levels of the Al grain at low temperatures. In reactive evaporation, oxygen is introduced into the chamber while aluminum is evaporated. The chamber is continuously pumped by the cryopump. With a flow rate of $200sccm$ (standard cubic centimeters per minute), oxygen pressure is stabilized at 2.5×10^{-5} $Torr$ after 30 seconds.

Py layer with a $0.2nm$ seed layer of aluminum is exposed to oxygen during the initial 30 seconds. The oxygen pressure of 2.5×10^{-5} is four order smaller than that of thermally oxidation [46], and the oxidation time is shorter than 2 minutes. So the thickness of the surface aluminum oxide in our case must be smaller than $1nm$. Thus, we expect that the seed aluminum layer of nominal thickness $0.2nm$ is oxidized here and provides some protection of Py surface from further oxidation.

When the pressure is stabilized, we deposit $1.2nm$ of Al_2O_3, at a rate of $0.35nm/s$, at an oxygen pressure of 2.5×10^{-5} $Torr$. Now, oxygen flow is shut down. Remaining oxygen is pumped out of the chamber. When pressure decreases to the 10^{-7} $Torr$ range, we deposit a $0.6nm$ Al onto Al_2O_3, at a rate of $0.35nm/s$, as shown in Figure 3.2-2. Al forms isolated grains with a typical diameter of $5nm$. The grains are displayed by the scanning electron microscope (SEM) image in Figure 3.3.

Al grains are exposed to oxygen before deposition of the top oxide layer, at 2.5×10^{-5} Torr for 30 seconds. Al grain surface is then oxidized from above, but we expect that the Al_2O_3 thickness is considerably smaller than $1nm$, as discussed above. Additionally, the grain surface may be oxidized from below by adsorbed oxygen on the underlying Al_2O_3 surface. Thus, the average size of the metallic grains should be smaller than the grain size (shown in figure 13) by up to $\sim 1nm$.

Finally we deposit another $1.2nm$ layer of Al_2O_3 by the reactive evaporation and top it of by an $11nm$ thick film of Py (Figure 3.2-3).

We make many samples on the same silicon wafer. The width of the suspended bridges vary around $200nm$. After shadow evaporation, we get overlaps which vary from 0 to $50nm$.

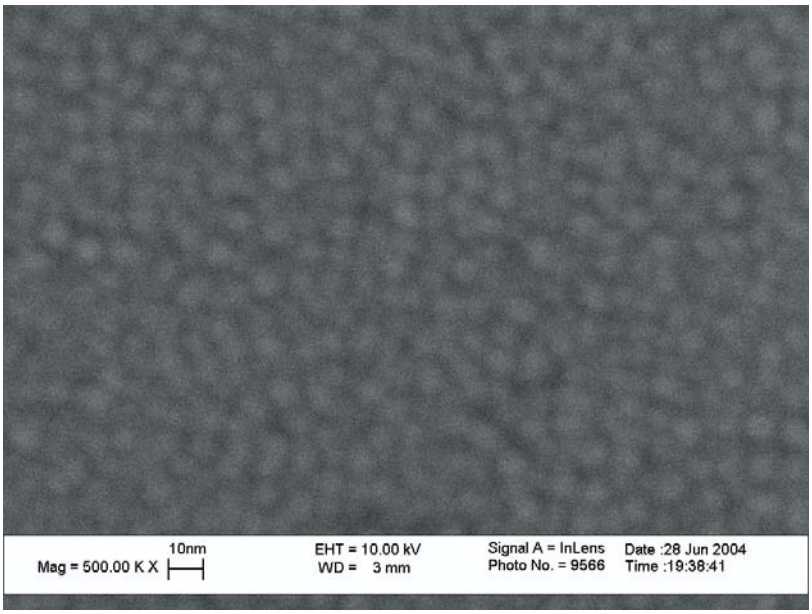

Figure 3.3: SEM image of nanosize aluminum grains. The aluminum grains are in different sizes. The average grain diameter is $\sim 5nm$.

The devices with the highest resistance are selected for low temperature measurement, since they have the smallest overlap. Figure 3.4 is a large view of SEM images of a typical device. The geometry of the device (large angle triangle) favors stable magnetic moments for both parallel and antiparallel configuration at zero applied field. Figure 3.5 is the close view of SEM images of a typical device. The bright area in the middle of Figure 3.5 contains nanoparticles which are weakly coupled to source and drain by tunneling junctions. The area of the overlap is about $500nm^2$, which contains $\sim$ 10 nanoparticles. Due to surface roughness and particle size variation, we can get a tunneling junction in which one particle connects to the thinner Al_2O_3 than other particles in the junction. Since the tunneling rate depends on barrier thickness exponentially, most current will flow through this single particle.

3.2 Sample Measurements

We investigate spin-polarized tunneling via discrete energy levels of single aluminum grain in this report. In order to get discrete energy levels of single aluminum nanoparticle, we

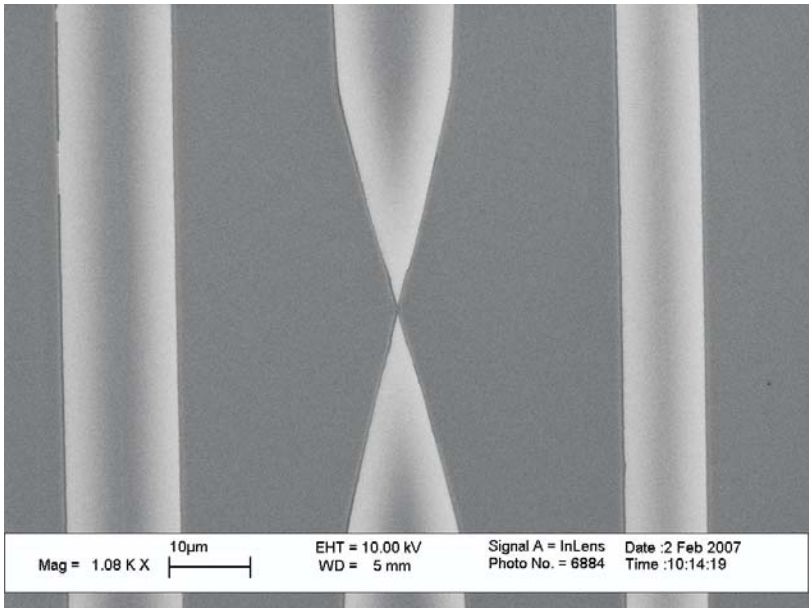

Figure 3.4: The large view of *SEM* images of a typical device. The geometry of the device favors stable magnetic moments for both parallel and antiparallel configuration at zero applied field.

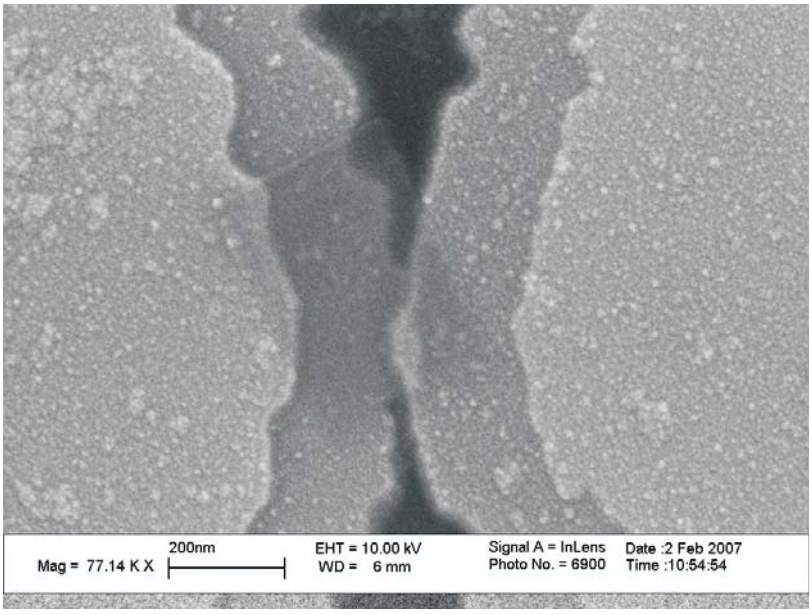

Figure 3.5: The close view of *SEM* images of a typical device. The bright area in the middle contains nanoparticles which are weakly coupled to source and drain by tunneling junctions.

cool down samples to $\approx 0.035K$ base temperature by a dilution refrigerator. The operation of dilution refrigerator is costly and the yield of working samples is quite low, so we preselect samples for cool down by the following procedure: sample resistance measurement at room temperature $\Rightarrow$ $I-V$ and TMR measurements at $4.2K$ $\Rightarrow$ detailed electron transport measurements at $\approx 0.035K$ base temperature.

Our single nanoparticle tunneling samples are relatively robust to mechanical shock, but they are extremely sensitive to electrostatic discharge. One should always ground oneself when dealing with the samples. Samples are easier to blow in winter because of dry air. We use a humidifier to reduce charges in the air when loading samples. A flaming candle is also used to reduce charges in the air. These methods are trivial but very efficient.

3.2.1 Measurements at Room Temperature

Samples are tested at room temperature quickly, using a basic setup for resistance measurement. A function generator (Stanford research Systems $DS335$) supplies the DC bias voltage to the sample, and the resulting current and voltage signals of the sample are detected by a low noise $Ithaco$ 1211 current amplifier and Stanford research Systems $SR560$ voltage amplifier respectively. A micro manipulator is used to make contact with the sample. A voltage divider is used to confine the voltage applied to our sample, the highest voltage across the sample should be lower than $50mV$ to protect the sample from blowing.

30 samples can be tested in one hour at room temperature. We put those samples in four categories upon their resistances: 1) low resistance samples ($< 10k\Omega$) whose $I-V$ curve is linear at $4.2K$, these samples most likely have metallic short. 2) medium resistance samples ($< 10k\Omega < R < 10M\Omega$ whose $I-V$ curve is nonlinear at $4.2K$, with high resistance near zero bias. In this case the Coulomb blockade is not complete and with smooth steps. This occurs mostly due to multiple particles in parallel connecting the two electrodes. 3) possibly good samples with a resistance ranging between $\sim 10M\Omega$ and $\sim 5G\Omega$. The majority of

samples ($> 80\%$) exhibit Coulomb blockade at $4.2K$. These possibly good samples will be tested at base temperature. 4) Extremely high resistance ($> 5G\Omega$) samples, indicating that there is no overlap or no nanoparticles embedded, or those insulating layers are too thick.

3.2.2 Measurements at Liquid Helium Temperature

Each sample is mounted to a special sample holder whose terminals are shorted to each other. The sample is protected by those shorted terminals, an accidently applied voltage will drop across the terminals rather than the sample. The possibly good samples are then loaded onto self-made dipstick and dipped into liquid helium slowly. It's take about 10 minutes to immerse the samples into liquid helium completely and reach $4.2k$ temperature. There is a solenoid superconducting magnet attached to the end of the dipstick. The magnetic field is 1 $Tesla$ at 60 $Amperes$. The magnet must be completely immersed into liquid helium to avoid heating.

The measurement setup is shown in Figure 3.6. We use Stanford Research Systems $DS335$ function generator to programming bias voltage and applied magnetic field. We measure the current through the sample with low noise $Ithaco$ 1211 current amplifier, the input of the current amplifier is connected to a triaxial cable, which ensures no noise introduced from the ground loops. A $LabView$ program is developed to collect all the data onto a computer. The magnet is powered by a $Kepco$ power supply, the highest field we can get is 0.33 $Tesla$.

We classify our samples into three categories based on I-V curve and TMR at $4.2K$.

- Multi-particle sample: In this case the Coulomb blockade is smooth and the I-V curve lacks sharp features. Basically [92], when current is carried by several particles, each of which has its own set of resistances, capacitances and the fractional residue charge Q_0. The randomness of those junctions parameters smoothes out the Coulomb blockade.

- Single-particle sample with no TMR: More than half measured samples show Coulomb

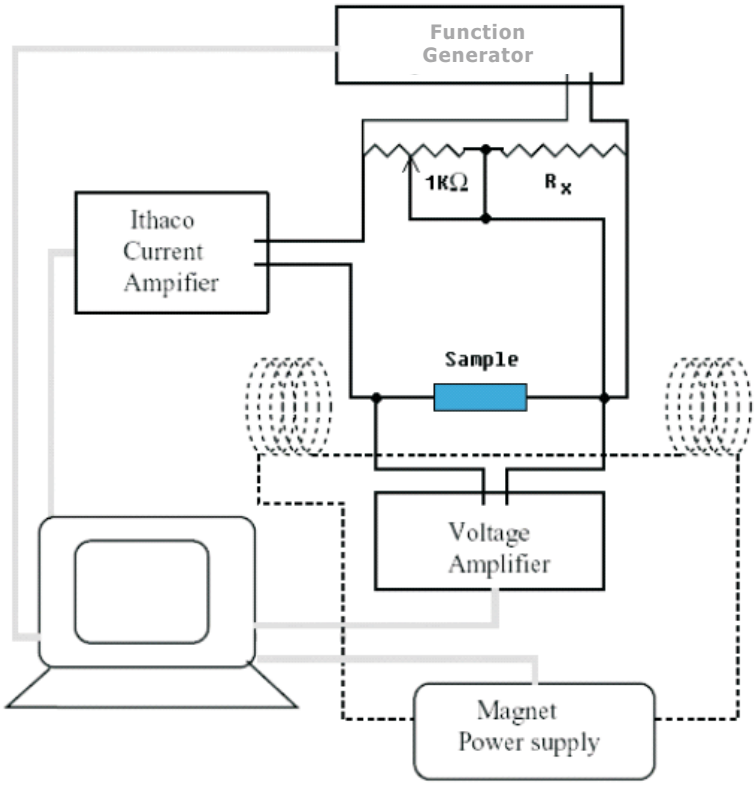

Figure 3.6: Schematic of electrical measurement circuit.

blockade with sharp features but without spin dependent TMR signal. Those samples are single particle devices. The absence of TMR for electron tunneling via grains shows that the spin-dephasing rate T_2 in these samples must be much larger than the tunneling rate at $4.2K$.

- Single-particle sample with TMR: This is the type of samples on which we are going to focus. The current flows through a single particle and is spin dependent. We cool down these samples to study the spin-polarized tunneling through discrete energy levels at $\sim 0.035mK$.

It is still not understood why some samples exhibit or do not exhibit TMR.

We also test the $I-V$ curves and TMR for about 10 tunneling junctions without the embedded grains and with similar resistance (empty junctions) at $4.2K$. Each of the empty junctions exhibits a linear $I-V$ curve and a significant TMR.

3.2.3 Measurements at Base Temperature

We use a He^3/He^4 dilution refrigerator to cool down our samples to base temperature ($\sim 0.035K$). Please read [93] for detailed operational mechanism of a He^3/He^4 dilution refrigerator.

There are 10 leads available for base temperature measurement. The sample leads are cryogenically filtered to reduce the electron temperature down to $\sim 0.1K$. We load 4 preselected samples with 2 leads connected to each sample. Each lead has a resistance of $4.2k\Omega$, which is much smaller than sample's resistance ($\sim G\Omega$). This is why we can do two probes measurement for our sample.

Preselected samples were placed in a weakly conductive container to protect samples from electrostatic shock. As we mentioned earlier, we ground ourselves and the cryogenic insertion during sample loading. Next, we use a turbo pump to pump the inner chamber, $1K$ pot, still, and condenser, then do the leak check for those parts. $1cm^3$ helium gas is filled into inner chamber as heat exchange gas at $4.2K$. Then we load the insertion into the main bath. The system is first cooled down to $77K$ by filling up the main bath with liquid nitrogen and allowing it to pre-cool overnight. Then we push out all the liquid nitrogen and fill it with liquid helium. The temperature reaches $4.2K$ quickly once helium exchange gas is adsorbed by a sorb. The temperature of the mixing chamber reaches $\sim 1.6K$ by pumping $1K$ pot properly. At this point, we can start the condensation and circulation of He^3/He^4 mixture and samples will be cooled down to base temperature ($35mK$). There is a superconducting magnet in the main chamber. The magnet must be completely immersed into liquid helium when running. In our dilution refrigerator, the magnetic field is perpendicular to the ground, the highest magnetic field is 12 $Tesla$ at $4.2K$, and is 14 $Tesla$ at $2.2K$. In order to run the magnet safely, liquid helium level $> 20\%$ is suggested.

The measurement setup in the dilution refrigerator is the same as that at $4.2K$. After cooling down the sample to the base temperature of the dilution refrigerator ($35mK$), four

types of measurements are mainly performed:

- $I-V$ curve at fixed magnetic field: $I-V$ curve is measured slowly to get very well resolved discrete energy levels. The bias voltage is limited within the first Coulomb staircase. The tunneling current increases in discrete steps as a function of bias voltage, corresponding to discrete electron-in-a-box energy levels of the grain. The tunneling rates from the leads to the grain can be calculated from the current steps.

- Vary the bias voltage very slow and magnetic field fast: Magnetic field is ramping between $-50mT$ and $50mT$ at a rate slow enough to show clear TMR without heating the sample, but fast enough to have at least 5 periods of field scans on each energy plateau.

- TMR at fixed bias voltage: Magnetic field is ramping between $-75mT$ and $75mT$ several times to check the reproducibility of TMR. The scan rate is slower than that of type 2 measurement, better resolved and more accurate TMR is obtained.

- Vary the magnetic field very slow and bias voltage fast: Magnetic field is swept from $12T$ to $-2T$ for more than 12 hours. The bias voltage is ramping between the threshold of the first discrete energy level and the threshold of the second Coulomb case. The scan rate of bias voltage should be slow enough to show clear resolved discrete energy levels without heating the sample, but fast enough to have at least 4 periods of bias scans for every Tesla. The energy levels exhibit Zeeman splitting as a function of an applied magnetic field. By analyzing Zeeman splitting, one can tell a lot about this tunneling device, such as, whether it's a single electron tunneling device, the number of electrons on the grain before tunneling in is even or odd, what the g-factor is and what the spin-orbit scattering rate is for a certain Al nanoparticle.

CHAPTER IV

EXPERIMENTAL RESULTS AND DISCUSSION

As we stated earlier, spin-polarized transport via metallic grains has recently generated significant theoretical interest [50, 54]. As spintronics goes nanometer scale, new phenomena are predicted resulting from the interplay between spin dependent electron transport and single electron physics [38, 33, 94, 95].

In this chapter we report on spin-polarized tunneling via single aluminum grains at low temperatures. Spin polarized electron transport permits studies of spin relaxation and spin dephasing [29, 23]. We find that some electron spin-relaxation times in Al grains are exceptionally long compared to bulk, on the order of μs [96].

4.1 Results at 4.2K and Discussion

We measured about 150 samples with the embedded grains at $4.2K$, the majority of samples ($> 80\%$) exhibit Coulomb blockade. We also tested about 10 tunneling junctions without the embedded grains and with similar resistance (empty junctions) at 4.2 K.

4.1.1 I-V Characteristic at 4.2K

Temperature dependence of $I-V$ curve for a single electron tunneling sample is shown in Figure 4.1. $I-V$ curves were measured in the temperature range from $4.2K$ to $293K$. Overall, sample resistance decreases with increasing temperature, which is typical for a tunneling junction [82]. At $4.2K$, sharp Coulomb blockade and Coulomb staircase are clearly observed. Coulomb blockade and Coulomb staircase are still visible but become

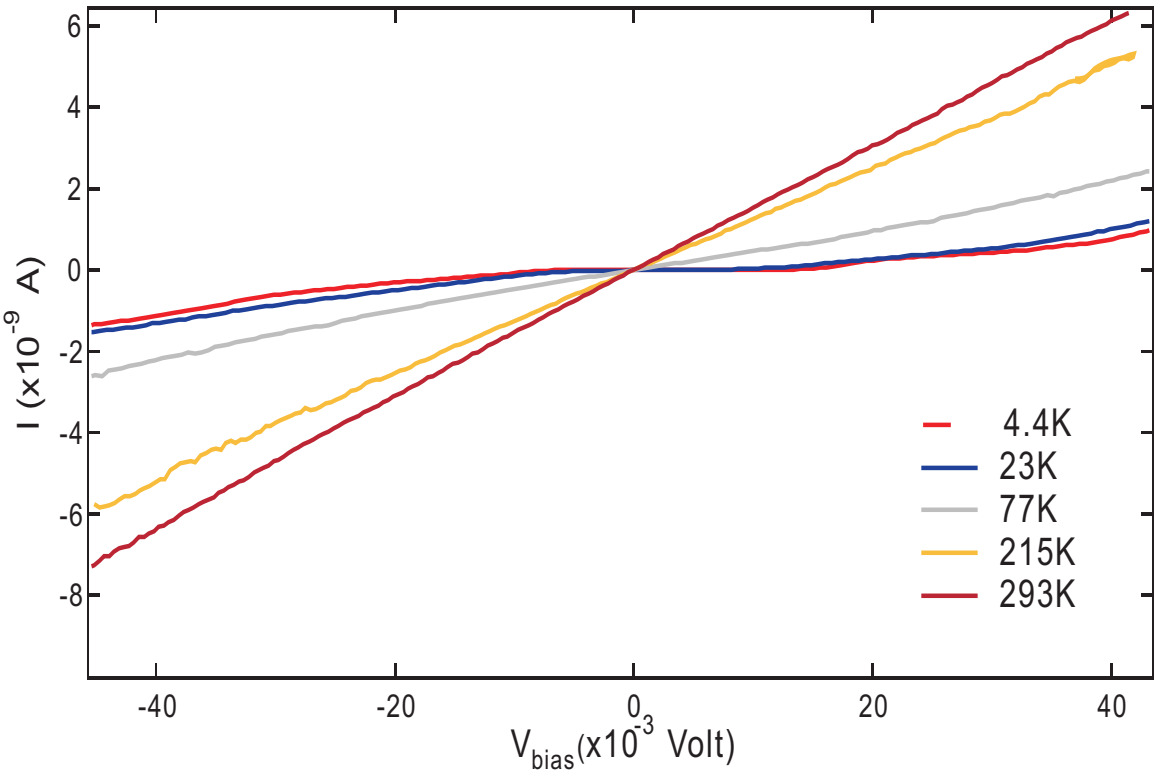

Figure 4.1: Temperature dependence of $I-V$ curve for a single electron tunneling sample. Sample resistance decreases with increasing temperature. Coulomb blockade appears at low temperatures, and disappears above 200K.

rounded when temperature rises from $4.2K$ to $77K$. This is due to thermal broadening of the Fermi distribution in the leads [92]. As temperature increased further ($215K - 293K$), single electron effects disappear and $I-V$ curve are linear. The full-width at half-maximum of the derivative of the Fermi distribution in the leads is about $3.5k_BT$ [92], the maximum temperature at which the Coulomb blockade is observable is $T_{max} \approx 0.57E_C/k_B$. The charging energy is about $14meV$, corresponding to $T_{max} \sim 160K$ for this sample, in good agreement with data.

The $I-V$ curve depends on the fractional residue charge Q_0 on the island and other parameters of the junctions, $C_{1,2}$ and $R_{1,2}$, four cases were illustrated in ref [64] when $-e/2 \leq Q_0 \leq e/2$. By following ref [64], one can obtain Q_0, $C_{1,2}$ and $R_{1,2}$ from $I-V$ curve.

We take the derivative of $I-V$ curve at $4.2K$, the $dI/dV-V$ curve is shown in Figure 4.2. Some junction parameters can be determined from the $dI/dV-V$ curve. The voltage spacing between steps of the Coulomb staircase is the distance between peaks in $dI/dV-V$

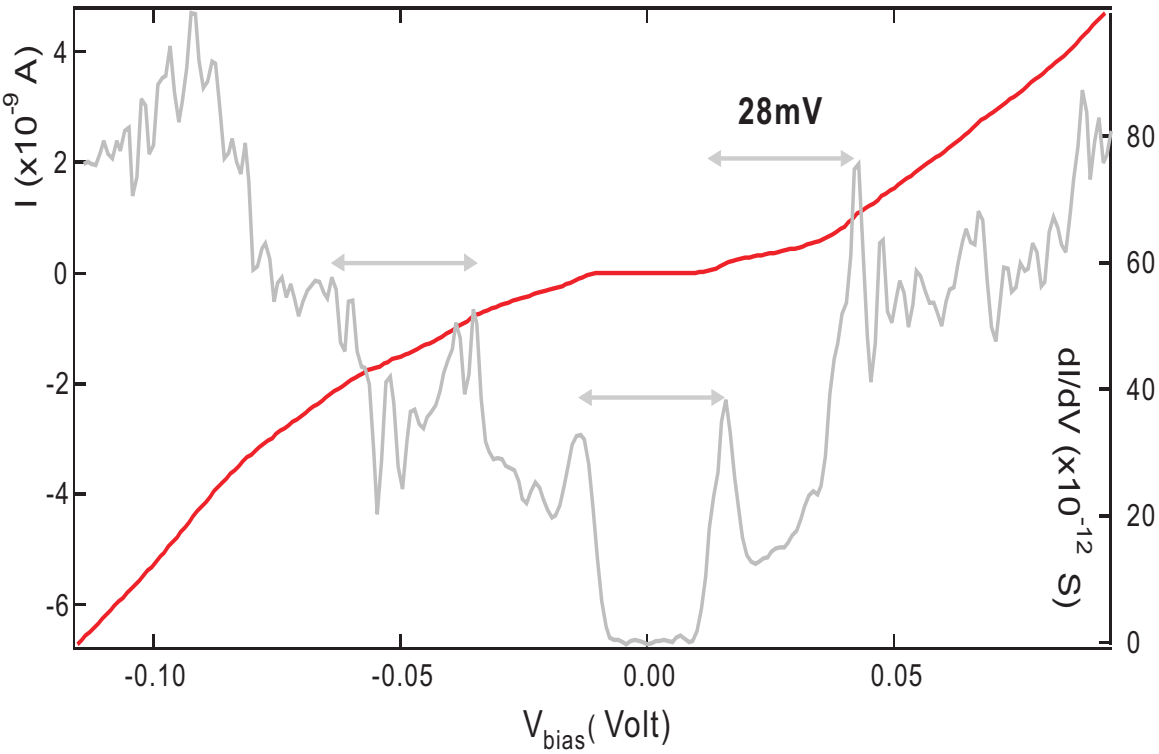

Figure 4.2: Conductance vs. bias voltage (grey curve) and current vs. bias voltage (red curve) for a device. The data shown here was acquired at 4.2K. We clearly see the periodicity of the Coulomb charging energy in the plot of conductance.

curve. In this particular case (Q_0 close to zero), one of the capacitances of two tunneling junctions can be determined from the $dI/dV - V$ curve as the following (it's applicable only in certain range of Q_0 and the ratio of C_1/C_2, and inapplicable to most of our samples):

$$C_{R>} = \frac{e}{V_{1^{st}pos.peak} - V_{1^{st}neg.peak}} \tag{4.1}$$

where $C_{R>}$ is the capacitance of the higher resistance junction, $V_{1_{st}pos.peak}$ and $V_{1_{st}neg.peak}$ are the positions of the first positive and negative peaks respectively.

From Figure 4.2, we have $V_{1^{st}pos.peak} - V_{1^{st}neg.peak} \approx 29.36meV \Rightarrow C_{R>} \approx 5.46aF$. Once we find $C_{R>}$, the fractional residue charge Q_0 can be determined by,

$$Q_0 = \frac{C_{R>} \times (V_{1^{st}pos.peak} + V_{1^{st}neg.peak})}{2} \tag{4.2}$$

The fractional residue charge $Q_0 \approx 0.066e$ is then determined.

$C_{R>}$ and fractional residue charge Q_0 are the only two junction parameters can be accurately determined for this $I - V$ curve. The rest of the parameters can be obtained by fitting $I - V$ curve to the orthodox theory of single electron tunneling [64, 65].

So far, we have evaluated the $I - V$ curve of a potential working sample. There are some samples which have $I - V$ curve as shown in Figure 4.3. The $I - V$ curve is nonlinear, but the $I - V$ curve is rounded at Coulomb blockade threshold. Samples with certain $I - V$ curve have multiple particles contributing to the current flow [97]. Those particles carry current in parallel, each particle has its unique tunneling parameters. The randomness of tunneling junctions obscures the clear features of single electron tunneling samples.

We made tunneling junctions without the embedded aluminum grains (empty junctions). We deposit aluminum oxide at the thickness of a single tunneling junction. The sample resistance is similar to that of sample with particle, and the $I - V$ curve is linear (Figure 4.4). When we deposit aluminum oxide with the thickness as twice thick as that of a single tunneling junction, the sample resistance goes to infinity. So in the nanoparticle samples, the electrons must tunnel onto nanoparticle from one electrode, then tunnel off nanoparticle to the other electrode, demonstrating single electron tunneling behaviors in our samples are caused by aluminum grains.

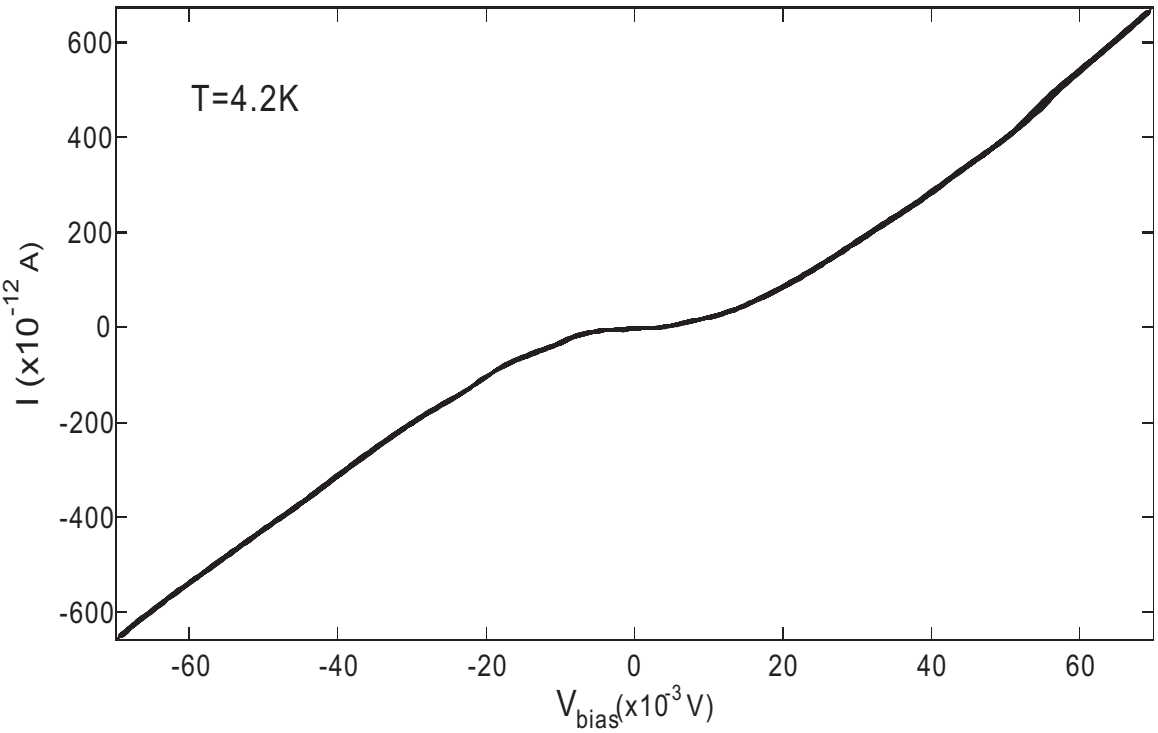

Figure 4.3: I-V curve of a multiparticles device measured at 4 K. The $I - V$ curve is rounded at Coulomb blockade threshold.

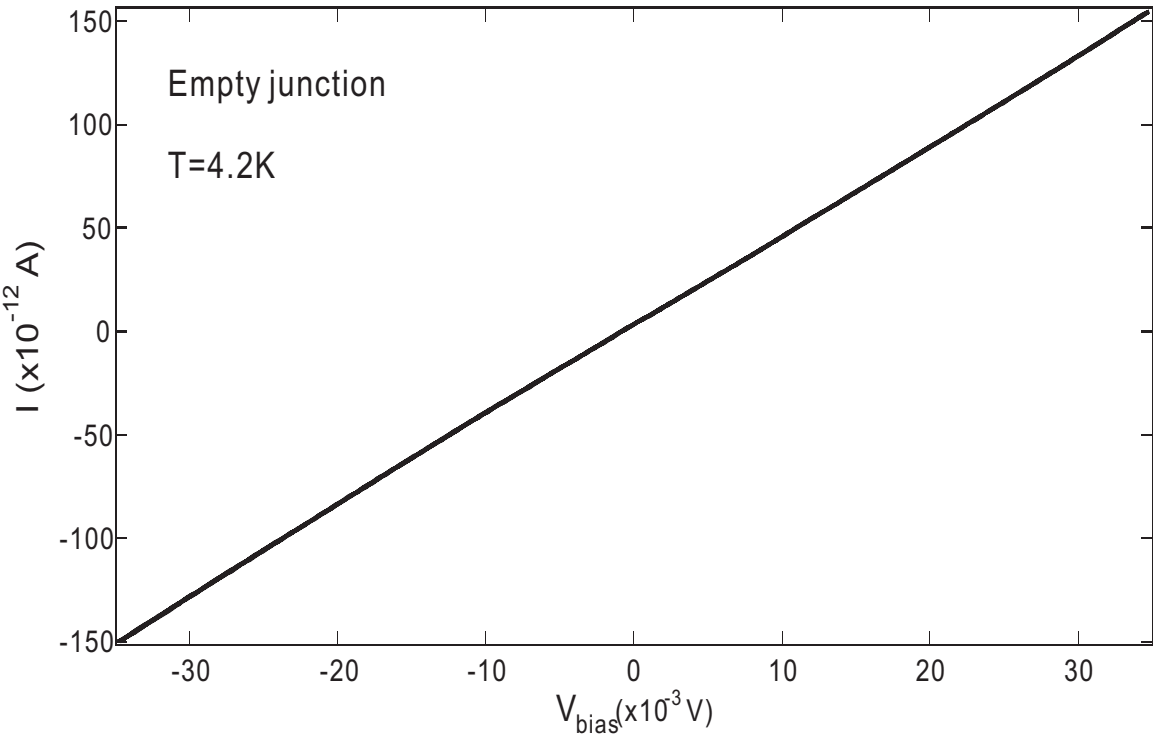

Figure 4.4: $I - V$ curve of an empty junction, which is linear.

4.1.2 TMR at 4.2K

Now we discuss spin-polarized tunneling at $4.2K$. In the magnetic field range of $\pm 50mT$, approximately 90% of the samples do not display any of TMR effect. By contrast, we tested about 10 tunneling junctions without the embedded grains and with similar resistance (empty junctions) at $4.2K$. All of the empty junctions exhibit a significant TMR in this field range, comparable to 10%. Approximately one half of the empty junctions display a simple spin-valve effect. So, the absence of TMR for electron tunneling via grains shows that the spin-dephasing T_2^{-1} in the grains must be typically much larger than the tunneling rate.

Nevertheless, approximately 10% of the samples with embedded grains display significant TMR, so in these samples T_2^{-1} must be smaller than or comparable to the tunneling rate in these samples. T_2 variation among different samples could be explained by magnetic defects, such as paramagnetic impurities from the Py layer. Paramagnetic impurities are common sources of dephasing [98], assuming that the relaxation rate of impurity is higher than tunneling rate. The defects would be located on the grain surface, since bulk Al does not support paramagnetism. Since the number of atoms on the surface is relatively small (~ 1000), we could occasionally obtain a sample free of impurities. More insight into the nature of T_2 in this device will require a more in depth theoretical study.

A majority of the samples with nonzero TMR show positive TMR (Figure 4.5); only about 30% of the samples show negative TMR (Figure 4.6). As we discussed in 2.3.2, the sign of TMR in quantum dots is determined by the interplay between charging effects and spin accumulation [34, 38, 55]. The negative TMR was also observed in Au nanoparticle in an $FM/I/Au/I/FM$ structure [42]; the negative TMR can not be explained in the framework of the *Julliére* model, and is attributed to the spin accumulation in Au nanoparticle.

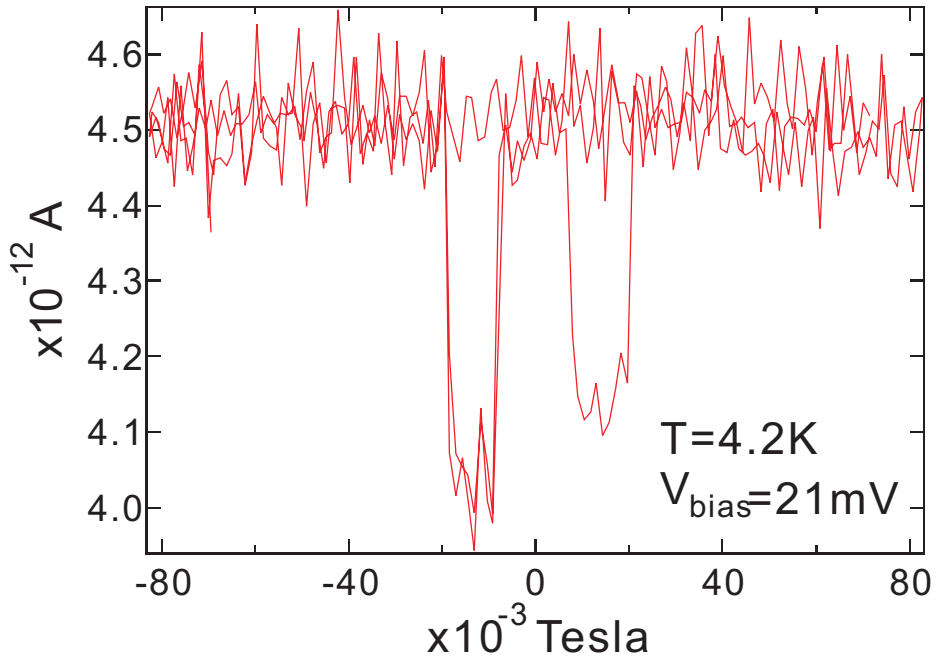

Figure 4.5: An example of typical positive TMR measured with positive bias at 4.2K. The current is higher when magnetization of two FM layer are parallel.

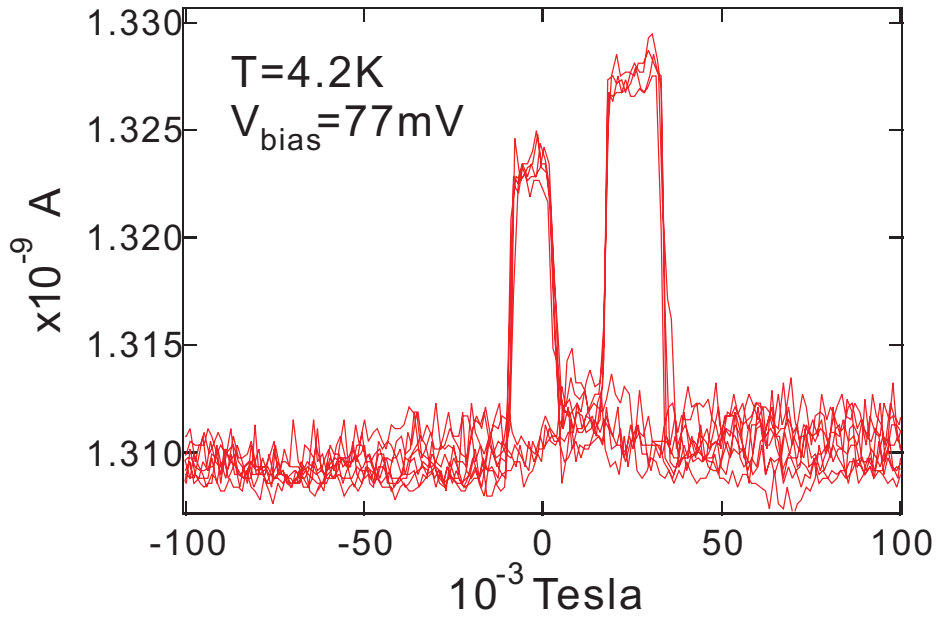

Figure 4.6: An example of negative TMR measured with positive bias at 4.2K. The current is lower when magnetization of two FM layer are parallel.

TMR in our devices usually does not display a simple spin-valve effect. We believe this is because there are spin-dependent interactions inside the grain that induce a complicated TMR even when the magnetic transitions in the drain and source leads are sharp and as expected. For example, a rotation of stray magnetic field acting on the grain will alter the direction of the spin-quantization axis in the grain, thereby changing the conductance [23]. A rotation or a switch of a remote domain can change the tunneling current through the grain via the magnetic field generated by the domain. Similarly, the orientation of the nuclear spin in the grain can change the quantization axes via the hyperfine interaction.

The resistance of our samples is much larger than resistance quantum ($25.8k\Omega$), co-tunneling is strongly suppressed and we do not study TMR effect in co-tunneling regime.

TMR is calculated by equation 2.19. TMR of empty junctions is about 10%, which is close to the highest TMR of $Py/I/Py$ single junction [90]. It proves that our empty junctions are of good quality. TMR of empty junctions is positive and is found to be symmetric and weakly dependent on voltage (Figure 4.7), in good agreement with the *Julliére* model.

TMR of our devices with embedded grains are less than 10%. It is unlikely that the suppression of TMR is caused by junction quality, since our empty junctions are of good quality. We suggested that the suppression of TMR is due to spin relaxation within the Al nanoparticle.

4.2 Results at Base Temperature and Discussion

Electron tunneling through single nanometer scale metallic grains at low temperatures can display a discrete energy level spectrum [46]. Spin-polarized tunneling via discrete energy levels of single aluminum grains permits studies of spin relaxation and spin dephasing [29, 23]. There were 16 samples measured at $35mK$. We describe two samples in details.

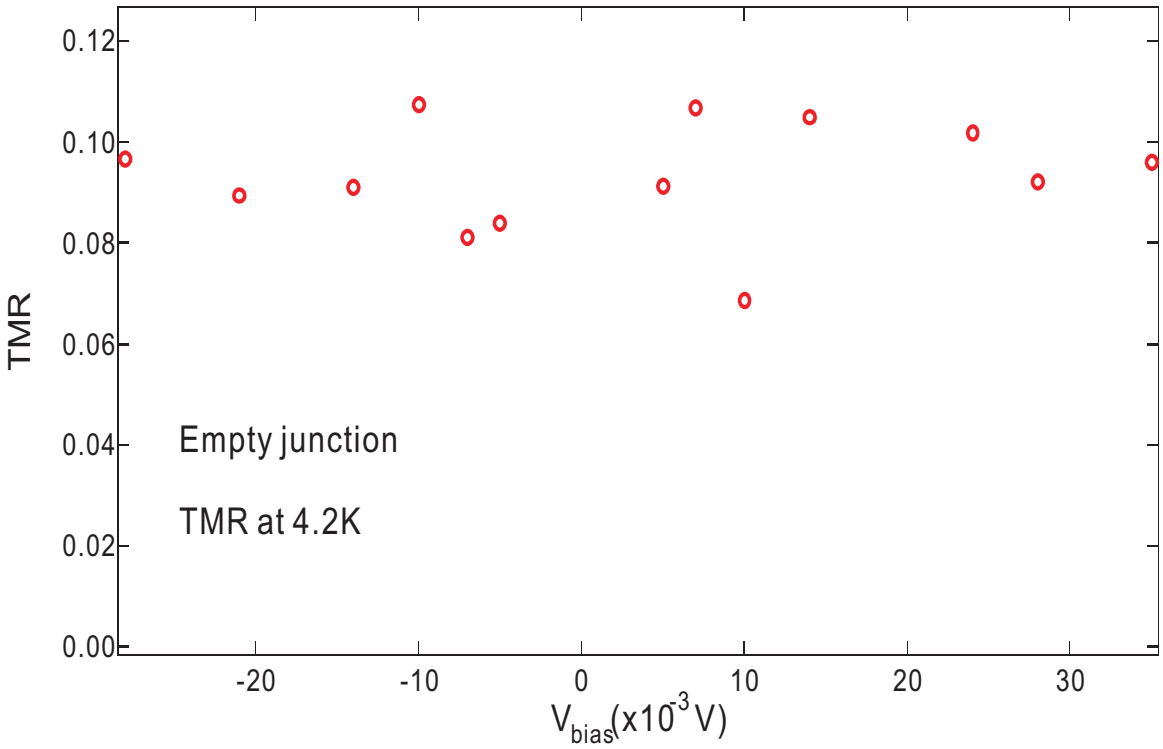

Figure 4.7: TMR of empty junctions is positive and is found to be symmetric and weakly dependent on voltage.

4.2.1 I-V Characteristic at 35mK

The I-V curve of two samples are shown in Figure 4.8. The tunneling current increases in discrete steps as a function of bias voltage, corresponding to discrete electron-in-a-box energy levels of the grain. The discrete energy levels are displayed more clear when we zoom in the negative bias of sample 1 (Figure 4.9). The conductance of sample 1 is also shown in Figure 4.9.

In sample 1, the average electron-in-a-box level spacing caused by electron geometric confinement is $\delta \approx 0.8meV$. Assuming a spherical shape, the diameter of Al grain in this sample is estimated to be $D \approx 6nm$ from equation (2.16). The average current step is $\overline{I} \approx 0.47pA$, We make a connection with the tunneling rates from the leads to the grain and the measured current response. The tunnel junctions are highly asymmetric, and therefore one of the tunneling rates is much smaller than the other, and thus rate limiting. Throughout this paper, we choose the rate limiting step to be across the left junction,

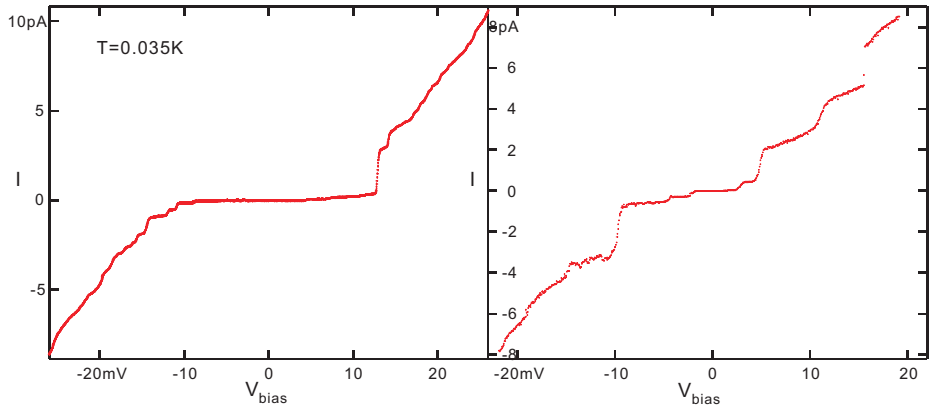

Figure 4.8: I-V curves at the base temperature. The tunneling current increases in discrete steps as a function of bias voltage, corresponding to discrete electron-in-a-box energy levels of the grain.

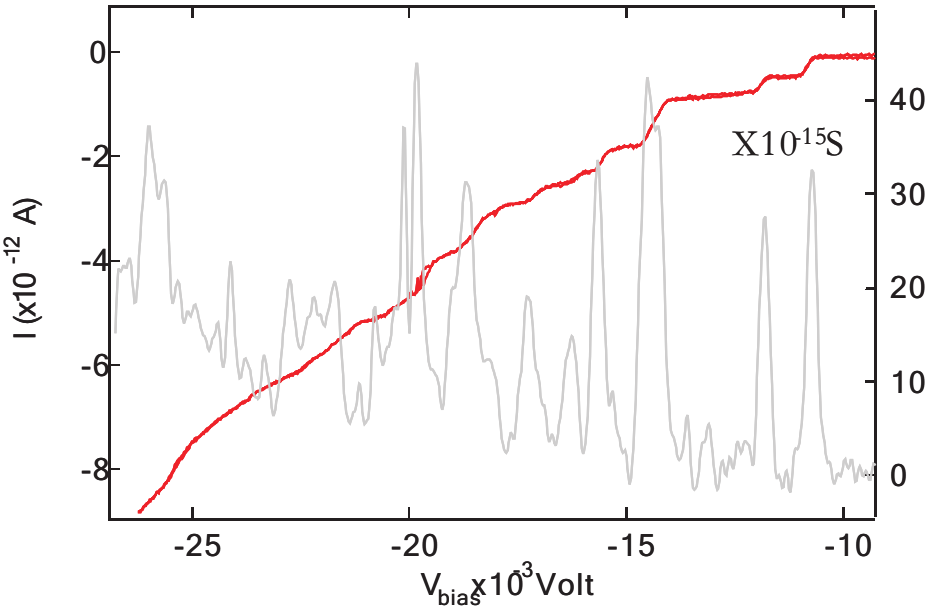

Figure 4.9: Conductance and I-V curves at the base temperature. Discrete energy levels are clearly observed. There are many conductance peaks, each of which relates to an energy level.

corresponding to the tunneling rate which corresponds to the average tunneling-in rate of $\overline{\Gamma}_L = \overline{I}/2|e| \approx 1.5 \cdot 10^6 s^{-1}$; the tunneling-out rates are much larger. Similarly, in sample 2, $\delta \approx 2.7meV$, $D \approx 4nm$, and $\overline{\Gamma}_R \approx 9.6 \cdot 10^6 s^{-1}$. The grain sizes of sample 1 and sample 2 are in agreement with $5nm$ average diameter obtained from SEM image.

The spin-conserving energy-relaxation in Al grains takes place by phonon emission with the relaxation rate [28]

$$\frac{1}{\tau_{e-ph}(\omega)} = \left(\frac{2}{3}E_F\right)^2 \frac{\omega^3 \tau_e \delta}{2\rho\hbar^5 v_S^5}, \tag{4.3}$$

where $E_F = 11.7eV$ is the Fermi energy, ω is the energy difference between the initial and the final state, $\rho = 2.7g/cm^3$ is the ion-mass density, and $v_s = 6420m/s$ is the sound velocity. We obtain $\tau_{e-ph}^{-1}(\delta) \approx 1.6 \cdot 10^9 s^{-1}$ and $4.1 \cdot 10^{10} s^{-1}$ in samples 1 and 2, respectively. Sample 2 has significantly larger relaxation rate because of the larger level spacing.

Since the tunneling rates in our samples are $\sim 10^6 s^{-1}$ if the grain is excited by electron tunneling in and out, it will instantly relax to the lowest energy state accessible by spin-conserving transitions.

The number of electron levels is determined by the following equation,

$$N = \frac{V_{bias} - V_{CBL}}{\delta \times \frac{C_R}{C_R + C_L}} \tag{4.4}$$

Where V_{CBL} is Coulomb blockade threshold voltage at negative bias, C_L and C_R are junction capacitances for left and right leads respectively, δ is the average energy level spacing. The number of electron levels can be obtained by the similar procedure at positive bias. This formula assumes that the level spacing is roughly constant, and that the tunnel junctions have well defined capacitances.

4.2.2 Zeeman effect and Spin-Orbit Interaction

Magnetic field is swept slowly from $12T$ to $-2T$ for more than 14 hours. The bias voltage is ramping faster between the threshold of the first discrete energy level and the

threshold of the second Coulomb staircase. Current and conductance versus bias voltage and the applied magnetic field are shown in Figure 4.10 and Figure 4.11 respectively, the energy levels exhibit Zeeman splitting as a function of an applied magnetic field. For purely spin-up and spin-down eigenstates, the applied magnetic field causes spin-up and spin-down eigenstates to shift linearly in opposite directions. The higher the applied field, the larger the splitting. The slope of this linear dependence is $\pm g\mu_B/2$, where g is electron g-factor (= 2 for free electron), and μ_B is the Bohr magneton. The g-factor can be reduced by scattering processes.

In sample 1, the $I-V$ curve probes the same energy spectrum at negative and positive bias voltage. This is evident from the equivalence of the magnetic field dependencies at negative and positive bias. The lowest tunneling threshold is two fold degenerate at zero magnetic field, showing that N_0, the number of electrons on the grain before tunneling in, is even. This can be explained by a simple model [92]. For an even N_0, the chemical potential μ ia right above the highest full-filled energy level, an electron can occupy both spin-up and spin-down states of each unoccupied energy level, Zeeman splitting will be observed. For an odd N_0, μ locates right at the energy of the half-filled highest occupied energy level, the lowest energy level will not show Zeeman splitting, since the lower-half of the lowest energy level has been occupied.

In sample 1, the current steps are similar in magnitude at negative bias, because the first tunneling step, in which an electron tunnels in to the grain through the higher resistance junction, is rate limiting. At positive bias, the first current step is much larger than the subsequent current steps, because the first tunneling step takes place via the lower resistance junction, and the rates are limited by the electron discharge process across the high resistance junction.

In sample 1, the first two current steps split corresponding to g-factors: $g = 1.83 \pm 0.05$ and 1.95 ± 0.05. Slight reduction of the g-factors from 2 indicates spin-orbit interaction in Al [46]. The avoided level crossings clearly are resolved in Figure 4.10, 4.11. In the regime where g factors are slightly reduced, the spin-orbit scattering rate (τ_{SO}^{-1}) can be obtained from the avoided crossing energies $\Delta_{SO} \approx 0.1meV$ [61]. Theory predicts that

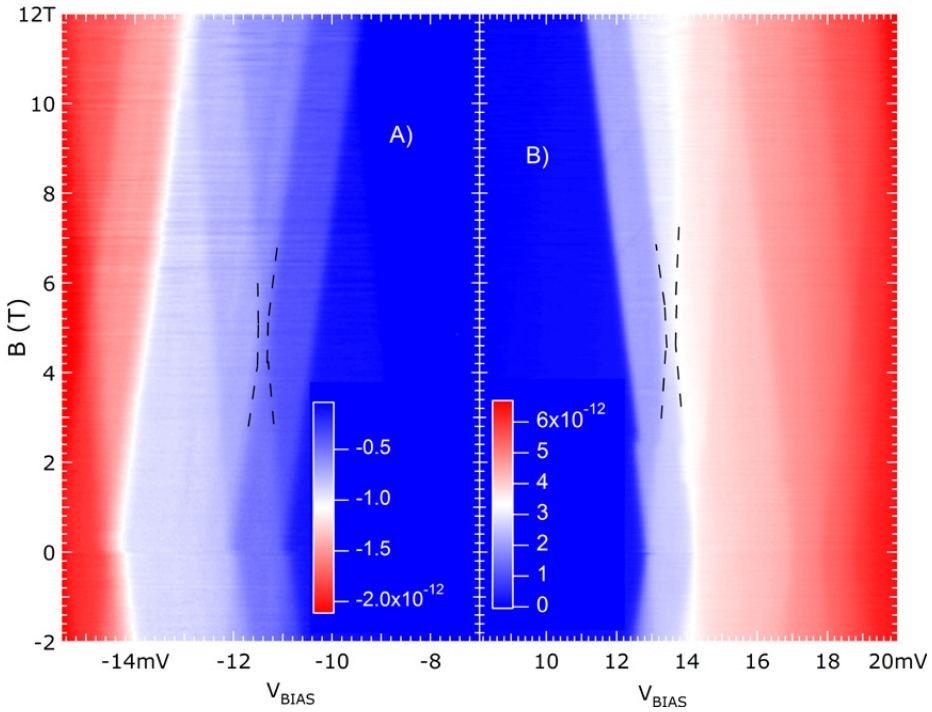

Figure 4.10: A, B: Current (color) versus bias voltage and the applied magnetic field in sample 1 at the base temperature.

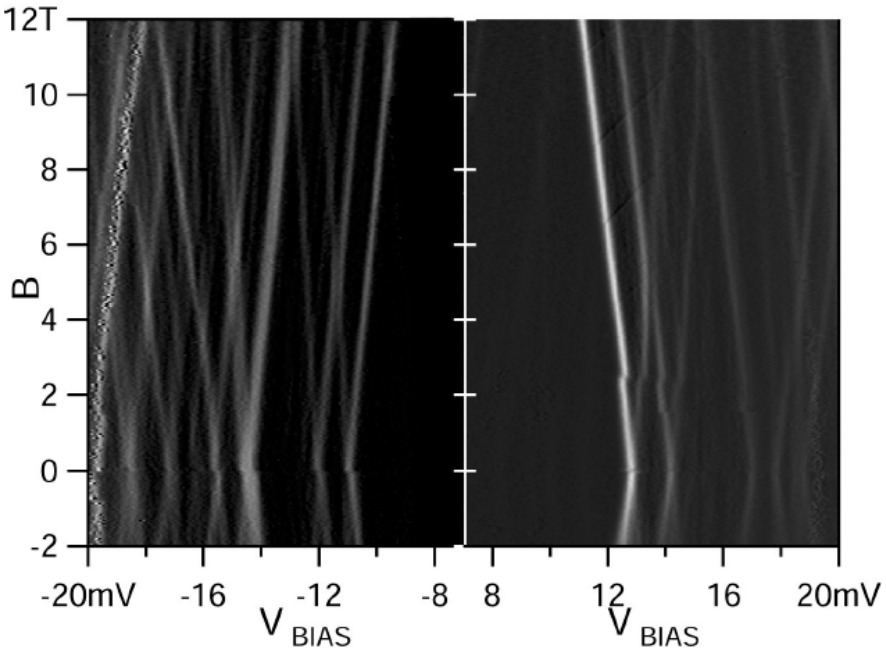

Figure 4.11: Differential conductance (gray) versus bias voltage and the applied magnetic field in sample 1 at the base temperature.

$\tau_{SO} \approx \hbar\delta/\pi\Delta_{SO}^2$ [61], within a factor of two. Thus, we obtain $\tau_{SO}^{-1} \approx 5.5 \cdot 10^{10} s^{-1}$. By the $Elliot - Yafet$ relation [19], τ_{SO}^{-1} is related to the elastic scattering rate τ_e^{-1}: $\tau_{SO}^{-1} = \alpha\tau_e^{-1}$. Assuming ballistic grain, $\tau_e^{-1} \approx v_F/D = 3.4 \cdot 10^{14} sec^{-1}$. We obtain $\alpha \approx 1.6 \cdot 10^{-4}$, in excellent agreement with $\alpha \approx 10^{-4}$ in Al thin films [56].

This current versus bias voltage and the applied magnetic field figure gives strong support that we are measuring the electron tunneling through a single particle. First, Figure 4.10, 4.11 demonstrates the equivalence of the magnetic field dependencies at positive and negative bias, indicating that the $I-V$ curve probes the same energy spectrum at negative and positive bias voltage. This argument is based on the fact that, due to differing tunnel junction widths and background charge, the electron would preferentially tunnel onto different particles in a multi-particle system depending on whether the bias is positive or negative. Second, comparing the related first five plateaus at positive and negative bias at zero field, we have $V_{Ri}/V_{Li} = 1.6 \pm 0.02$, for $i = 1, 2, 3, 4, 5$. Therefore, the fractional residual charge Q_0 and capacitance ratio C_R/C_L must be the same for all five peaks [64]. Next, the slopes of the splitting of the current thresholds with field also depend on the capacitance ratio. All thresholds at one side of the bias voltage split with same slope; all thresholds on the right hand side split with the same slope as well; the slopes at the negative and positive bias are different, in agreement with the capacitance ratio. Finally, energy levels of different particles would not exhibit avoided level crossings, contrary to the data.

4.2.3 TMR and Spin Relaxation

A majority of the samples with nonzero TMR show positive TMR near the Coulomb-Blockade conduction threshold; only about 30% of the samples show negative TMR. The sign of TMR in quantum dots is determined by the interplay between charging effects and spin accumulation [33, 55]. For any given sample, the data in this part correspond to the voltage range within the first step of the Coulomb staircase, where $sgn(TMR) = const.$.

We select only those samples that display a simple spin-valve TMR effect, which is shown

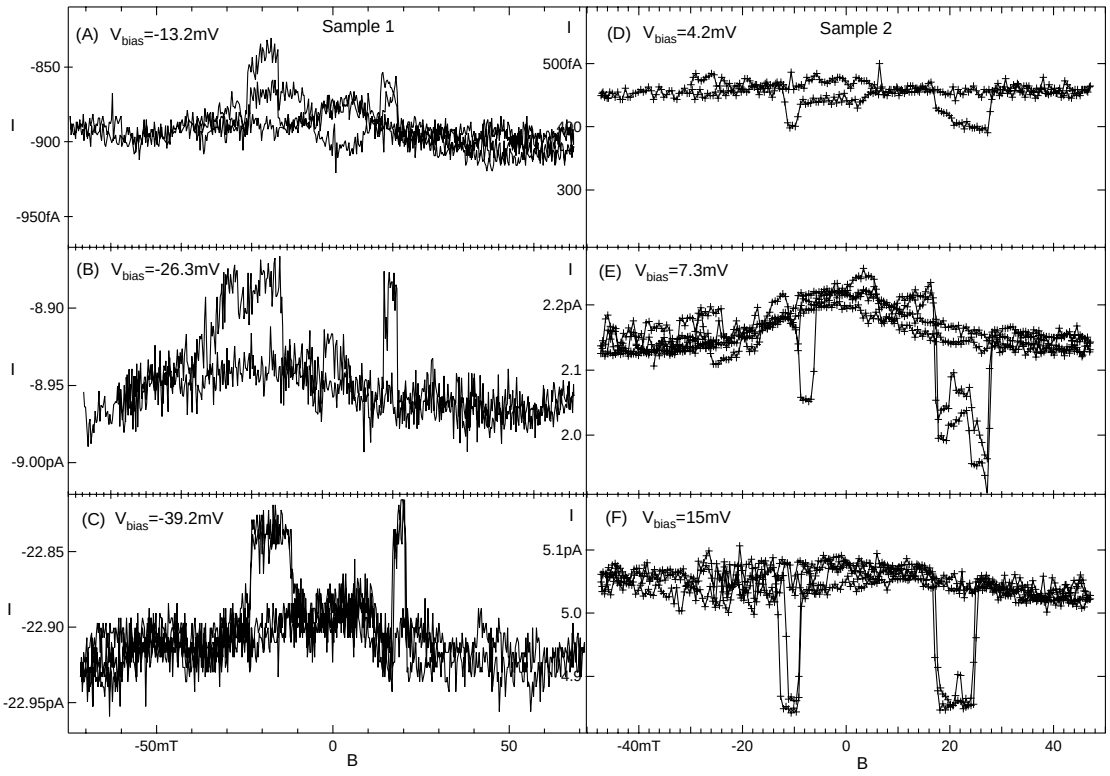

Figure 4.12: A-F: Spin-valve effect in current versus applied magnetic field in two samples at the base temperature. The current magnitude is reduced in the antiparallel state.

in Figure 4.12. Figure 4.12-A is the TMR of sample 1 at a bias voltage corresponding to the second current plateau. TMR is barely resolved in this case, since the current changes by only about $40fA$. We do not have good data to display TMR at the first current plateau. By comparison, Figure 4.12-B and C display TMR at bias voltage where the number of electron-in-a-box levels, calculated from equation 4.4, energetically available for tunneling-in are approximately 19 and 48, respectively. To facilitate comparisons, the current intervals on the vertical axes in Figure 4.12 A-C and D-F have equal lengths.

The switching events in our samples is quite reproducible with repeated field scans, but they are history dependent and do vary a little between repeated scans. The history dependence can be explained by the hysteresis in the leads. The tunneling junction is of nanometer size, much smaller than the domain size, so tunneling takes place from a single domain. This domain will switch direction depending on the stray fields from neighboring domains, which is history dependent. Similarly, small shifts of the switching field with

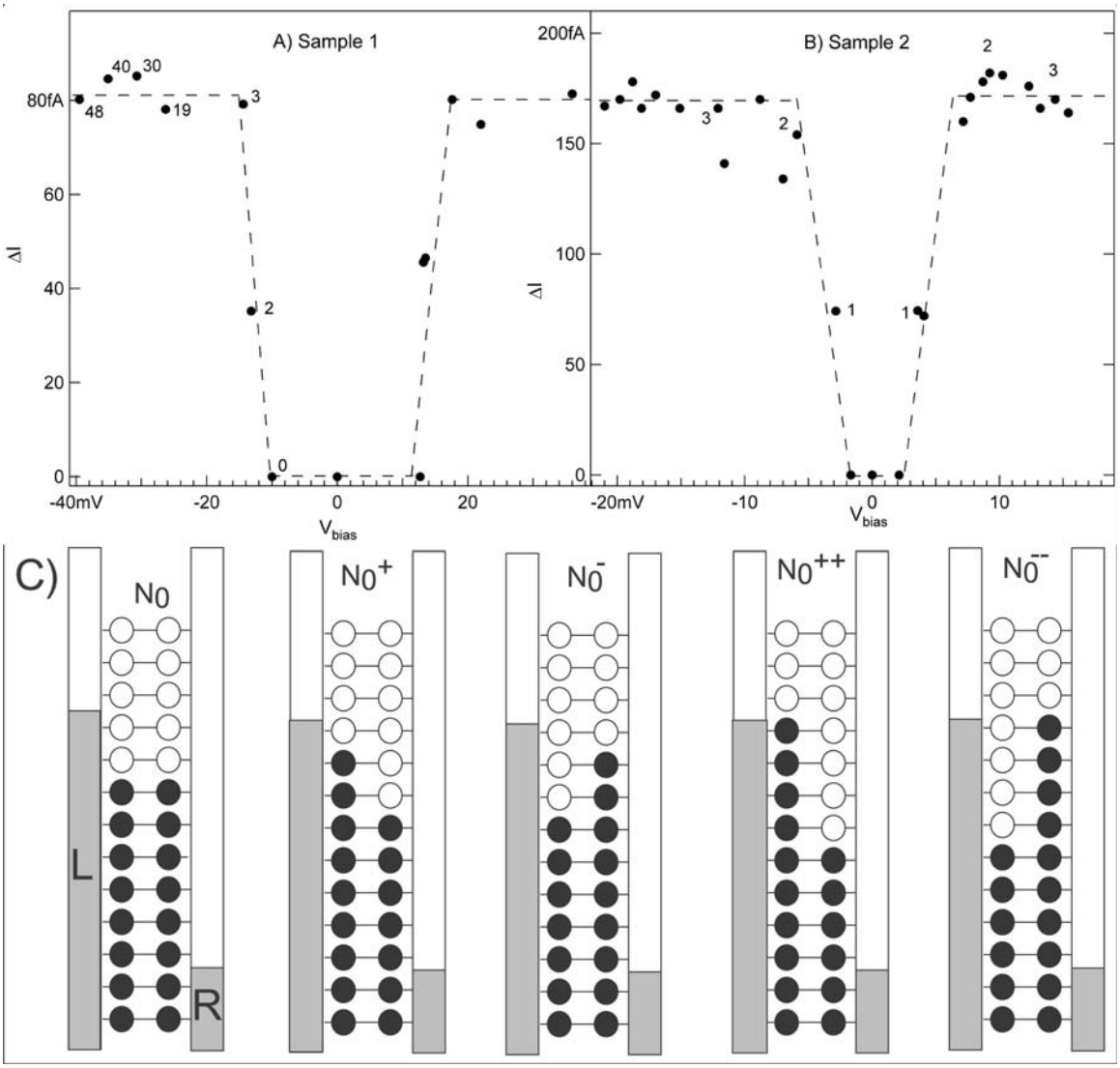

Figure 4.13: A and B: $\Delta I = |I_{\uparrow\uparrow} - I_{\uparrow\downarrow}|$ versus bias voltage in samples 1 and 2, respectively, at the base temperature. The numbers near the circles indicate how many doubly degenerate electron-in-a-box levels are available for tunnelling in. C: Possible spin-polarized electron configurations caused by electron tunnelling in and out, before an electron tunnels in, at the second current plateau, for N_0 even.

repeated cycles can be explained by the fact that the magnetic domain configuration of Py film does not exactly follow the same microscopic state with repeating cycles, which is a hysteresis intrinsic to ferromagnets. The fluctuations of the switching fields are weak.

A common artifact in Coulomb blockade samples containing magnetic components is that the electrochemical potential difference between the island and leads can jump when the moment in one of the magnetic components changes direction [52]. This can cause a sudden shift in energy levels, producing a jump in current. This threshold voltage shift is clearly shown as a discontinuity near zero magnetic field in Figure 4.11, and is $\sim 0.1meV$. We also performed other measurements by sweeping the magnetic field both on and between the current plateaus, coming up with similar values for the electrochemical shift. This is lower than the average level spacing of $0.8meV$ and $2.7meV$ for sample 1 and sample 2 respectively. To rule out the artifact mentioned above, we carefully measured TMR in the middle of the current plateau, the threshold voltage shift should not effect our measurements.

The key observation in this report is that $\Delta I = \mid I_{\uparrow\uparrow} - I_{\uparrow\downarrow} \mid$ is nearly constant with current above a certain current. There is hardly any increase in ΔI between Figure 4.12 B and C and between Figure 4.12 E and F. This behavior is shown in more detail Figure 4.13-A and B, which displays ΔI versus bias voltage. ΔI versus negative bias voltage in sample 1 is fully saturated at the third current plateau; at the second current plateau, ΔI is already at one half of the saturation value. Similarly, in sample 2 ΔI reaches saturation at the second current plateau. Our samples should be contrasted with ordinary ferromagnetic tunneling junctions, where ΔI is proportional to the current over a significantly wider range of bias voltage [82, 83].

To explain $\mid I_{\uparrow\uparrow} - I_{\uparrow\downarrow} \mid = const$, we must discuss the relative magnitudes of three rates: τ_{e-ph}^{-1}, the rate of energy relaxation from excited to lower energy states by spin-conserving phonon emission; Γ_L, the rate electrons tunnel into the grain; and T_1^{-1}, the rate of transitions between levels that result in an electron flipping its spin orientation. τ_{e-ph}^{-1} is obtained theoretically, the measured $I-V$ spectrum fixes the tunneling rate Γ_L, and T_1^{-1} is obtained from the saturation in $\mid I_{\uparrow\uparrow} - I_{\uparrow\downarrow} \mid$ with bias voltage.

Finally we must deduce the relative magnitude of T_1^{-1}. The rate of spin-flip transitions is expected to be significantly smaller than τ_{e-ph}^{-1} [19]. In this case the ground state would not always be accessible by energy relaxation. The grain could remain in an excited, spin-polarized state, as sketched in Figure 4.13-C. These spin polarized excited states are responsible for spin accumulation in the antiparallel magnetic configuration of the leads. If the relaxation rates for the spin-flip transitions are much smaller than the tunneling rate, then various spin-polarized states would have similar probabilities, which are determined by the tunneling rates. In the antiparallel configuration of the leads, the probabilities of the excitations with spin up would be enhanced by $1 + P$ and probabilities of the excitations with spin down would be suppressed by $1 - P$, where P is the spin polarization in the leads. In the parallel configurations, the probabilities of the excitations with spin up and spin down are the same. In this regime, $\mid I_{\uparrow\uparrow} - I_{\uparrow\downarrow} \mid$ is proportional to the current, similar to the usual ferromagnetic tunneling junctions.

It is reasonable to expect that the spin-flip rate $T_1^{-1}(\omega)$ increases rapidly with energy difference ω between the initial and the final state (In bulk metals the spin-orbit scattering rate increases rapidly with electron excitation energy.). If $T_1^{-1}(\omega)$ exceeds the tunneling rate above some ω, then the excitations with energy $> \omega$ will occur with a reduced probability in the ensemble of states generated by tunneling in and out. Thus ΔI is limited by tunneling via the ground state and those low lying spin-polarized states where $T_1^{-1}(\omega) < \Gamma_L$. ΔI versus bias voltage approaches saturation approximately when $T_1^{-1}(\omega) = \Gamma_L$, where ω is the highest excitation energy in the ensemble of spin-polarized states generated by tunneling in and out: $\omega \approx \delta \frac{I}{|e|\Gamma_L}$. This is how we can determine the spin-relaxation time $T_1(\omega)$ at one energy ω in a given sample.

In sample 1, ΔI is at 50% of the saturation value at the second current plateau, and ΔI is saturated at the third current plateau. At the second current plateau, the spin relaxation rate of the highest energy excited state generated by tunneling must be close to the tunneling rate. Since the spin relaxation is very rapid in configurations more than 3δ above the ground state, and N_0 is even as noted above, the grain spends most of the time among the five configurations shown in Figure 4.13-C: N_0, N_0^+, N_0^-, N_0^{++}, and N_0^{--}. The

highest energy spin-polarized states are N_0^{++} and N_0^{--}. Thus, $T_1^{-1}(3\delta) \approx \Gamma_L = 1.5 \cdot 10^6 s^{-1}$. In sample 2, this analysis leads to $T_1^{-1}(2\delta) \approx 10^7 s^{-1}$.

Now we discuss the origin of spin relaxation and its rapid enhancement with the energy difference. Note that the rate of spin-conserving transitions in equation 4.3 increases as ω^3. We suggest that the electron-phonon transition rates without and with spin flip scale by the $Elliot - Yafet$ relation: $T_1^{-1}(\omega) = \alpha' \tau_{e-ph}^{-1}(\omega)$. This scaling would explain the increase in spin-relaxation rate with excitation energy. In metallic films, it is well established that the $Elliot - Yafet$ scaling applies for both elastic and inelastic scattering processes, with $\alpha \approx \alpha'$ [56].

In sample 1, equation 4.3 leads to $\tau_{e-ph}^{-1}(3\delta) \approx 4 \cdot 10^{10} s^{-1}$. Since $T_1^{-1}(3\delta) \approx 1.5 \cdot 10^6 s^{-1}$, we obtain $\alpha' \approx 0.4 \cdot 10^{-4}$. Similarly, in sample 2, $\tau_{e-ph}^{-1}(2\delta) \approx 3.3 \cdot 10^{11} s^{-1}$ and we obtain $\alpha' \approx 0.3 \cdot 10^{-4}$. α' agrees with $\alpha \approx 1.5 \cdot 10^{-4}$ obtained earlier, within an order of magnitude. So the ratio of τ_{e-ph} and T_1 is in agreement with the $Elliot - Yafet$ scaling. This is an evidence that the spin-flip transitions in Al grains are driven by the spin-orbit interaction. By this relaxation mechanism, the spin of an electron on the grain is coupled to the phonon continuum via the spin-orbit interaction. An electron in an excited spin-polarized state relaxes by an emission of a phonon, which has an angular momentum equal to the difference between the initial and final electron spin.

CHAPTER V

CONCLUSIONS

Single Aluminum nanoparticle double tunneling junctions devices were fabricated by using a state of the art e-beam lithography and shadow evaporation technique. The size of Aluminum nanoparticle is about $5nm$. The energy levels of such a small Aluminum nanoparticle are quantized at very low temperatur (30mK).

We have observed spin-coherent transport via discrete energy levels of single Al grains. In high resistance samples ($\sim G\Omega$), spin polarized current saturates quickly as a function of bias voltage, which demonstrates that spin-polarized current is carried only via the ground state and the low-lying excited states. Higher excited states have a relaxation time shorter than the tunneling time and they do not carry spin-polarized current. In two samples, the spin-relaxation rate T_1^{-1} for some of the low-lying excited states is comparable to the electron tunneling rate: $T_1^{-1} \approx 1.5 \cdot 10^6 s^{-1}$ and $10^7 s^{-1}$.

The ratio of the spin-flip transition rate (T_1^{-1}) and the electron-phonon relaxation rate is in quantitative agreement with the $Elliot - Yaffet$ scaling ratio, an evidence that the spin-relaxation transitions are driven by the spin-orbit interaction.

A majority of the samples with nonzero TMR show positive TMR near the Coulomb-Blockade conduction threshold; only about 30% of the samples show negative TMR. The sign of TMR in quantum dots is determined by the interplay between charging effects and spin-accumulation.

CHAPTER VI

MESOSCOPIC ELECTRON TRANSPORT IN COBALT NANO FERROMAGNETS: MOTIVATION AND THEORETICAL OVERVIEW

In micron scale metallic samples at low temperatures, interference among scattered electron waves creates noticeable contributions to sample resistance, including random but reproducible fluctuations in conductance (CF) [43, 44, 45]. One remarkable consequence is that the resistance of phase-coherent samples becomes sensitive to microscopic impurity configurations. In this work we investigate the resistance of mesoscopic ferromagnets at low temperatures and find a similar result that the resistance is very sensitive to the magnetic state of the sample. In particular, we observe significant wave-function phase-shifts generated by domain-walls.

Mesoscopic effects in ferromagnets could be significantly different from mesoscopic effects in normal metals [99, 100, 101, 102]. While normal metals with a short mean-free-path do not exhibit classical magnetoresistance (MR), weakly disordered ferromagnets with a similar mean-free-path display MR, which includes domain-wall resistance (DWR) [103, 104, 105, 106, 107, 108, 109, 110, 111, 112, 113] and anisotropic magnetoresistance (AMR) [114]. MR could lead to novel mesoscopic effects because the wavefunction-phase depends on the scattering potential [101, 102].

Signatures of mesoscopic electron transport in ferromagnets have been reported [115, 116, 117, 118]. However, the dependence of the phase of the electron wavefunction on magnetization reversal processes have not been measured yet.

We present measurements of mesoscopic resistance fluctuations in cobalt nanoparticles and study how the fluctuations with bias voltage, bias fingerprints, respond to magnetization reversal processes.

6.1 Mesoscopic Systems

Mesoscopic systems are intermediate between microscopic and macroscopic systems [119, 120, 121]. Mesoscopic systems has the length scale which is much larger than atoms, but small enough not to show ohmic behavior. Mesoscopic electron transport has many major effects, several effects are related to our research namely the universal conductance fluctuations (UCF), weak localization (WL) and Aharonov-Bohm effect ($AB-effect$).

6.1.1 Characteristic Length Scales

Electron transport in mesoscopic systems depends on the relation between the sample dimensions and the following three characteristic length scales [120, 121].

Fermi wavelength: The Fermi wavelength λ_F is the de Broglie wavelength for electrons at the Fermi energy. The Fermi wavelength decreases when electron density (n_e) increases. At low temperature or the degenerate limit ($exp(E-E_F)/k_BT \ll 1$), the Fermi wavelength is given by [121]:

$$\lambda_F = 2\pi/k_F = \sqrt{2\pi/n_e} \tag{6.1}$$

At low temperature, only electrons close to the Fermi energy contribute to the conductance, so the Fermi wavelength is related to the current flow. Electron density n_e can be determined by Hall measurement, then we can get λ_F from 6.1.

Mean free path: The mean free path l_m represents the average distance that an electron travels before it collides with impurities or phonons which changes its initial momentum. l_m can be expressed as the multiply of the Fermi velocity v_F and the momentum relaxation time τ_m [122]:

$$l_m = v_F\tau_m \tag{6.2}$$

Phase relaxation length: The phase relaxation length L_φ is the distance at which the phase of electron wavefunction is destroyed. The dephasing processes are due to time-reversal breaking processes such as dynamic scattering (phonons) and electron-electron interactions [123]. Static scatterers do not contribute to dephasing, only dynamic scatterers do [121].

The relation between phase relaxation length L_φ and phase relaxation time τ_φ is not so straight forward as that of momentum relaxation.

If phase relaxation length L_φ is comparable or shorter than mean free path l_m, the electron transfer through a phase relaxation length is ballistic. Then we have

$$Ł_\varphi = v_F \tau_\varphi \tag{6.3}$$

If phase relaxation length is much longer than mean free path, the electron transfer through a phase relaxation length is diffusive. Electrons collide with elastic scatterers and move randomly over a phase relaxation length. With a simple argument [121], one have

$$Ł_\varphi^2 = v_F^2 \tau_\varphi \tau_m / 3 \tag{6.4}$$

6.1.2 Aharonov-Bohm Effect

Aharonov-Bohm effect [124] is a quantum interference phenomenon by which an electron is affected by the presence of a vector potential produced by an applied magnetic field. A ring-shaped conductor was used to perform the first Aharonov-Bohm effect measurement [123]. As shown in Figure 6.1, electron travel from left to the right through both the upper and the lower branch of the ring and the phase difference $\varphi_u - \varphi_l$ between those two paths is given by the total magnetic flux Φ enclosed by the ring. That is

$$\Phi = \frac{e}{\hbar} \oint_c \vec{A} dr \tag{6.5}$$

where $\vec{A}$ is the vector potential.

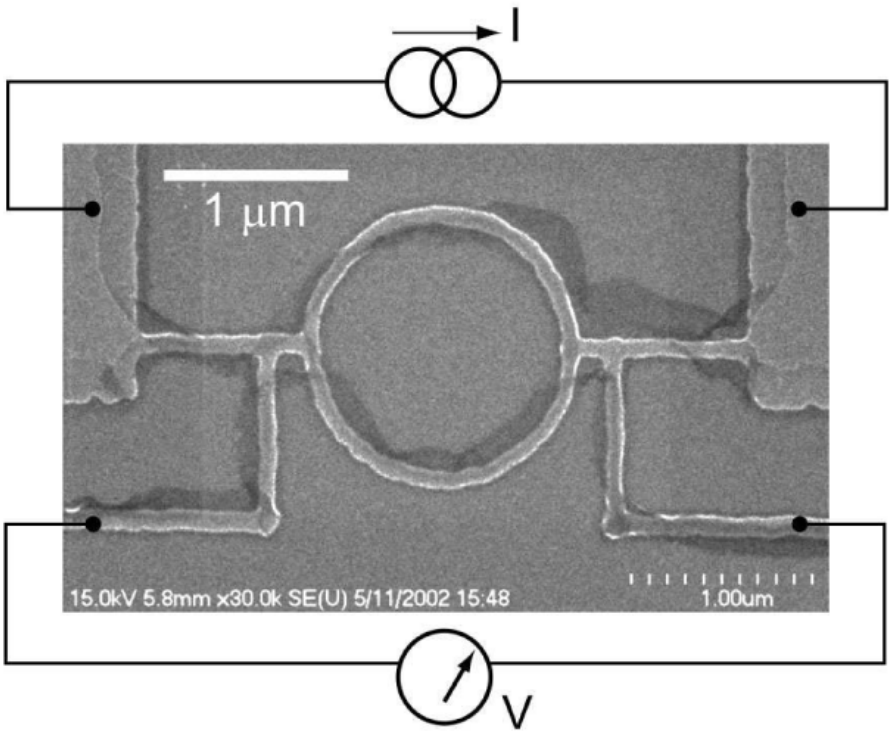

Figure 6.1: A ring-shaped conductor was used to perform Aharonov-Bohm effect measurement in cobalt.

By defining flux quantum $\Phi_0 = h/e$ the phase difference is $2\pi\Phi/\Phi_0$. We know that magnetic field $\vec{B} = \nabla \times \vec{A}$. So phase will oscillate at the period of h/e with changing the magnetic field. Assuming the uniform magnetic field, electron wavefunction phase change 2π when $B \times S = \Phi_0$, where $S = \text{Ł}_\varphi^2$ when Ł_φ^2 is smaller than the area enclosed by the ring.

6.1.3 Weak Localization

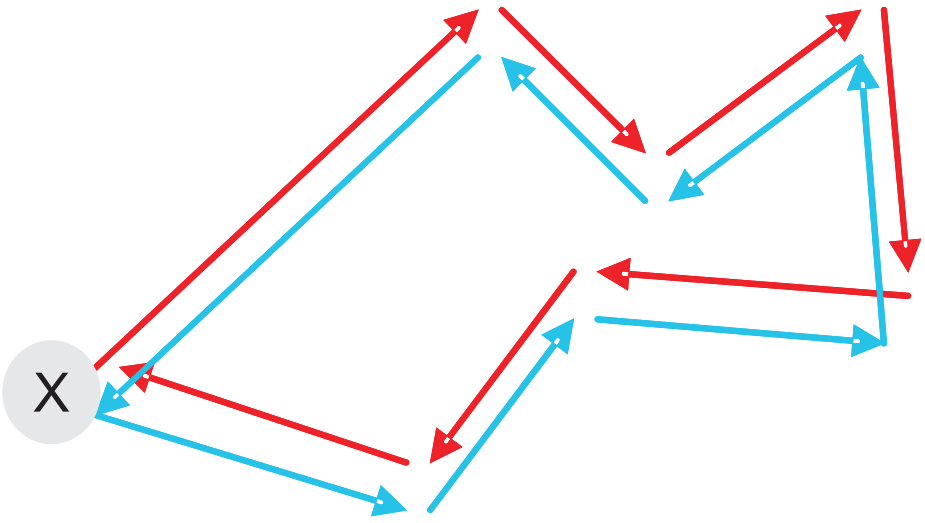

Figure 6.2: Cartoon of backscattering. Electron wave propagating in opposite direction interfere at the origin and create a coherent.

Weak localization is a quantum interference effect, which occurs in disordered electronic systems at very low temperatures. For disordered electronic systems at very low temperatures, phase relaxation length L_φ is much larger than mean free path l_m and comparable with the localization length $L_c = Ml_m$ (M is the number of conduction channels). Then when the sample length L is much smaller than localization length L_c, the conductor is in the weak localization regime.

In the weak localization regime, the average conductance $< G_{WL} >$ is smaller than the classic conductance G_{CL} by $\sim e^2/h$ [121]:

$$< G_{WL} > -G_{CL} \sim -e^2/h \tag{6.6}$$

The weak localization effect [125] can be explained by the enhanced backscattering due to quantum interference. Figure 6.2 is the cartoon of back scattering process. Electron propagates from point X along path *red* and comes back to the same point. Electron can also propagates starting and ending to point X along path *blue* which is a time reversal path of path *red*, then the amplitudes of path *red* and path *blue* are equal and coherent.

Thus, the quantum mechanical return probability

$$|P_c|^2 = |P_A + P_B|^2 = 4|P_A|^2 \tag{6.7}$$

If path A and path B are equal but incoherent, the sum of the corresponding probabilities

$$|P_{inc}|^2 = |P_A|^2 + |P_B|^2 = 2|P_A|^2 \tag{6.8}$$

Thus, the coherent backscattering probability is twice the classical value. Which explains the quantum conductance reduction compared to its classical value.

The coherent backscattering is limited by the phase coherence length L_φ, which decreases with temperature. At high temperature, sample dimensions L becomes larger than the phase coherence length L_φ [126].

Magnetic fields destroy the time reversal symmetry of the electronic motion and thus the weak localization effect vanishes, which is the unique signature of weak localization.

6.1.4 Universal Conductance Fluctuations

Universal conductance fluctuation is another quantum interference effect, which has random, but reproducible variations in a sample's conductance as a function of the applied magnetic field or the Fermi energy [43, 102, 127, 128]. The magnitude of the conductance fluctuations is about the same in different mesoscopic samples in the weak localization regime.

The conductance varies from sample to sample, but its root-mean-square (RMS) fluctuation

$$\Delta G \equiv \sqrt{\langle (G - \langle G \rangle)^2 \rangle} \sim e^2/h \tag{6.9}$$

does not depend on specific sample properties, such as the impurity configuration, the material, sample size or shape.

We have seen that the conductance fluctuations are about the same in phase coherent samples. What if sample size is much larger than phase coherence length L_φ ($L \gg L_\varphi$)? We could treat this large sample as $N = L/L_\varphi$ phase coherent samples in series [121]. The resistance fluctuation for each resistor is

$$\delta(G^{-1}) = \frac{\delta G}{G^2} \tag{6.10}$$

For N phase coherent samples (three dimension) in series, the conductance fluctuation (δG_N)is given by [121]

$$\delta G_N = G_N^2 \delta(G_N^{-1}) = \frac{\delta G}{N^{3/2}} \tag{6.11}$$

So the magnitude of conductance fluctuations decreases as sample size increases when ($L \gg L_\varphi$).

6.2 Domain walls and Magnetoresistance

A Domain walls (DW) is an interface separating magnetic domains with different magnetization directions. The length scale over which the magnetization direction changes is determined by material parameters (the exchange and magnetic anisotropy energies) as well as the sample geometry [103]. Within a DW, the material is chemically homogeneous and magnetization varies on a the scale of the domain wall width.

Domain walls scattering is a physical property that reflects both the electronic transport characteristics and the magnetic nature of a ferromagnetic material. It's a powerful tool that can provide direct information about magnetization reversal or domain-wall dynamics [110]. The effect of domain walls on the resistance of ferromagnetic metals has been widely studied during recent years [103, 129, 130, 131, 132, 133, 134, 135, 136].

Experimentally, the DW resistance are found out in some cases to be positive [104, 107, 110, 111]. whereas in other cases to be negative [108, 137].

The positive DW resistance was explained by Levy and Zhang [129]. They argued that diffuse scattering between electronic states of opposite spin orientation, which occurs in the process of electron transport across the rotating magnetization within a DW, leads to the mixing of spin-up and spin-down electrons due to the mistracking of the electron's spin on passing through the DW. Hence, the resistance increases. For negative DW resistance, Tatara and Fukuyama [101] demonstrated that DW can suppress weak localization due to the opening of additional conduction channels. As a consequence, resistance is lowered by forming DW.

A recent investigations point out that the negative DW resistance effect is mainly due to the anisotropic magnetoresistance (AMR) of the domain wall itself [132]. Generally, in measurements, domain wall resistance is superposed by a anisotropic magnetoresistance (AMR). The AMR is a contribution to the resistivity which depends on the relative directions of the current and magnetic field. This physical origin is that spin-orbit coupling leads to spin-dependent scattering of conduction electrons. AMR effect is weak ($\sim 1\%$). But, electron wave-vectors at the Fermi level may change sufficiently to cause a mesoscopic AMR. AMR effects resistivity as

$$\rho = \rho_0 + \Delta\rho \cos^2(\theta) \tag{6.12}$$

where θ is the angle between current and magnetization. So resistance is maximal when current and magnetization are parallel.

In this project, the major motivation is to study how the phase of the electron wave function responds to magnetization-reversal processes. Domain walls nucleation or annihilation associates with magnetization reversal processes. As we mentioned above, there is a mistracking effect when conduction electron spins lag behind the magnetic moments in the domain-wall [104, 105, 129, 107]. The conduction electron spin tracks the local exchange field well when the angular rotational period around the exchange field is much smaller

than the time of flight across the wall, which is equivalent to a large value of the tracking parameter $\xi = 2E_{ex}\delta_w/hv_F$. Here, E_{ex} is the exchange energy between conduction electron spins and the spins responsible for ferromagnetism. After a conduction electron traverses the wall, the angle between the exchange field direction and the conduction electron spin is $\theta = 1/\xi$ (Figure 8.7). This angular deviation increases the effective potential energy of the conduction electron by $\Delta = E_{ex}(1 - cos(\theta))$. The increase in effective potential energy contributes to DW resistance [104, 105, 129, 107]. In mesoscopic transport, however, electrons interfere among trajectories with diffusion times shorter than τ_ϕ, which leads to a correction in sample resistance. The wavefunction attains a phase-shift from this effective potential of $\Delta\tau_\phi/\hbar$, so we expect to observe mesoscopic fluctuations induced by the domain walls.

CHAPTER VII

EXPERIMENTS

Similar to double tunneling junctions devices in previous part, samples are made by electron beam lithography and shadow vapor deposition. It's critical to isolate the nanoparticle from any other ferromagnet to remove the influence of stray magnetic field from other magnetic parts of the device. Differential resistance is measured as a function of dc-bias voltage (V) and the applied magnetic field (B) at base temperature ($30mK$).

7.1 Sample Preparation

Since the similar techniques are used to prepare the nano-ferromagnet as to make the double tunneling junctions device. I am only going to emphasize the major steps of the sample preparation.

7.1.1 Electron Beam Lithography

Electron beam lithography is done over a bi-layer resist. The top layer is $PMMA$ with the thickness of $200nm$, the bottom layer is copolymer $MMA-MAA$ with the thickness of $800nm$. Four patterns are designed from nano-scale features to contact pads. By precisely applying certain doses to different patterns, a large undercut is created between contact pads and nano-magnet. The top view of the sample after development is shown in Figure 7.1. For better demonstration, Fig. 1 is not in scale as the real sample. The grey area is an uncovered area where both $PMMA$ and copolymer are removed. The solid purple area is an area where both $PMMA$ and copolymer are still attached to the substrate. In the shadowed area, the bottom layer has been removed while the top layer is suspended on the top of the substrate. The undercut between contact pads and nano-magnet is about $1.5\mu m$.

This large undercut serve as the mask for shadow deposition.

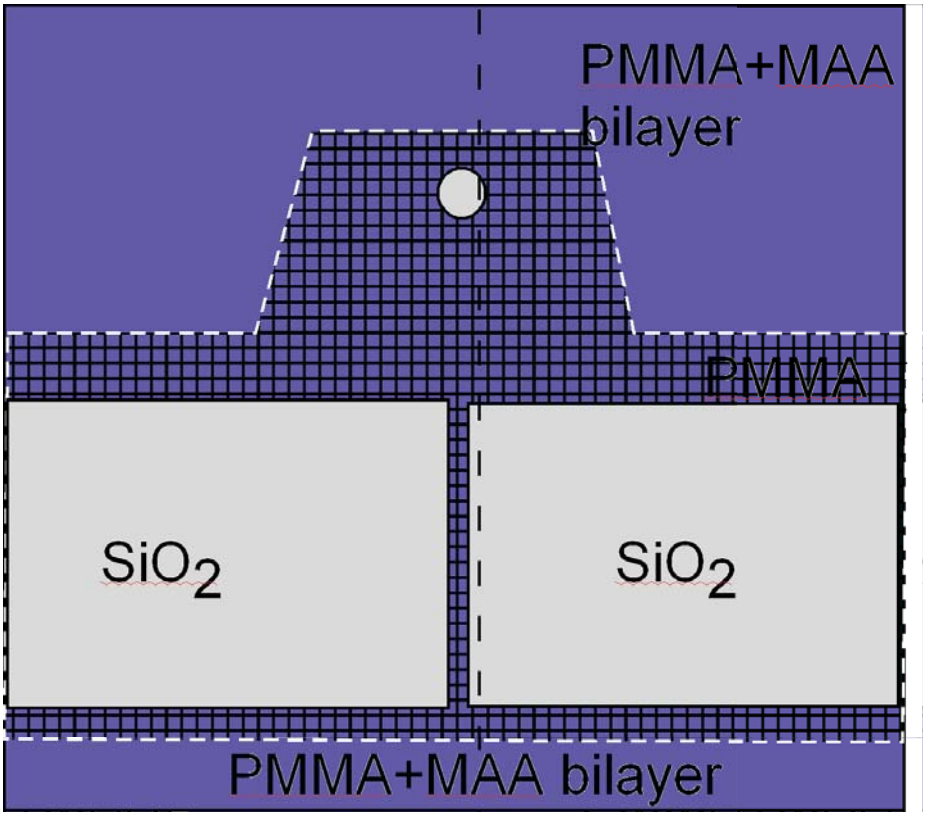

Figure 7.1: Top view of the pattern written by electron beam lithography: Electron beam lithography over a 2-layer resist, a suspended small bridge is formed.

7.1.2 Shadow Evaporation

Figure 7.2 shows the shadow deposition procedures by using the pattern defined by Electron Beam Lithography. First (Figure 7.2 A), a Co nanoparticle is deposited vertically at $10^{-7}Torr$ base pressure and a rate of $0.5nm/s$. Deposition is stopped when the Co thickness (t) reaches $10nm$. The Co nanoparticle is about $200nm$ in diameter. Other than depositing Co nanoparticle, a layer of Co is also deposited at the contact pads area. The Co nanoparticle is completely isolated from the Co at the contact pads area in a vicinity of $1.5\mu m$, by which removes the influence of stray magnetic field from Co contact pads.

Then we rotate the sample by 72° (Figure 7.2 B) without breaking the vacuum and

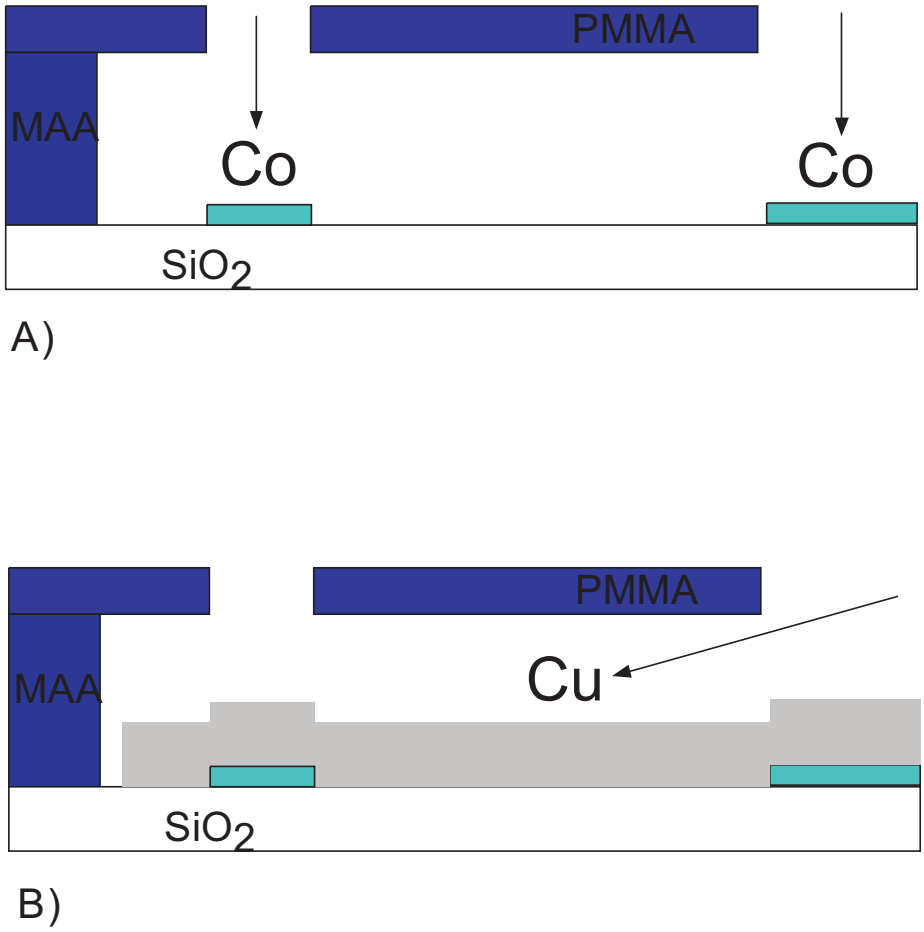

Figure 7.2: Shadow deposition procedures by using the pattern defined by Electron Beam Lithography. A) a Co nanoparticle is deposited vertically; B) Cu contact pads are deposited at a sharp angle.

deposit $50nm$ Cu at $0.5nm/s$. The Co nanoparticle is partially covered by Cu contact pads. The interface between Co and Cu is nearly free from adsorbates because the Co surface is exposed to base pressure for less than 10 seconds.

SEM image of a representative sample is shown in Figure 7.3. A Co particle of $200nm$ diameter and $10nm$ thickness is in electric contact with two Cu leads of $50nm$ thickness. The gap between Cu leads is about $100nm$.

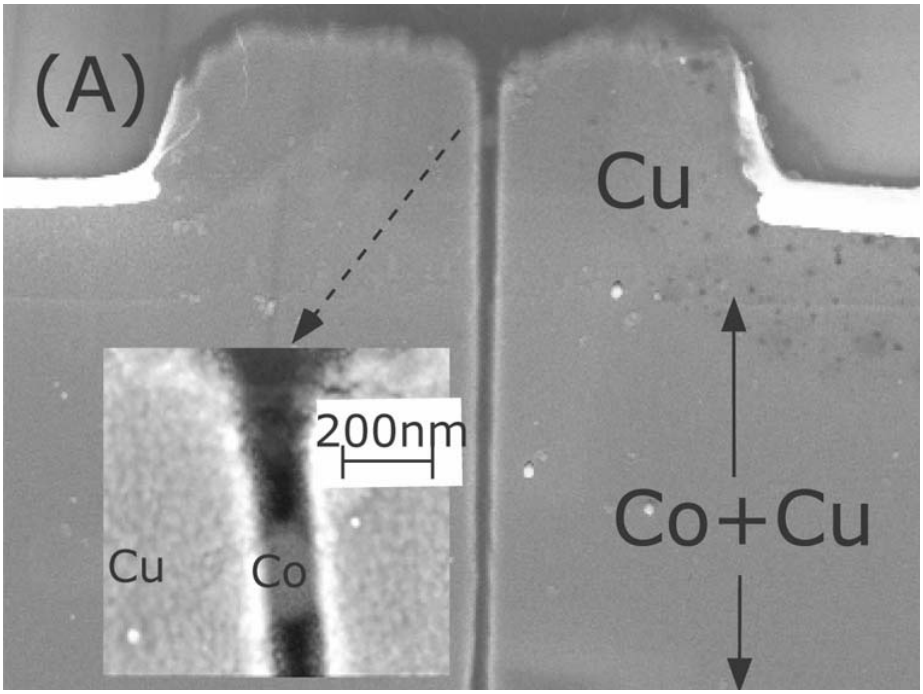

Figure 7.3: SEM image of a representative sample

The sample is exposed to air before transferred to a dilution refrigerator. The Co nanoparticle is oxidized at the surface not covered by Cu. Surface oxidation reduces the metal thickness and covers the film with a cobalt-oxide (CoO) layer. The time of air exposure before evacuation in the dilution refrigerator is less than one hour. We measure the resistance of Co films with various thicknesses *in situ* and monitor how the resistance increases when the films are exposed to air for one hour. We infer that the thickness of Co-metal is reduced by approximately $2nm$ after one hour of air exposure. The sheet resistance of the Co film at $4.2K$ temperature is $R_S \approx 120\Omega$, which is in agreement with the sheet

resistance of Co films of this thickness studied by other experimental group [114].

CoO is antiferromagnetic and the Co/CoO interface generates an exchange-bias effect in Co, [138, 139, 112] which leads to pinning of the magnetization and the enhancement of the coercive field. We expect that domain-walls (Figure 7.4) are nucleated at the interface between the exposed Co and unexposed Co (under Cu) by applying well defined magnetic fields, analogous to the similar behavior shown in Ref. [112]. The nanoparticle can support domains because the domain-wall width (δ_w) in Co ($\delta_w = 15nm$ [104, 105, 107]) is much smaller than the diameter.

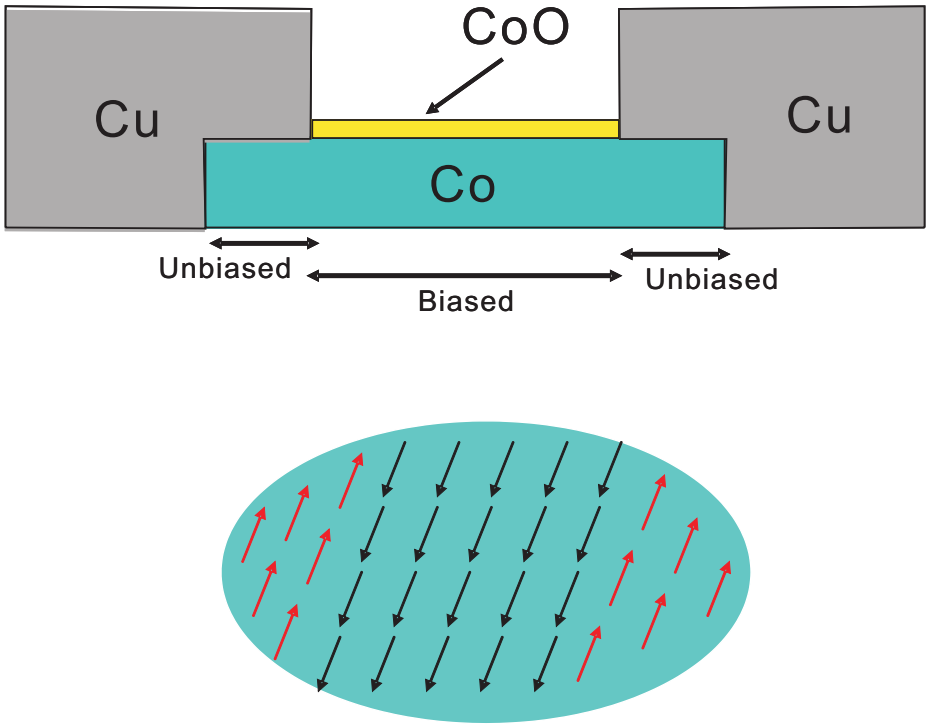

Figure 7.4: Cartoon of domain walls formation. We expect that domain-walls are nucleated at the interface between the exposed Co and unexposed Co (under Cu) by applying well defined magnetic fields.

7.2 Sample Measurements

Samples were studied at low temperatures in dilution refrigerator. Four probes were used to measure the resistance of Co nanoparticle. Two probes send current flow through the device, and the other two probes monitor the voltage drop across the device. Differential resistance ($r = dV/dI$) is measured as a function of DC-bias voltage (V) and (or) the applied magnetic field (B), ($r(V, B)$). The applied current is $I + icos(2\pi ft)$, where $i = 0.5\mu A$, and $f = 80Hz$. Then, r is obtained by measuring the AC-voltage across the sample with a lock-in amplifier. For measurement, the excitation voltage has to be low enough to avoid sample heating. At $0.03K$, we confirm that $r(V, B)$ is independent of i when $i < 0.5\mu A$. At $6K$, $r(B, V)$ is independent of i when $i < 2\mu A$. The resistance of Cu leads is about 10Ω and is not subtracted from r.

The out-of-plane (OP, magnetic field perpendicular to the film plane) and the in-plane (IP, magnetic field in plane and perpendicular to the current) MR are measured at low temperatures between -2.4T and 2.4T. The magnetic field is initially set to -12T, then it is reduced to -2.4T, and then it is cycled between -2.4T and 2.4T at the rate of $2.78 \cdot 10^{-4} s^{-1}$.

To study mesoscopic effects, we measured the dependence of r on two independent parameters, bias voltage (V) and magnetic field (B) [$r(V, B)$]. The dependence is obtained by quickly sweeping the bias voltage (at the rate of $0.003Hz$ between -4.2mV and 4.2mV), while the applied field is slowly changing (at the rate of $0.021T/min$ between -12T and 12T). We did measurement in both IP and OP configurations.

CHAPTER VIII

EXPERIMENTAL RESULTS AND DISCUSSION

8.1 Magnetoresistance at Low Temperatures

The OP and IP MR at $T = 6K$ were measured. First we discuss the $IP - MR$ (Figure 8.1) data. The magnetic field is initially set to $-12T$, then it is reduced to $-2.4T$, and then it is cycled between $-2.4T$ and $2.4T$.

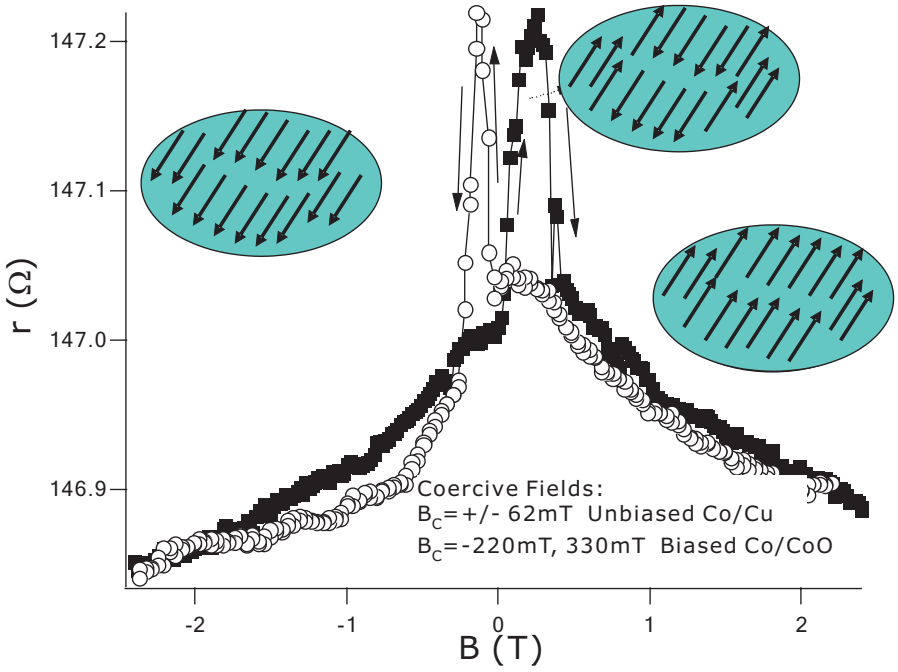

Figure 8.1: In-Plane MR. Two sharp peaks originate from AMR in domain walls.

The $IP - MR$ graph has hysteresis. There are two sharp resistance transitions in each field direction. The low and the high field transitions indicate nucleation and annihilation of domains, respectively. The smaller coercive fields are symmetric, $B_C = \pm 62mT$, which can

be explained if the magnetization is first reversed in unexposed Co (under Cu), as expected. The larger coercive fields are $330mT$ and $-220mT$. The magnetic moments in exchange biased Co change direction at these coercive fields. The coercive field is larger in magnitude when B increases, because B is initially $-12T$ [112, 140].

The resistance increases when the domains are nucleated. The increase is explained by the AMR inside the wall, which arises from the dependence of the conduction electron scattering rate on the angle between the current and the magnetization [114].

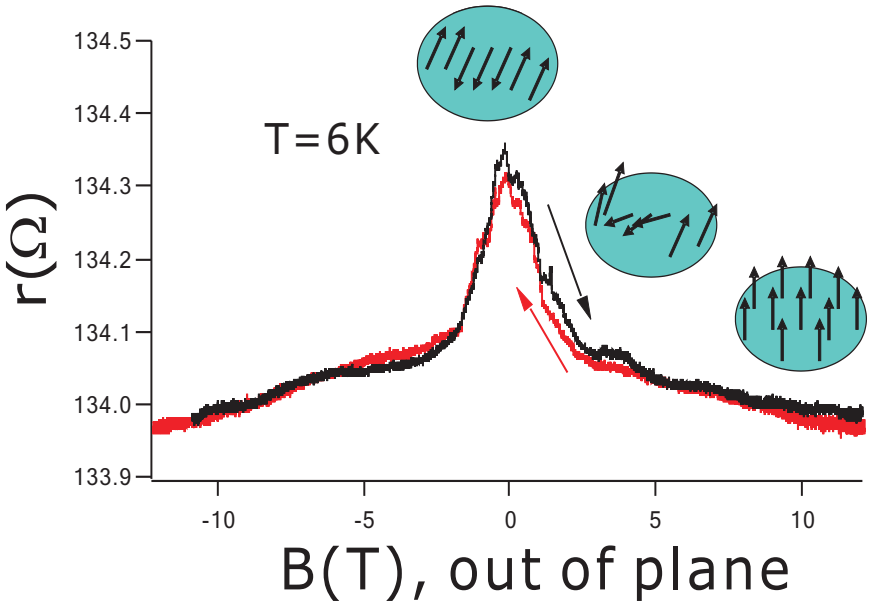

Figure 8.2: Out-of-plane MR. $OP-MR$ exhibits a broad maximum at $B=0$ and a weak hysteresis.

Next we discuss the $OP-MR$ in Figure 8.2. $OP-MR$ exhibits a broad maximum at $B=0$ and a weak hysteresis. The maximum is explained as arising from the rotation of magnetic moments supported by the domain wall magnetoresistance (explained before) and shape anisotropy (at high field, all the local magnetic moments are aligned with applied field, then current and magnetic moments are perpendicular to each other, which gives the lowest resistance (equation 6.12). As the applied field reduces to zero, the magnetic moments rotate into the film plane, the angle between magnetic moments and the current

is reduced, so r increases.).

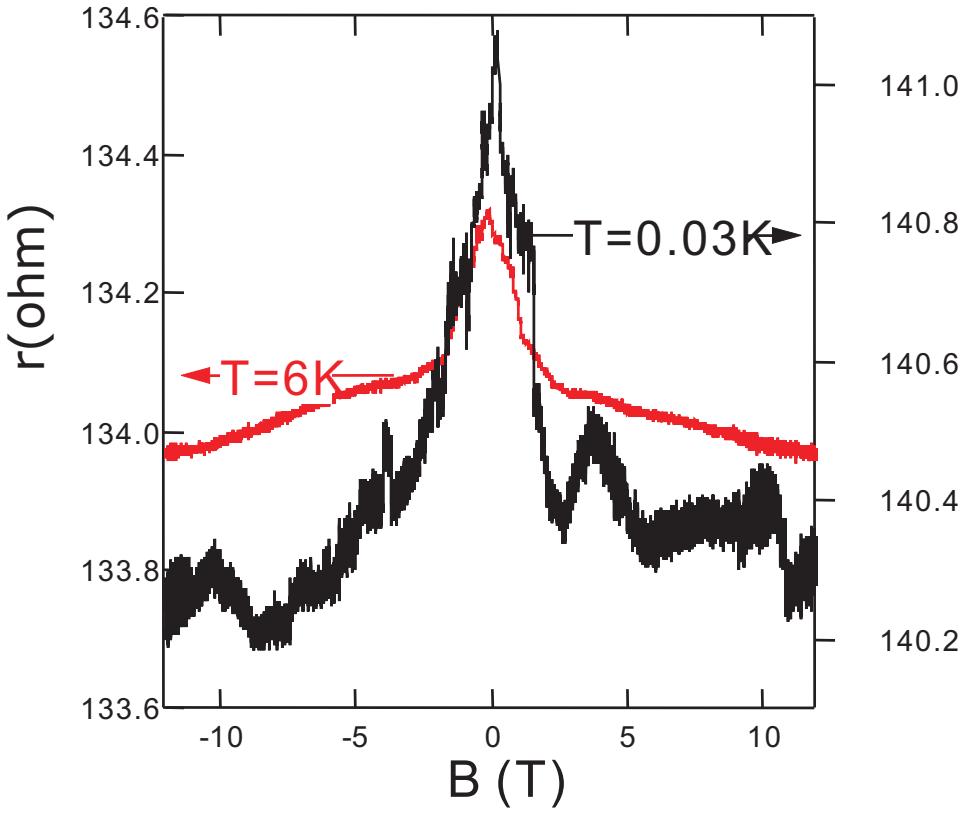

Figure 8.3: OP-MR measured at 6K (red) and 30mK (black). The differential resistance has fluctuations with magnetic field only at 30mK

We also measured the MR at $30mK$. The temperature dependence of $OP - MR$ is shown in Figure 8.3. (We describe the analysis of the OP- field data. The analysis of the IP-field data is equivalent. r and average MR are larger at 30mk than that at $6K$.) There are three major difference between 6K and 30mK results.

First, the differential resistance r is larger at 30mk than that at $6K$. The resistance increases by $\sim 6\Omega$ when the temperature drops from $6K$ to $30mK$. Similar effect is reported in Co films at temperatures above $1.5K$ [141] and is attributed to enhancement of electron-electron interactions caused by phase coherence [71]. An electron is scattered by the other electrons. An effective potential caused by those other electrons depends on L_φ, which is temperature dependent, and makes a resistivity correction at low temperature [121].

Next, the average MR at $30mK$ is enhanced compared to the AMR at $6K$. This enhancement suggests that weak localization effect contributes to MR at low temperatures. Prior research in Co-films did not find any weak localization effects at temperatures above $1.5K$ [141]. Our temperatures are much lower than $1.5K$, which could explain the difference between the results.

The weak localization MR contribution cannot be extracted from data because of the internal field of Co. The total magnetic field acting on conduction electrons in Co cannot be equal to zero; it is equal to the sum of the applied field and the internal field ($1.8T$), which is much larger than the coercive fields. Thus, the low-field contributions to quantum interference effects, such as weak antilocalization, are experimentally inaccessible.

Last, the resistance has fluctuations with magnetic field only at 30mK. I will discuss the fluctuations in details in next section.

8.2 Conductance Fluctuation and Magnetization Reversal Process

It was shown that the resistance fluctuated with magnetic field at 30mK above. The fluctuations are aperiodic and not reproducible when the field is varied arbitrarily. However, the fluctuations (Figure 8.4) are reproducible when B varies between two fields in the same direction after an initial training with one field cycle.

8.2.1 Extracting Conductance Fluctuations (CF)

To study mesoscopic effects, we obtain the dependence of r on two independent parameters, V and B $[r(V,B)]$ at 30mK as described previously. Figure 8.5-A displays $r(V,B)$ when B is OP. The brighter the color, the larger the resistance. So the cross in this image displays maximums in resistance versus field and voltage, centered at zero field and voltage, respectively.

The average resistance versus field and voltage are defined as $r_0(B) = \int_{-V_{max}}^{V_{max}} r(V,B)dV/2V_{max}$

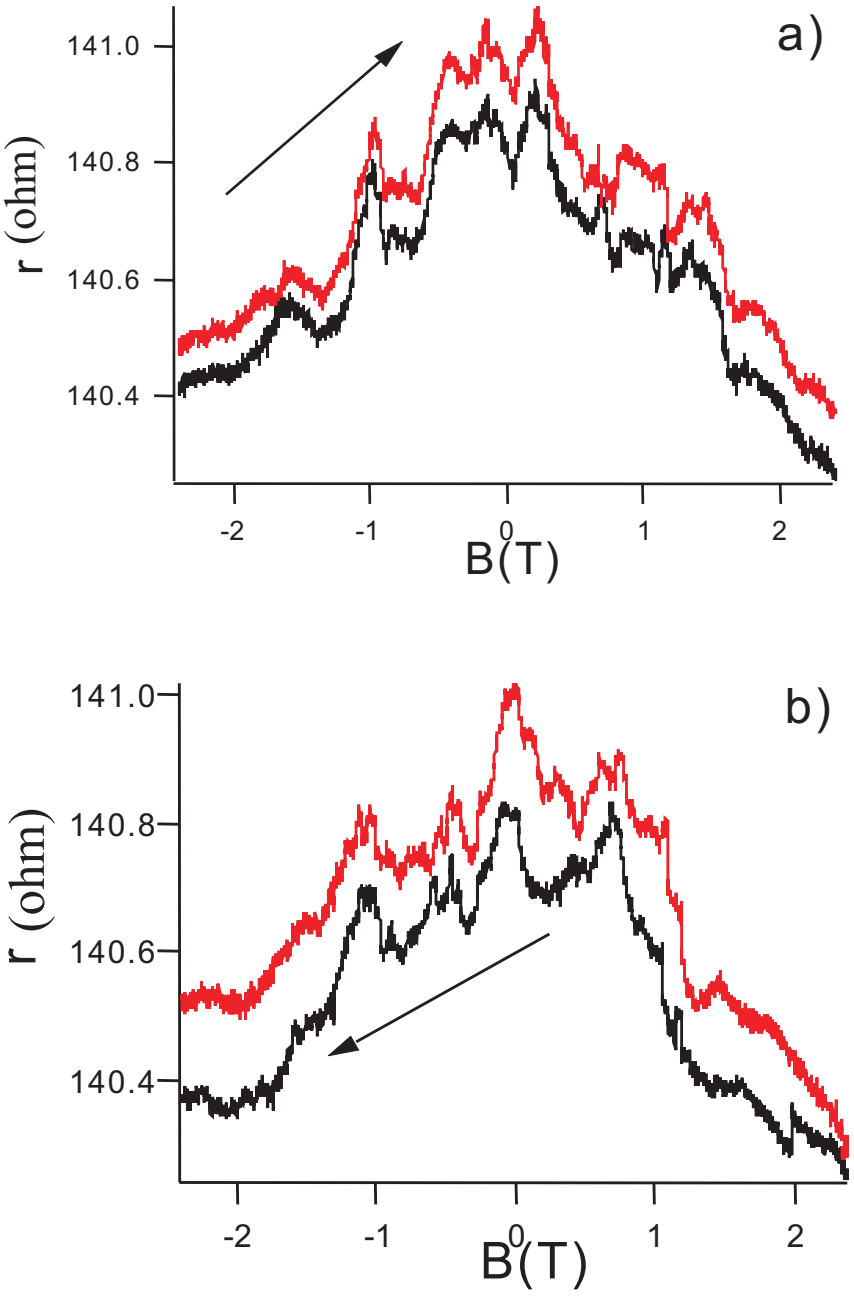

Figure 8.4: Conductance Fluctuation at 30mK. The fluctuations are aperiodic but reproducible when B varies between two fields in the same direction after an initial training with one field cycle.

and $r_0(V) = \int_{-B_{max}}^{B_{max}} r(V,B)dB/2B_{max}$, respectively, where $B_{max} = 12T$, and $V_{max} = 4.2mV$. The averages are shown in Figures 8.5-B and C. The resistance averaged over both V and B is $r_0 = 140\Omega$.

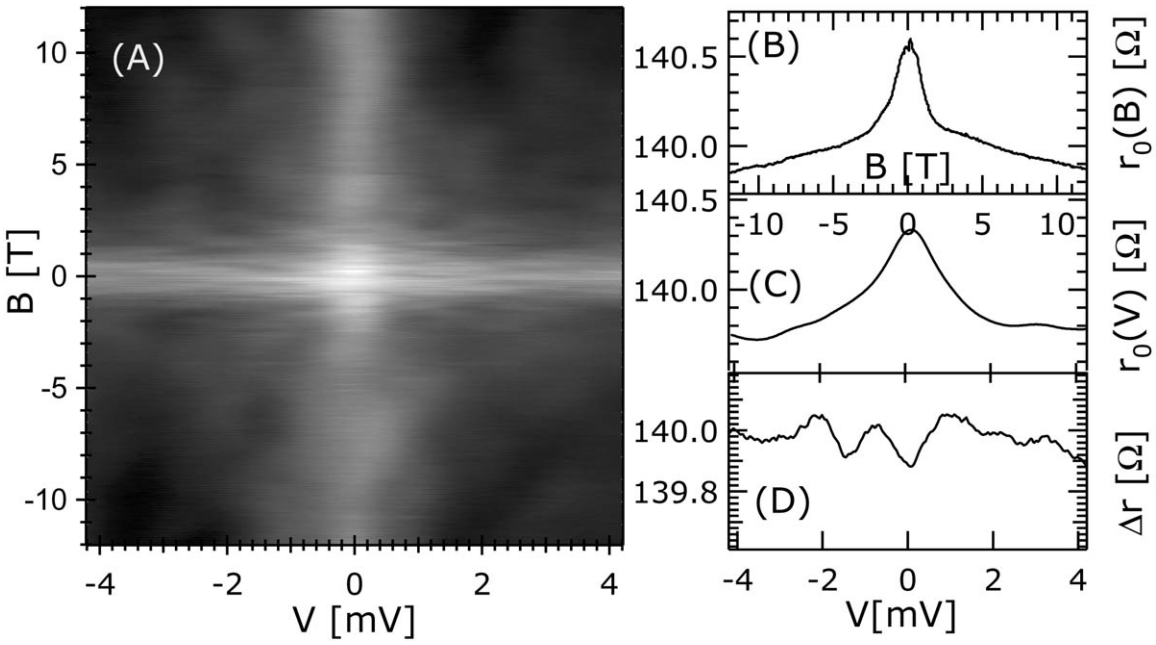

Figure 8.5: A: Differential resistance (r) versus bias voltage and out-of-plane magnetic field at 0.03K. B and C: Average resistance versus out-of-plane field and bias voltage, respectively, defined in text. D: Fluctuations in resistance with bias voltage, $r(V,B) - r_0(V) + r_0$, at $B = -5.5T$.

The resistance maximum with field in Figure 8.5-B is due to average MR ($WL + AMR$) effect in mesoscopic samples [142]. Resistance fluctuations in Figure 8.5-A are superimposed with the EE-effect [142] and the average MR. To better display the fluctuations in resistance with voltage, we find the difference between $r(V,B)$ and the average EE-effect in Figure 8.5-C. The resulting resistance as a function of voltage at fixed field is shown in Figure 8.5-D. The resistance now clearly exhibits fluctuations with voltage. The fluctuations are reproducible and are found at low temperatures only.

The fluctuations in r with V represent changes in electron interference from constructive to destructive as a function of electron energy [45]. Root-mean-square (rms) of the

fluctuations is 0.1Ω, which corresponds to $rms - CF$ of $0.05e^2/h$ ($\delta g_0 = \delta r_0/r_0^2$). The fluctuation amplitude is $\ll e^2/h$, showing that the dephasing time must be much shorter than the transport time. The rms does not change with V, showing that the heating effects are weak.

The correlation voltage V_C is given by the average spacing between minima and maxima, $V_C \sim 1mV$. The meaning of V_C is that changing the electron energy by eV_C changes the electron-phase by π. V_C is related to the dephasing time τ_ϕ as $|e|V_C = \hbar/\tau_\phi$ [121], so $\tau_\phi = 0.7ps$.

8.2.2 Conductance Fluctuation Induced by the Magnetization Reversal Process

To display the fluctuating part of the resistance at different magnetization configurations, we subtract the average EE-effect and MR from the resistance. The background has characteristic voltage and field scales much larger than the voltage and field correlation scales for fingerprints. Background subtraction has negligible effect on the correlation scales. To display the fluctuating part of the resistance at different magnetization configurations, we subtract the average EE-effect and MR from the resistance. Four red-white-blue images in Figure 8.6 display CFs with magnetic field and bias voltage at 30mK refrigerator temperature. Red and blue regions indicate larger and smaller resistance, respectively.

The fluctuations with field and voltage, represented in Fig. 8.4, are not reproducible when the field is varied arbitrarily. However, the fluctuations are reproducible when B varies between two fields in the same direction after an initial training with one field cycle.

In Figure 8.6-A and B, there is a noticeable difference between dependence of the bias-fingerprints on the IP and the OP-fields. If the IP-field varies from -2T to 0, the resistance maxima and minima with voltage shift weakly. By contrast, when B is changing OP, bias-fingerprints shift or rearrange several times. These rearrangements are indicated by the appearances and disappearances of the red and blue regions in Figure 8.6-B.

Figure 8.6-C shows that bias fingerprints vary weakly with the IP-field in the field range $-12T < B < 0$. But, when the IP-field changes sign and reaches the coercive field, the

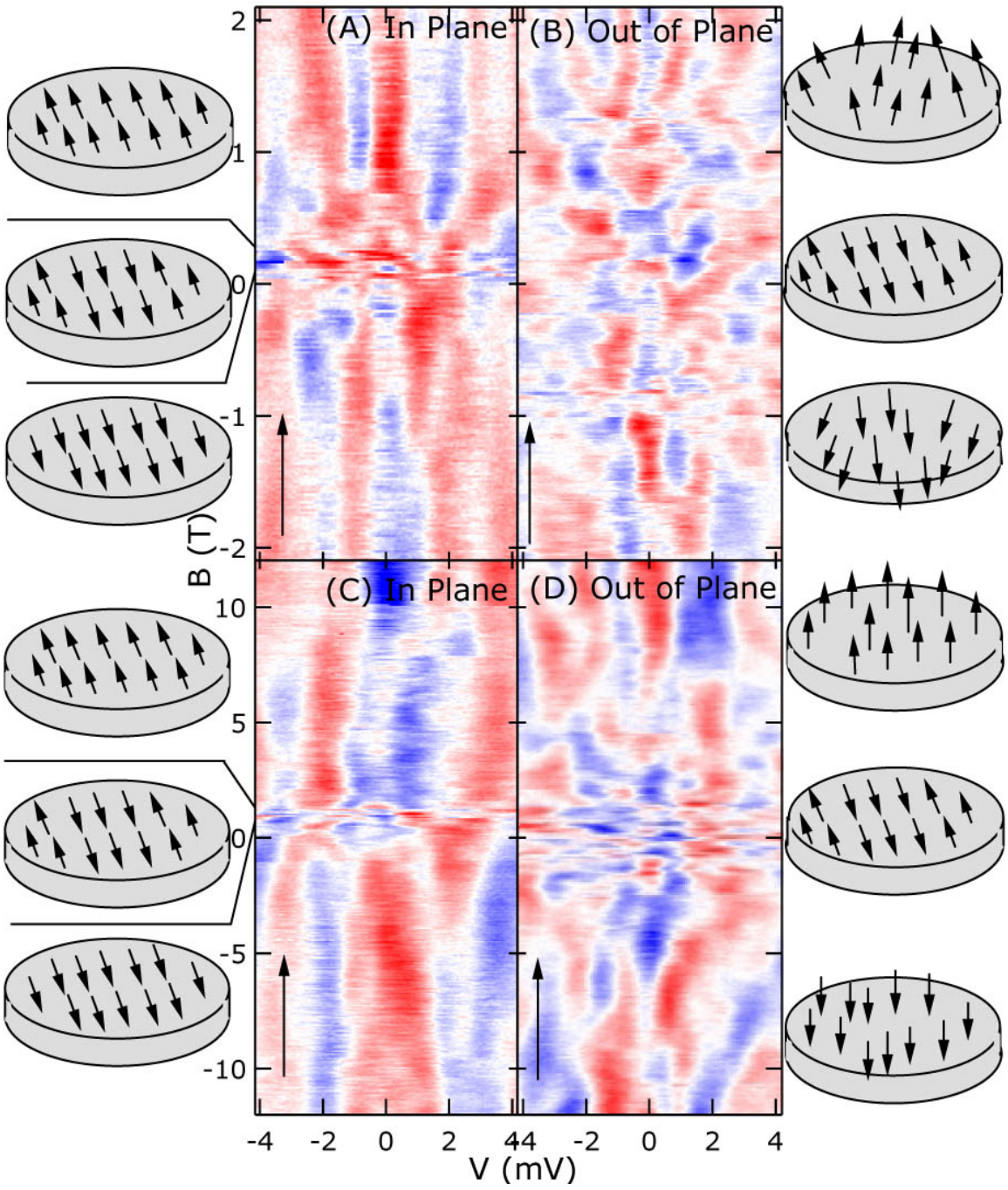

Figure 8.6: A and B: Fluctuations in differential resistance, $r(V,B) - r_0(V) - r_0(B)$, with V and the IP-field and the OP-field, respectively. C and D: same as A and B, but in a wider field range. The minima and the maxima of differential resistance with B and V correspond to constructive and destructive electron interference, as described in text. The schematics indicate the expected magnetic configurations

bias-fingerprints rearrange at the coercive field. This shows that the domain-walls generate significant electron-phase shifts, at least on the order of π.

Before discussing the physical origin of the rearrangements in bias-fingerprints, we analyze the strong field data in Figure 8.6-C and D, $2T < |B| < 12T$. Comparing Figure. 8.6-C and Figure 8.6-D in this field-range, we observe that bias fingerprints vary faster with the OP-field. Alternatively, the characteristic field scale, which rearranges the bias-fingerprint in strong field, is smaller in the OP-direction. The correlation field B_C is the average spacing between the red and the blue regions along B axes; $B_C \approx 4T$ and it is weakly dependent on V, confirming that the heating is not significant.

In a strong OP-field, magnetization is saturated and B_C is given by the field for a flux quantum over the phase coherent area, Φ_0/L_ϕ^2, where $\Phi_0 = h/e$ is the flux quantum, and L_ϕ is the dephasing length. We find $L_\phi \approx 30nm$. Assuming a mean-free-path $l = 5nm$ and the Fermi velocity $v_F = 1.4 \cdot 10^6 m/s$, the electron dephasing time is $L_\phi^2/(v_F l/3) = 0.4ps$, in agreement with τ_ϕ obtained before, within an order of magnitude. In the IP-direction, B_C is larger; because the phase coherent area perpendicular to the field is smaller, $B_C = \Phi_0/tL_\phi \approx 12T$.

Now we discuss the rearrangements in bias-fingerprints at the coercive fields, Figure 8.6-A and Figure 8.6-C. The internal field switches at the coercive fields. In Co, the internal field change is less than $3.6T$, much smaller than the IP-field for a flux quantum ($12T$). So the $Aharonov - Bohm$ phase cannot be responsible for the rearrangements.

Figure 8.6-D shows that the density of red and blue regions increases when $|B| < 1.5T$. In Figure 8.6-B, there are about five red and blue regions along B-axes between 0 and 1.5T. This shows that the magnetization rotation from IP to OP direction creates a phase-shift along a typical phase coherent electron trajectory of about 5π. Since the total field (internal plus applied) changes by $< 3.3T$ in this applied field range and the OP-field for a flux quantum is $4T$, five resistance minima and maxima cannot originate from the $Aharonov - Bohm$ phase.

A variety of effects could lead to wave-function phase-shifts in mesoscopic ferromagnets.

We show that the phase-shift could originate from a weak mistracking effect when conduction electron spins lag behind the magnetic moments in the domain-wall [104, 105, 129, 107]. The conduction electron spin tracks the local exchange field well when the angular rotational period around the exchange field is much smaller than the time of flight across the wall, which is equivalent to a large value of the tracking parameter $\xi = 2E_{ex}\delta_w/hv_F$. Here, E_{ex} is the exchange energy between conduction electron spins and the spins responsible for ferromagnetism. After a conduction electron traverses the wall, the angle between the exchange field direction and the conduction electron spin is $\theta = 1/\xi$ (Figure 8.7).

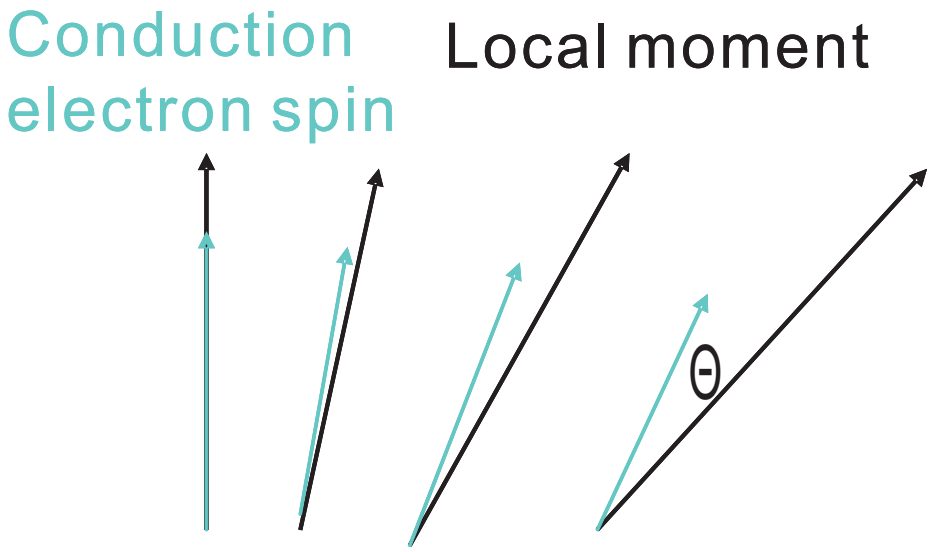

Figure 8.7: Cartoon of the electron transfer through the domain wall. Electron spin mistrack the local moments by an angle θ, transport is weakly unparallel.

Using $E_{ex} = 1eV$ and $\delta_w = 15nm$, one obtains $\xi \approx 7.3$ [104]. The angular deviation increases the effective potential energy of the conduction electron by $\Delta = E_{ex}(1 - cos(\theta)) \approx 9meV$. The increase in effective potential energy contributes to DWR [104, 105, 129, 107]. In mesoscopic transport, however, electrons interfere among trajectories with diffusion times shorter than τ_ϕ, which leads to a correction in sample resistance. The wavefunction attains a phase-shift from this effective potential of $\Delta\tau_\phi/\hbar \approx 4.8\pi$. The phase-shift is reduced to zero when the magnetic moments become parallel with each other. So the bias-fingerprints

should rearrange about 5 times when the moment rotate from IP-direction into the OP-direction.

An alternative mechanism was recently proposed in ref. [102]. Quantum interference leads to an additional random dependence of the conductance on the magnetization direction. As a result, conductance fluctuations occur as a function of the magnetization orientation. Our experimental results are also in agreement with ref. [102].

The dephasing length of $L_\phi = 30nm$ is very short. we measured two Co nanowires of lengths $500nm$ and $800nm$ and width $100nm$ at $T = 30mK$. These nanowires displayed no conductance fluctuations, confirming that $L_\phi \ll 500nm$.

The dephasing process in ferromagnets is not well understood. In permalloy, experiments suggest that two level systems are important sources of dephasing [118]. Theoretically, domain-walls were are found to reduce the dephasing length [101]. But, the dephasing time $\tau_\phi = \hbar/eV_C$ in our samples is independent of B, because V_C does not vary significantly with B; τ_ϕ in strong field, in a single domain state, is approximately the same as τ_ϕ at $B = 0$ when domains are present. This demonstrates that the domain-walls are not responsible for short τ_ϕ.

The phase of the wavefunction is extremely sensitive to the position/presence of domain-walls, as indicated by the rearrangement of bias fingerprints in Figure 8.6. The absence of domain-wall contribution to dephasing shows that the electron interaction with the wall must be elastic. This situation is analogous to the sensitivity of conductance fluctuation with respect to changes in the impurity configurations. [45, 43, 44] In a thin film mesoscopic sample, motion of an impurity by the Fermi wavelength rearranges CFs. Nevertheless, the impurities do not contribute to dephasing when electron scattering is elastic.

Kasai, *et al.*, found very short L_ϕ in Ni, $L_\phi \approx 80nm$ [117]. Small L_ϕ is correlated with the large magnetocrystalline anisotropy in Ni; the dephasing length in permalloy, which has negligible magnetocrystalline anisotropy, is $500nm$. Since the magnetocrystalline anisotropy in Co is stronger than that in Ni, the dephasing length of 30nm in Co agrees with the trend that L_ϕ decreases with magnetocrystalline anisotropy [117].

CHAPTER IX

CONCLUSIONS

We successfully created the well-defined domain walls in a ferromagnetic Co nanoparticle by partially covering the Co with an antiferromagnetic CoO thin film. Which enables us to present measurements of mesoscopic resistance fluctuations in cobalt nanoparticles and study how the fluctuations with bias voltage, bias fingerprints, respond to magnetization reversal processes.

By applying OP and IP magnetic fields, domain walls are created at the interface between biased (covered by CoO) and unbiased Co. Bias fingerprints rearrange when domains are nucleated or annihilated during magnetization-reversal process in a Co nanoparticle. The domain-wall causes an electron wavefunction phase-shift of $\approx 5\pi$. The phase-shift is not caused by the Aharonov-Bohm effect; it arises from the mistracking effect, where electron spins lag in orientation with respect to the moments inside the domain-wall.

The dephasing length at low temperatures is only $30nm$, which is attributed to the large magnetocrystalline anisotropy in Co, in agreement with the trend established before, but not understood theoretically.

APPENDIX A

LIST OF SYMBOLS

h	Planck Constant (6.62×10^{-34} Js)
k_B	Boltzman constant(1.38×10^{-23} J/K)
nm	nanometer (10^{-9} m)
$\mathring{A}$	Unit of length, Angstrom (10^{-10}m)
Ω	Ohm
E_C	Charging energy
CF	Conductance fluctuation
DW	Domain Wall
Q_0	fractional residue charge
K	Kelvin
Torr	Unit of pressure, equal to 133.32 Pa
e	Charge of an electron
eV	electron volt
G	Differential conductance
I	Current
R	Resistance
r	Differential Resistance
U	Electrostatic Energy
V_{bias}	Bias Voltage
τ	Relaxation Time
f	Frequency
T	Temperature
t	Time

T_1	longitudinal spin relaxation time
T_2	spin dephasing time
M	Magnetization
DOS	Density Of State
P	Spin Polarization
T_c	Critical Temperature
MTJ	Magnetic Tunnel Junction
SDT	Spin-Dependent Tunnelling
MRAM	Magneto random access memories
FM/I/FM	Ferromagnetic Insulator Ferromagnetic
AP	Antiparallel
DW	Domain Wall
AMR	anisotropic Magneto Resistance
TMR	Tunnel Magneto Resistance
GMR	Giant Magnetoresistance
PMMA	PolyMethyl MethAcrylate
IPA	Isopropanol
SCCM	unit of flow, standard cubic centimeter per minute
SEM	Scanning Electron Microscope

APPENDIX B

PUBLISHED PAPERS

Y. G. Wei, X. Y. Liu, L. Y. Zhang, and D. Davidović, "Mesoscopic Resistance Fluctuations in Cobalt Nanoparticles," Physical Review Letters 96, 146803 (2006).

Y. G. Wei, C. E. Malec, D. Davidović, "Saturation of Spin-Polarized Current in Nanometer Scale Aluminum Grains," Accepted by physical Review B, (2007).

L. Y. Zhang, C. Y. Wang, Y. G. Wei, X. Y. Liu, and D. Davidović, "Spin-Polarized Electron Transport through Nanometer-Scale Al Grains," Physical Review B 72, 155445 (2005).

REFERENCES

[1] S. A. Wolf, D. D. Awschalom, R. A. Buhrman, J. M. Daughton, S. von Molnar, M. L. Roukes, A. Y. Chtchelkanova, and D. M. Treger, "Spintronics: A spin-based electronics vision for the future," *Science* **294**, 1488 (2001).

[2] I. Zutic, J. Fabian, and S. D. Sarma, "Spintronics: Fundamentals and applications," *Rev. Mod. Phys.* **76**, 323 (2004).

[3] P. Seneor, A. Bernand-Mantel, and F. Petroff, "Nanospintronics: when spintronics meets single electron physics," *Journal Of Physics-Condensed Matter* **19**, 165222 (2007).

[4] M. M. Deshmukh, S. Kleff, S. Gueron, E. Bonet, A. N. Pasupathy, J. von Delft, and D. C. Ralph, "Magnetic anisotropy variations and nonequilibrium tunneling in a cobalt nanoparticle," *Physical Review Letters* **8722**, 226801 (2001).

[5] M. M. Deshmukh and D. C. Ralph, "Using single quantum states as spin filters to study spin polarization in ferromagnets," *Physical Review Letters* **89**, 266803 (2002).

[6] H. FUJIMORI, S. MITANI, and S. OHNUMA, "Tunnel-Type Gmr In Metal-Nonmetal Granular Alloy Thin-Films," *Materials Science And Engineering B-Solid State Materials For Advanced Technology* **31**, 219 (1995).

[7] L. Y. Zhang, C. Y. Wang, Y. G. Wei, X. Y. Liu, and D. Davidovic, "Spin-polarized electron transport through nanometer-scale Al grains," *Physical Review B* **72**, 155445 (2005).

[8] J. M. Kikkawa, I. P. Smorchkova, N. Samarth, and D. D. Awschalom, "Room-temperature spin memory in two-dimensional electron gases," *Science* **277**, 1284 (1997).

[9] J. A. Gupta, D. D. Awschalom, X. Peng, and A. P. Alivisatos, "Spin-coherence in semiconductor quantum dots (vol 59, pg R10421, 1999)," *Physical Review B* **60**, 8394 (1999).

[10] G. Burkard, H. A. Engel, and D. Loss, "Spintronics and quantum dots for quantum computing and quantum communication," *Fortschritte Der Physik-Progress of Physics* **48**, 965 (2000).

[11] D. Loss and D. P. Divincenzo, "Quantum computation with quantum dots," *Physical Review A* **57**, 120 (1998).

[12] A. V. Khaetskii and Y. V. Nazarov, "Spin relaxation in semiconductor quantum dots," *Physical Review B* **61**, 12639 (2000).

[13] A. V. Khaetskii and Y. V. Nazarov, "Spin-flip transitions between zeeman sublevels in semiconductor quantum dots," *Physical Review B* **6412**, 125316 (2001).

[14] T. Fujisawa, D. G. Austing, Y. Tokura, Y. Hirayama, and S. Tarucha, "Allowed and forbidden transitions in artificial hydrogen and helium atoms," *Nature* **419**, 278 (2002).

[15] J. M. Elzerman, R. Hanson, L. H. W. van Beveren, B. Witkamp, L. M. K. Vandersypen, and L. P. Kouwenhoven, "Single-shot read-out of an individual electron spin in a quantum dot," *Nature* **430**, 431 (2004).

[16] A. C. Johnson, J. R. Petta, J. M. Taylor, A. Yacoby, M. D. Lukin, C. M. Marcus, M. P. Hanson, and A. C. Gossard, "Triplet-singlet spin relaxation via nuclei in a double quantum dot," *Nature* **435**, 925 (2005).

[17] A. V. Khaetskii, D. Loss, and L. Glazman, "Electron spin decoherence in quantum dots due to interaction with nuclei," *Physical Review Letters* **88**, 186802 (2002).

[18] R. J. Elliott, "Theory of the effect of spin-orbit coupling on magnetic resonance in some semiconductors," *Physical Review* **96**, 266 (1954).

[19] Y. Yafet, "G-factors and spin-lattice relaxation of conduction electrons," *Solid State Physics-Advances in Research and Applications* **14**, 1 (1963).

[20] J. Fabian and S. Das Sarma, "Spin relaxation of conduction electrons in polyvalent metals: Theory and a realistic calculation," *Physical Review Letters* **81**, 5624 (1998).

[21] J. Fabian and S. Das Sarma, "Phonon-induced spin relaxation of conduction electrons in aluminum," *Physical Review Letters* **83**, 1211 (1999).

[22] J. Fabian and S. Das Sarma, "Band-structure effects in the spin relaxation of conduction electrons (invited)," *Journal of Applied Physics* **85**, 5075 (1999).

[23] F. J. Jedema, H. B. Heersche, A. T. Filip, J. J. A. Baselmans, and B. J. van Wees, "Electrical detection of spin precession in a metallic mesoscopic spin valve," *Nature* **416**, 713 (2002).

[24] W. P. Halperin, "Quantum size effects in metal particles," *Rev. Mod. Phys.* **58**, 533 (1986).

[25] P. W. Brouwer, X. Waintal, and B. I. Halperin, "Fluctuating spin g-tensor in small metal grains," *Physical Review Letters* **85**, 369 (2000).

[26] K. A. Matveev, L. I. Glazman, and A. I. Larkin, "g-factors of discrete levels in nanoparticles," *Physical Review Letters* **85**, 2789 (2000).

[27] M. M. Deshmukh, E. Bonet, A. N. Pasupathy, and D. C. Ralph, "Equilibrium and nonequilibrium electron tunneling via discrete quantum states," *Physical Review B* **65**, 073301 (2002).

[28] O. Agam, N. S. Wingreen, B. L. Altshuler, D. C. Ralph, and M. Tinkham, "Chaos, interactions, and nonequilibrium effects in the tunneling resonance spectra of ultrasmall metallic particles," *Physical Review Letters* **78**, 1956 (1997).

[29] M. Johnson and R. H. Silsbee, "Interfacial charge-spin couplinginjection and detection of spin magnetization in metals," *Physical Review Letters* **55**, 1790 (1985).

[30] C. D. Chen, Y. D. Yao, S. F. Lee, and J. H. Shyu, "Magnetoresistance study in Co-Al-Co and Al-Co-Al double tunneling junctions," *Journal of Applied Physics* **91**, 7469 (2002).

[31] K. Ono, H. Shimada, S. Kobayashi, and Y. Ootuka, "Magnetoresistance of Ni/NiO/Co small tunnel junctions in Coulomb blockade regime," *Journal of the Physical Society of Japan* **65**, 3449 (1996).

[32] K. Ono, H. Shimada, and Y. Ootuka, "Enhanced magnetic valve effect and magneto-Coulomb oscillations in ferromagnetic single electron transistor," *Journal of The Physical Society of Japan* **66**, 1261 (1997).

[33] J. Barnas and A. Fert, "Magnetoresistance oscillations due to changing effects in double ferromagnetic tunnel junctions," *Physical Review Letters* **80**, 1058 (1998).

[34] J. Barnas and A. Fert, "Effects of spin accumulation on single-electron tunneling in a double ferromagnetic microjunction," *Europhysics Letters* **44**, 85 (1998).

[35] S. Takahashi and S. Maekawa, "Effect of Coulomb blockade on magnetoresistance in ferromagnetic tunnel junctions," *Physical Review Letters* **80**, 1758 (1998).

[36] K. Majumdar and S. Hershfield, "Magnetoresistance of the double-tunnel-junction Coulomb blockade with magnetic metals," *Physical Review B* **57**, 11521 (1998).

[37] A. Brataas, Y. V. Nazarov, J. Inoue, and G. E. W. Bauer, "Non-equilibrium spin accumulation in ferromagnetic single-electron transistors," *European Physical Journal B* **9**, 421 (1999).

[38] A. Brataas, Y. V. Nazarov, J. Inoue, and G. E. W. Bauer, "Spin accumulation in small ferromagnetic double-barrier junctions," *Physical Review B* **59**, 93 (1999).

[39] J. Martinek, J. Barnas, G. Michalek, B. R. Bulka, and A. Fert, "Spin effects in single-electron tunneling in magnetic junctions," *Journal of Magnetism and Magnetic Materials* **207**, L1 (1999).

[40] J. Barnas, J. Martinek, G. Michalek, B. R. Bulka, and A. Fert, "Spin effects in ferromagnetic single-electron transistors," *Physical Review B* **62**, 12363 (2000).

[41] J. Martinek, J. Barnas, A. Fert, S. Maekawa, and G. Schon, "Transport in magnetic nanostructures in the presence of Coulomb interaction," *Journal of Applied Physics* **93**, 8265 (2003).

[42] A. Bernand-Mantel, P. Seneor, N. Lidgi, M. Munoz, V. Cros, S. Fusil, K. Bouzehouane, C. Deranlot, A. Vaures, F. Petroff, and A. Fert, "Evidence for spin injection in a single metallic nanoparticle: A step towards nanospintronics," *Applied Physics Letters* **89**, 062502 (2006).

[43] P. A. LEE and A. D. STONE, "Universal Conductance Fluctuations In Metals," *Physical Review Letters* **55**, 1622 (1985).

[44] B. L. ALTSHULER and D. E. KHMELNITSKII, "Fluctuation Properties Of Small Conductors," *Jetp Letters* **42**, 359 (1985).

[45] S. WASHBURN and R. A. WEBB, "Quantum Transport In Small Disordered Samples From The Diffusive To The Ballistic Regime," *Reports On Progress In Physics* **55**, 1311 (1992).

[46] D. C. Ralph, C. T. Black, and M. Tinkham, "Spectroscopic measurements of discrete electronic states in single metal particles," *Physical Review Letters* **74**, 3241 (1995).

[47] D. Davidovic and M. Tinkham, "Spectroscopy, interactions, and level splittings in an nanoparticles," *Physical Review Letters* **83**, 1644 (1999).

[48] J. R. Petta and D. C. Ralph, "Studies of spin-orbit scattering in noble-metal nanoparticles using energy-level tunneling spectroscopy," *Physical Review Letters* **87**, 266801 (2001).

[49] C. T. Black, D. C. Ralph, and M. Tinkham, "Spectroscopy of the superconducting gap in individual nanometer-scale aluminum particles," *Physical Review Letters* **76**, 688 (1996).

[50] M. Braun, J. Konig, and J. Martinek, "Hanle effect in transport through quantum dots coupled to ferromagnetic leads," *Europhysics Letters* **72**, 294 (2005).

[51] I. Weymann and J. Barnas, "Effect of intrinsic spin relaxation on the spin-dependent cotunneling transport through quantum dots," *Physical Review B* **73**, 205309 (2006).

[52] S. J. van der Molen, N. Tombros, and B. J. van Wees, "Magneto-Coulomb effect in spin-valve devices," *Physical Review B* **73**, 220406 (2006).

[53] W. Wetzels, G. E. W. Bauer, and M. Grifoni, "Exchange effects on electron transport through single-electron spin-valve transistors," *Physical Review B* **74**, 224406 (2006).

[54] A. Cottet and M. S. Choi, "Magnetoresistance of a quantum dot with spin-active interfaces," *Physical Review B* **74**, 235316 (2006).

[55] F. Ernult, K. Yakushiji, S. Mitani, and K. Takanashi, "Spin accumulation in metallic nanoparticles," *Journal Of Physics-Condensed Matter* **19**, 165214 (2007).

[56] F. J. Jedema, M. S. Nijboer, A. T. Filip, and B. J. van Wees, "Spin injection and spin accumulation in all-metal mesoscopic spin valves," *Physical Review B* **67**, 085319 (2003).

[57] F. Beuneu and P. Monod, "The Elliott relation in pure metals," *Phys. Rev. B* **18**, 2422 (1978).

[58] J. Fabian and S. D. Sarma, "Spin relaxation of conduction electrons," *J. Vac. Sci. Technol. B* **17**, 1708 (1999).

[59] J. von Delft and D. C. Ralph, "Spectroscopy of discrete energy levels in ultrasmall metallic grains," *Physics Reports-Review Section Of Physics Letters* **345**, 61 (2001).

[60] D. G. Salinas, S. Gueron, D. C. Ralph, C. T. Black, and M. Tinkham, "Effects of spin-orbit interactions on tunneling via discrete energy levels in metal nanoparticles," *Physical Review B* **60**, 6137 (1999).

[61] S. Adam, M. L. Polianski, X. Waintal, and P. W. Brouwer, "Magnetic-field dependence of energy levels in ultrasmall metal grains," *Physical Review B* **66**, 195412 (2002).

[62] A. T. JOHNSON, L. P. KOUWENHOVEN, W. DEJONG, N. C. VANDERVAART, C. J. P. M. HARMANS, and C. T. FOXON, "Zero-Dimensional States And Single Electron Charging In Quantum Dots," *Physical Review Letters* **69**, 1592 (1992).

[63] V. J. GOLDMAN, B. SU, and J. E. CUNNINGHAM, "Single-Electron Tunneling In Double-Barrier Nanostructures," *International Journal Of Modern Physics B* **6**, 2321 (1992).

[64] A. E. HANNA and M. TINKHAM, "Variation Of The Coulomb Staircase In A 2-Junction System By Fractional Electron Charge," *Physical Review B* **44**, 5919 (1991).

[65] D. V. Averin and K. K. Likharev, *Mesoscopic Phenomena in Solids* (Elsevier and Amsterdam, 1991).

[66] M. Tinkham, *Introduction to Superconductivity* (McGraw-Hill, New York, 1996).

[67] R. C. J. S. K. Mullen, E. Ben-JacobZ, "I-V characteristics of coupled ultrasmall-capacitance normal tunnel junctions," *Phys. Rev. B* **37**, 98 (1988).

[68] D. C. Ralph, C. T. Black, and M. Tinkham, "Studies of electron energy levels in single metal particles," *Physica B* **218**, 258 (1996).

[69] D. C. Ralph, C. T. Black, and M. Tinkham, "Gate-voltage studies of discrete electronic states in aluminum nanoparticles," *Physical Review Letters* **78**, 4087 (1997).

[70] O. AGAM, B. L. ALTSHULER, and A. V. ANDREEV, "Spectral Statistics - From Disordered To Chaotic Systems," *Physical Review Letters* **75**, 4389 (1995).

[71] N. W. Ashcroft and N. D. Mermin, *Solid State Physics* (W.P. Saunders College, 1976).

[72] J. Von Delft and D. C. Ralph, "Spectroscopy of discrete energy levels in ultrasmall metallic grains," *Physics Reports-Review Section of Physics Letters* **345**, 62 (2001).

[73] M. M. Deshmukh, *PROBING MAGNETISM AT THE NANOMETER SCALE USING TUNNELING SPECTROSCOPY*, PhD thesis Cornell University 2002.

[74] E. Bonet, M. M. Deshmukh, and D. C. Ralph, "Solving rate equations for electron tunneling via discrete quantum states," *Physical Review B* **65**, 045317 (2002).

[75] C. Tiusan, F. Greullet, M. Hehn, F. Montaigne, S. Andrieu, and A. Schuhl, "Spin tunnelling phenomena in single-crystal magnetic tunnel junction systems," *Journal Of Physics-Condensed Matter* **19**, 165201 (2007).

[76] M. Julliere, "Tunneling between ferromagnetic-films," *Physics Letters A* **54**, 225 (1975).

[77] J. S. MOODERA, L. R. KINDER, T. M. WONG, and R. MESERVEY, "Large Magnetoresistance At Room-Temperature In Ferromagnetic Thin-Film Tunnel-Junctions," *Physical Review Letters* **74**, 3273 (1995).

[78] T. Miyazaki and N. Tezuka, "Spin polarized tunneling in ferromagnet insulator ferromagnet junctions," *Journal Of Magnetism And Magnetic Materials* **151**, 403 (1995).

[79] S. H. Chun, S. J. Potashnik, K. C. Ku, P. Schiffer, and N. Samarth, "Spin-polarized tunneling in hybrid metal-semiconductor magnetic tunnel junctions," *Physical Review B* **66**, 100408 (2002).

[80] J. C. SLONCZEWSKI, "Conductance And Exchange Coupling Of 2 Ferromagnets Separated By A Tunneling Barrier," *Physical Review B* **39**, 6995 (1989).

[81] E. Y. Tsymbal, O. N. Mryasov, and P. R. LeClair, "Spin-dependent tunnelling in magnetic tunnel junctions," *Journal of Physics-Condensed Matter* **15**, R109 (2003).

[82] S. Zhang, P. M. Levy, A. C. Marley, and S. S. P. Parkin, "Quenching of magnetoresistance by hot electrons in magnetic tunnel junctions," *Physical Review Letters* **79**, 3744 (1997).

[83] J. S. Moodera, J. Nowak, and R. J. M. van de Veerdonk, "Interface magnetism and spin wave scattering in ferromagnet-insulator-ferromagnet tunnel junctions," *Physical Review Letters* **80**, 2941 (1998).

[84] C. H. Shang, J. Nowak, R. Jansen, and J. S. Moodera, "Temperature dependence of magnetoresistance and surface magnetization in ferromagnetic tunnel, junctions," *Physical Review B* **58**, R2917 (1998).

[85] X. H. Wang and A. Brataas, "Large magnetoresistance ratio in ferromagnetic single-electron transistors in the strong tunneling regime," *Physical Review Letters* **83**, 5138 (1999).

[86] H. Sukegawa, S. Nakamura, A. Hirohata, N. Tezuka, and K. Inomata, "Significant magnetoresistance enhancement due to a cotunneling process in a double tunnel junction with single discontinuous ferromagnetic layer insertion," *Physical Review Letters* **94**, 068304 (2005).

[87] S. Takahashi and S. Maekawa, "Enhancement in spin-dependent tunneling with Coulomb blockade," *J. Magn. Magn. Mater.* **198**, 143 (1999).

[88] F. J. Jedema, A. T. Filip, and B. J. van Wees, "Electrical spin injection and accumulation at room temperature in an all-metal mesoscopic spin valve," *Nature* **410**, 345 (2001).

[89] E. I. Rashba, "Theory of electrical spin injection: Tunnel contacts as a solution of the conductivity mismatch problem," *Physical Review B* **62**, R16267 (2000).

[90] R. Meservey and P. M. Tedrow, "Spin-polarized electron-tunneling," *Physics reports-review section of physics letters* **238**, 173 (1994).

[91] S. M. Sze, *Semiconductor Devices* (John Wiley & Sons, Inc., 2002).

[92] C. T. Black, *Tunneling spectroscopy of nanometer-scale metal particles*, PhD thesis Harvard University 1996.

[93] F. Pobell, *Matter and Methods at Low temperatures, Second Edition* (Springer, 1996).

[94] W. Rudzinski and J. Barnas, "Tunnel magnetoresistance in ferromagnetic junctions: Tunneling through a single discrete level," *PHYSICAL REVIEW B* **64**, 085318 (2001).

[95] N. T. S. J. van der Molen and B. J. van Wees, "Magneto-Coulomb effect in spin-valve devices," *PHYSICAL REVIEW B* **73**, 220406 (2006).

[96] D. D. Y. G. Wei, C. E. Malec, "Saturation of Spin-Polarized Current in Nanometer Scale Aluminum Grains," *Physical Review B (Accepted)* (2007).

[97] H. R. Zeller and I. Giaever, "Tunneling, zero-bias anomalies, and small superconductors," *Physical Review* **181**, 789 (1969).

[98] G. Bergman, "Weak localization in thin films," *Physics Rep.* **107**, 1 (1984).

[99] Y. Lyanda-Geller, I. L. Aleiner, and P. M. Goldbart, "Domain walls and conductivity of mesoscopic ferromagnets," *Physical Review Letters* **81**, 3215 (1998).

[100] D. LOSS, H. SCHOELLER, and P. M. GOLDBART, "Weak-Localization Effects And Conductance Fluctuations - Implications Of Inhomogeneous Magnetic-Fields," *Physical Review B* **48**, 15218 (1993).

[101] G. Tatara and H. Fukuyama, "Resistivity due to a domain wall in ferromagnetic metal," *Physical Review Letters* **78**, 3773 (1997).

[102] S. Adam, M. Kindermann, S. Rahav, and P. W. Brouwer, "Mesoscopic anisotropic magnetoconductance fluctuations in ferromagnets," *Physical Review B* **73**, 212408 (2006).

[103] A. D. Kent, J. Yu, U. Rudiger, and S. S. P. Parkin, "Domain wall resistivity in epitaxial thin film microstructures," *Journal Of Physics-Condensed Matter* **13**, R461 (2001).

[104] J. F. Gregg, W. Allen, K. Ounadjela, M. Viret, M. Hehn, S. M. Thompson, and J. M. D. Coey, "Giant magnetoresistive effects in a single element magnetic thin film," *Physical Review Letters* **77**, 1580 (1996).

[105] M. Viret, D. Vignoles, D. Cole, J. M. D. Coey, W. Allen, D. S. Daniel, and J. F. Gregg, "Spin scattering in ferromagnetic thin films," *Physical Review B* **53**, 8464 (1996).

[106] M. Viret, Y. Samson, P. Warin, A. Marty, F. Ott, E. Sondergard, O. Klein, and C. Fermon, "Anisotropy of domain wall resistance," *Physical Review Letters* **85**, 3962 (2000).

[107] U. Ebels, A. Radulescu, Y. Henry, L. Piraux, and K. Ounadjela, "Spin accumulation and domain wall magnetoresistance in 35 nm Co wires," *Physical Review Letters* **84**, 983 (2000).

[108] U. Ruediger, J. Yu, S. Zhang, A. D. Kent, and S. S. P. Parkin, "Negative domain wall contribution to the resistivity of microfabricated Fe wires," *Physical Review Letters* **80**, 5639 (1998).

[109] S. G. Kim, Y. Otani, K. Fukamichi, S. Yuasa, R. Nyvlt, and T. Katayama, "Magnetoresistivity of micron size (10.0) epitaxial Co wires," *Ieee Transactions On Magnetics* **35**, 2862 (1999).

[110] D. Ravelosona, A. Cebollada, F. Briones, C. Diaz-Paniagua, M. A. Hidalgo, and F. Batallan, "Domain-wall scattering in epitaxial FePd ordered alloy films with perpendicular magnetic anisotropy," *Physical Review B* **59**, 4322 (1999).

[111] R. Danneau, P. Warin, J. P. Attane, I. Petej, C. Beigne, C. Fermon, O. Klein, A. Marty, F. Ott, Y. Samson, and M. Viret, "Individual domain wall resistance in submicron ferromagnetic structures," *Physical Review Letters* **88**, 157201 (2002).

[112] D. Buntinx, S. Brems, A. Volodin, K. Temst, and C. Van Haesendonck, "Positive domain wall resistance of 180 degrees Neel walls in Co thin films," *Physical Review Letters* **94**, 017204 (2005).

[113] C. Yu, S. F. Lee, J. L. Tsai, E. W. Huang, T. Y. Chen, Y. D. Yao, Y. Liou, and C. R. Chang, "Study of domain wall magnetoresistance by submicron patterned magnetic structure," *Journal Of Applied Physics* **93**, 8761 (2003).

[114] T. R. MCGUIRE and R. I. POTTER, "Anisotropic Magnetoresistance In Ferromagnetic 3d Alloys," *Ieee Transactions On Magnetics* **11**, 1018 (1975).

[115] K. M. HONG and N. GIORDANO, "Approach To Mesoscopic Magnetic Measurements," *Physical Review B* **51**, 9855 (1995).

[116] J. Aumentado and V. Chandrasekhar, "Magnetotransport in mesoscopic ferromagnetic particles," *Physica B* **284**, 1742 (2000).

[117] S. Kasai, E. Saitoh, and H. Miyajima, "Quantum transport properties in ferromagnetic nanorings at low temperature," *Journal Of Applied Physics* **93**, 8427 (2003).

[118] S. Lee, A. Trionfi, T. Schallenberg, H. Munekata, and D. Natelson, "Mesoscopic conductance effects in InMnAs structures," *Applied Physics Letters* **90**, 032105 (2007).

[119] Y. Imry, *'Physics of mesoscopic systems' in Directions in Condensed Matter Physics* (World Scientific Press, Singapore, 1986).

[120] M. Janssen, "Statistics and scaling in disordered mesoscopic electron systems," *Physics Reports-Review Section Of Physics Letters* **295**, 2 (1998).

[121] S. Datta, *Electronic transport in Mesoscopic Systems* (Cambridge University Press, 2002).

[122] T. Heinzel, *Mesoscopic Electronics in Solid State Nanostructures* (John Wiley & Sons, 2007).

[123] R. A. Webb and S. Washburn, "Quantum Interference Fluctuations In Disordered Metals," *Physics Today* **41**, 46 (1988).

[124] Y. AHARONOV and D. BOHM, "Significance Of Electromagnetic Potentials In The Quantum Theory," *Physical Review* **115**, 485 (1959).

[125] L. P. GORKOV, A. I. LARKIN, and D. E. KHMELNITSKII, "Particle Conductivity In A Two-Dimensional Random Potential," *Jetp Letters* **30**, 228 (1979).

[126] S. KOBAYASHI, F. KOMORI, Y. OOTUKA, and W. SASAKI, "In T-Dependence Of Resistivity In 2-Dimensionally Coupled Fine Particles Of Cu," *Journal Of The Physical Society Of Japan* **49**, 1635 (1980).

[127] B. L. ALTSHULER, "Fluctuations In The Extrinsic Conductivity Of Disordered Conductors," *Jetp Letters* **41**, 648 (1985).

[128] B. L. ALTSHULER, Y. GEFEN, and Y. IMRY, "Persistent Differences Between Canonical And Grand Canonical Averages In Mesoscopic Ensembles - Large Paramagnetic Orbital Susceptibilities," *Physical Review Letters* **66**, 88 (1991).

[129] P. M. Levy and S. F. Zhang, "Resistivity due to domain wall scattering," *Physical Review Letters* **79**, 5110 (1997).

[130] L. BERGER, "Exchange Interaction Between Ferromagnetic Domain-Wall And Electric-Current In Very Thin Metallic-Films," *Journal Of Applied Physics* **55**, 1954 (1984).

[131] A. D. Kent, U. Rudiger, J. Yu, L. Thomas, and S. S. P. Parkin, "Magnetoresistance, micromagnetism, and domain wall effects in epitaxial Fe and Co structures with stripe domains (invited)," *Journal Of Applied Physics* **85**, 5243 (1999).

[132] M. Klaui, C. A. F. Vaz, J. Rothman, J. A. C. Bland, W. Wernsdorfer, G. Faini, and E. Cambril, "Domain wall pinning in narrow ferromagnetic ring structures probed by magnetoresistance measurements," *Physical Review Letters* **90**, 097202 (2003).

[133] B. Cetin and N. Giordano, "Domain wall resistance and magnetoresistance of narrow ferromagnetic wires," *Materials Science And Engineering B-Solid State Materials For Advanced Technology* **84**, 133 (2001).

[134] R. F. Sabirianov, A. K. Solanki, J. D. Burton, S. S. Jaswal, and E. Y. Tsymbal, "Domain-wall magnetoresistance of Co nanowires," *Physical Review B* **72**, 054443 (2005).

[135] M. Hayashi, L. Thomas, Y. B. Bazaliy, C. Rettner, R. Moriya, X. Jiang, and S. S. P. Parkin, "Influence of current on field-driven domain wall motion in permalloy nanowires from time resolved measurements of anisotropic magnetoresistance," *Physical Review Letters* **96**, 197207 (2006).

[136] A. Radulescu, U. Ebels, Y. Henry, K. Ounadjela, J. L. Duvail, and L. Piraux, "Magnetoresistance of a single domain wall in Co and Ni nanowires," *Ieee Transactions On Magnetics* **36**, 3062 (2000).

[137] T. Taniyama, I. Nakatani, T. Namikawa, and Y. Yamazaki, "Resistivity due to domain walls in Co zigzag wires," *Physical Review Letters* **82**, 2780 (1999).

[138] W. H. MEIKLEJOHN and C. P. BEAN, "New Magnetic Anisotropy," *Physical Review* **102**, 1413 (1956).

[139] B. Hausmanns, T. P. Krome, and G. Dumpich, "Magnetoresistance and magnetization reversal process of Co nanowires covered with Pt," *Journal Of Applied Physics* **93**, 8095 (2003).

[140] F. Radu, M. Etzkorn, R. Siebrecht, T. Schmitte, K. Westerholt, and H. Zabel, "Interfacial domain formation during magnetization reversal in exchange-biased CoO/Co bilayers," *Physical Review B* **67**, 134409 (2003).

[141] M. Brands, A. Carl, and G. Dumpich, "Absence of weak electron localization in ferromagnetic cobalt wires," *Europhysics Letters* **68**, 268 (2004).

[142] K. E. NAGAEV, "Nonlinear Conductivity Of Diffusive Normal-Metal Contacts," *Physics Letters A* **189**, 134 (1994).